The Seismogenic Zone of Subduction Thrust Faults, ed. T. Dixon and C. Moore, Columbia U. Press, 2007.

13

Laboratory-Observed Faulting in Intrinsically and Apparently Weak Materials

Strength, Seismic Coupling, Dilatancy, and Pore-Fluid Pressure

N. M. Beeler

Abstract

Under some circumstances, subduction thrust faulting produces the Earth's largest and most hazardous earthquakes and earthquake-induced tsunamis, but in other localities, large-scale aseismic slip is common and portions of some subduction zones are nearly completely aseismic. Understanding the particular conditions that lead to seismic rather than aseismic fault slip is critical for improving earthquake and tsunami hazard estimates in subduction zones and is a major objective of the NSF-MARGINS initiative. This paper reviews laboratory rock mechanics observations of rock fracture and fault slip relevant to seismic shallow crustal faulting, emphasizing differences between behavior of intrinsically weak and strong faults and identifying the underlying physical processes and conditions that influence fault strength. These laboratory rock friction and rock failure observations, made primarily on strong faults and intact rock, largely suggest that earthquake occurrence is a result of dilatancy. As many subduction zones appear to be profoundly weak, the conditions for seismicity are considered in the context of intrinsic fault weakness, and under circumstances of apparent weakness owing to high pore pressure. The principal conclusion of this review is that in the absence of chemical effects of fluids on fault strength, both intrinsic weakness and apparent weakness resulting from high pore pressure tend to encourage aseismic over seismic slip. However, the sliding stability of intrinsically and apparently weak rocks and minerals is not well studied. The effect of high pore pressure on sliding stability has only been considered for an intrinsically strong, highly dilatant, apparently weak fault. Since many weak phases found in subduction zones have low dilatancy, the effect of high pore pressure on sliding stability is presently unknown. In addition, chemical effects on fault strength are not well studied to date. Many weak phases have strengths that are sensitive to the chemical environment; in

particular, clays and other sheet silicate minerals have strengths that are influenced by the presence of water. The role of such effects in seismogenesis is not known at present. Given the present state of knowledge, sliding stability and fault strength cannot be unequivocally related.

Introduction

The San Andreas fault between San Juan Batista and Parkfield and sections of the Hayward-Calaveras fault south of San Francisco Bay are of the few well-characterized locations in the world where slip on large displacement through-going crustal-scale continental faults is predominately aseismic [*Scholz*, 1990]. However, in subduction zones, large-scale aseismic slip is very common, and portions of some subduction zones are nearly completely aseismic [*Peterson and Seno*, 1984]. At the same time, subduction thrust faulting produces the Earth's largest and most hazardous earthquakes [*Kelleher et al.,* 1974] and the Earth's largest earthquake-induced tsunamis [*Furumoto*, 1991]. Understanding the particular conditions that lead to seismic rather than aseismic response is critical for improving earthquake and tsunami hazard estimates in subduction zones and is a major objective of the NSF-MARGINS initiative. At present, seismogenesis in subduction zones is not well understood for any particular subduction thrust. With the exception of temperature [*Goetze and Evans,* 1979; *Brace and Kohlstedt*, 1980; *Kirby*, 1980], seismicity in subduction zones has not been clearly related to specific observables such as strain rate, strain, intrinsic material strength, mineralogy, porosity, or fluid pressure. Though qualitative arguments suggest nearly cohesionless weak accretionary prism sediments are aseismic and that stronger cemented and lithified materials are associated with the onset of seismicity [*Byrne et al.,* 1988; *Moore and Saffer*, 2001], some great subduction zones earthquakes occur on faults that are weaker than the intrisinic strength of the weakest geomaterials. *Wang and He* [1999] estimate a spatially averaged apparent friction $\mu' = 0.05–0.09$ for the Nankai and Cascadia subduction zones; here, $\mu' = \mu\left(1 - p/\sigma_L\right)$, μ is friction, the ratio of shear to normal stress and, p is fluid pressure, σ_L is lithostatic pressure (see Background). Weak phases in subduction environments, illite, and chrysotile serpentine, have friction coefficients between 0.2 and 0.45 [*Morrow et al.,* 1992, 2000; *Moore et al*., 1996; *Moore and Lockner*, 2004]. Saturated montmorillonite can have friction as low as 0.08 at low effective stress [*Logan and Rauenzahn*, 1987], but since montmorillonite is chemically unstable above 125°C, the weakness of the seismic Nankai and Cascadia subduction zones is apparently not due to intrinsic material properties alone. Furthermore, saturated smectite, illite, and serpentine, though pressure dependent, are apparently rheologically ductile in the shallow crust (see Strength and Rate Dependence of Subduction Zone Minerals section below); at least they do not permit seismic stress drops in laboratory tests at natural low loading rates. Thus, on the basis of laboratory observations

to date, the Nankai and Cascadia subduction zones are both weaker and more seismic than expected mineral composition permits.

This paper reviews laboratory rock mechanics observations of rock fracture and fault slip relevant to seismic and aseismic shallow crustal faulting, emphasizing differences between behavior of intrinsically weak and strong faults. The physical processes that influence fault strength in the laboratory under shallow crustal conditions are also identified. Representative constitutive equations for rock failure and for slip on preexisting faults are used to illustrate implications of the laboratory observations. These relations are used to develop the standard laboratory-derived conditions for seismic fault slip (instability). The conditions for seismicity are considered in the context of intrinsic fault weakness and under circumstances of apparent weakness due to high pore pressure. A conclusion of this review is that in the absence of chemical effects of fluids on fault strength, both intrinsic weakness and apparent weakness resulting from high pore pressure encourage aseismic over seismic slip. Thus absolute fault strength, apparent strength, and the stability of faulting may correlate in some cases, which might explain or help to explain the spatial and temporal distribution of seismicity in weak-faulting environments.

However, existing theories of frictional instability, based on frictional sliding on preexisting faults [*Dieterich*, 1978b, 1979] and on analysis of the resulting constitutive equations [*Ruina*, 1983, *Rice*, 1983; *Rice and Ruina*, 1983], may not be comprehensive. The experiments that established the condition for unstable slip were done dry at room temperature on artificially well-localized faults in quartzofeldspathic rocks. Inferences of the role of fluid pressure in instability are also based on analysis of these intrinsically strong and highly dilatant rocks. Such laboratory faults are much stronger than many seismic subduction zones and many weak materials have material properties (e.g., molecular bond strengths [*Morrow et al.*, 2000; *Moore and Lockner*, 2004], material anisotropy [e.g., *Mares and Kronenburg*, 1993], and dilatancy [*Escartin et al.*, 1997] that are quite different. In particular, many weak phases found in subduction thrusts have strengths that are significantly influenced by the presence of water and that deform by contact-scale processes that are distinctly different from those occurring in quartzofeldspathic materials. The final section of this paper reviews faulting experiments in intrinsically weak saturated fault zones and the implications of these results for seismicity.

Background: Pressure Dependence

Knowledge of crustal stress, earthquake occurrence and related crustal processes have been guided by laboratory studies in rock mechanics. To begin to put laboratory observations in context, let's briefly illustrate the specific observations and terminology used to define rock failure, fault slip, pressure dependence, and the strength losses of brittle failure (fig. 13.1a) using stress-strain data from a series of experiments at different confining pressure conducted

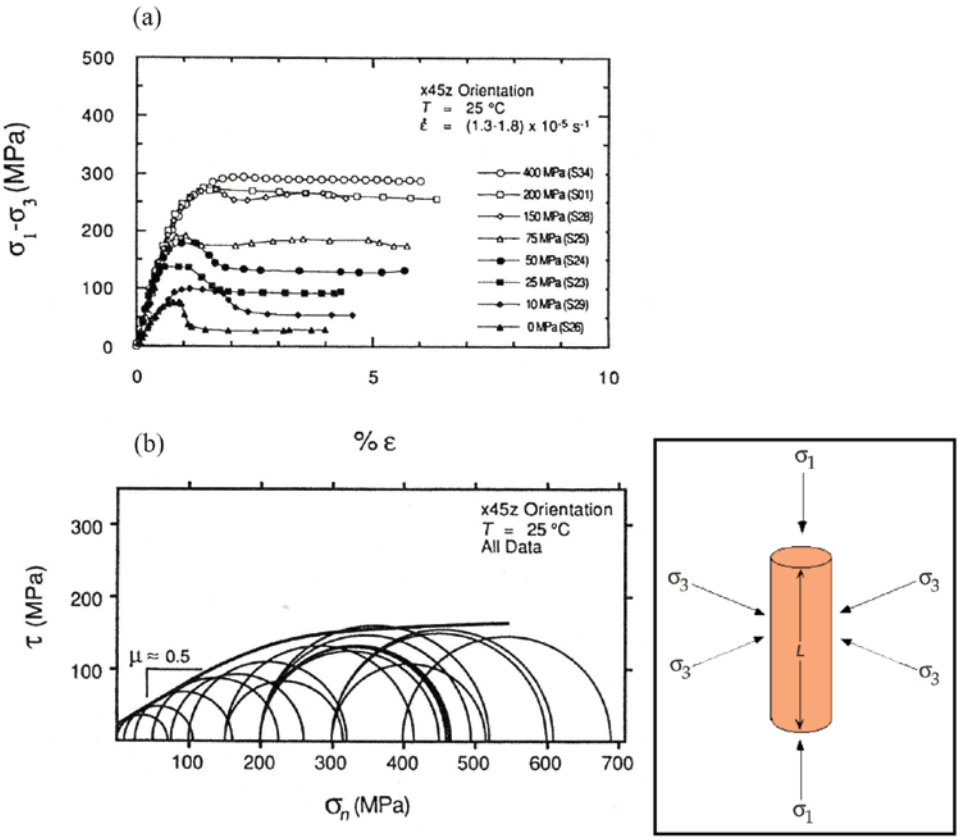

Figure 13.1 Observations of rock failure from *Shea and Kronenberg* [1992]. (a) Differential stress versus axial strain (percent) data from a series of experiments at different confining pressure conducted on initially intact mica schist at room temperature. Tests use a cylindrical sample and two independently controlled applied stresses (inset). The differential stress is $\sigma_\Delta = \sigma_1 - \sigma_3$. Axial strain ε_z in percent is $100 \times (L - L_0)/L_0$, where L is sample length and L_0 is the starting length. The failure condition is defined by the peak stress on the stress strain curve, which in the case of faulting can be related to the shear τ and normal stresses σ_n on the resulting fault (see text). The measured shear and normal stress at peak are used to define the brittle failure envelope from the tests at different confining pressures; the envelope is constructed by collecting the failure strengths from the different tests on a single shear versus normal stress plot (fig. 13.1b). (b). The failure envelope (heavy line) for the tests shown in figure 13.1a. Also shown are the Mohr stress circles, at peak stress in each test.

on initially intact mica schist at room temperature from *Shea and Kronenburg* [1992]. Failure tests are conducted using a cylindrical sample and two independently controlled applied stresses, an axial stress σ_1 provided by a mechanically driven hardened metal piston, and a constant confining pressure σ_3 provided to the jacketed sample by pressurized fluid (fig. 13.1, inset). The

differential stress $\sigma_\Delta = \sigma_1 - \sigma_3$ when raised to a sufficient level causes failure, either a throughgoing fracture at angle ϕ referenced to σ_1, or from deformation distributed throughout the sample. The failure condition is usually defined by the peak stress (fig. 13.1), which in the case of faulting can be related to the shear τ and normal stresses σ_n on the fault by the relationships $\tau = 0.5\sigma_\Delta \sin 2\phi$, and $\sigma_n = \sigma_3 + 0.5\sigma_\Delta(1 - \cos 2\phi)$.

It is these so measured shear and normal stress associated with the peak strength that are used to define the brittle failure condition from a sequence of tests at different confining pressures as shown in figure 13.1a; these failure shear and normal stresses are collected on a single plot, defining the failure envelope shown in figure 13.1b. The failure envelope is curved with pressure dependence $\mu_f = \partial\tau/\partial\sigma_e$ that is high at low stress and decreases with increasing stress. The individual stress strain data (fig. 13.1a) also show a postpeak strain weakening associated with failure. The strain weakening is transient, and strength drops to a steady level defining the residual sliding strength. The residual strength usually has pressure dependence quite similar to the failure strength over most of the brittle regime (fig. 13.2). The residual sliding strength and peak strength define the shear strength loss. The strength loss does not occur in tests at high pressure; for example in figure 13.1a the strength loss is becoming smaller with increasing confining pressure.

Though the examples in figure 13.2 show a nonlinear dependence of the shear strength at failure on confining or fault normal stress, laboratory observations of rock failure strength and fault strength at low to modest confining pressure, corresponding to shallow crustal conditions, can be described for illustrative purposes by the linear empirical Coulomb failure relation between shear stress in the direction of slip τ and the effective normal stresses σ_e across the fracture plane or fault at the time of failure

$$|\tau| = S_o + \mu_f \sigma_e \tag{13.1a}$$

Here S_o, the strength at zero effective normal stress, is cohesion. And μ_f is a coefficient of friction $\mu_f = \partial\tau/\partial\sigma_e$, the normal pressure dependence of fault strength, referred to in the case of rock failure as the internal friction coefficient and in the case of slip on a preexisting fault as the coefficient of friction.

Pore-fluid pressure affects rock failure and fault strength by decreasing normal stress throughout the rock mass according to the effective pressure law [*Terzaghi*, 1923; *Hubbert and Rubey*, 1959], $\sigma_e = \sigma_n - \alpha p$, where σ_n is the applied normal stress, p is pore-fluid pressure, and α is a constant related to pore geometry. For the onset of frictional sliding and for the fracture strength of rock with well-connected porosity, $\alpha = 1$ and $\sigma_e = \sigma_n - p$. The normal hydraulic head for well-connected porous material $p = \rho_{H_2O} g z$ will offset the overburden pressure $\sigma_v = \rho g z$ by approximately one third owing to the density difference between water and rock. Here z is depth from the surface, g is the acceleration due to gravity 9.8 m/s^2, ρ is rock density, and ρ_{H_2O} is the density of water. How-

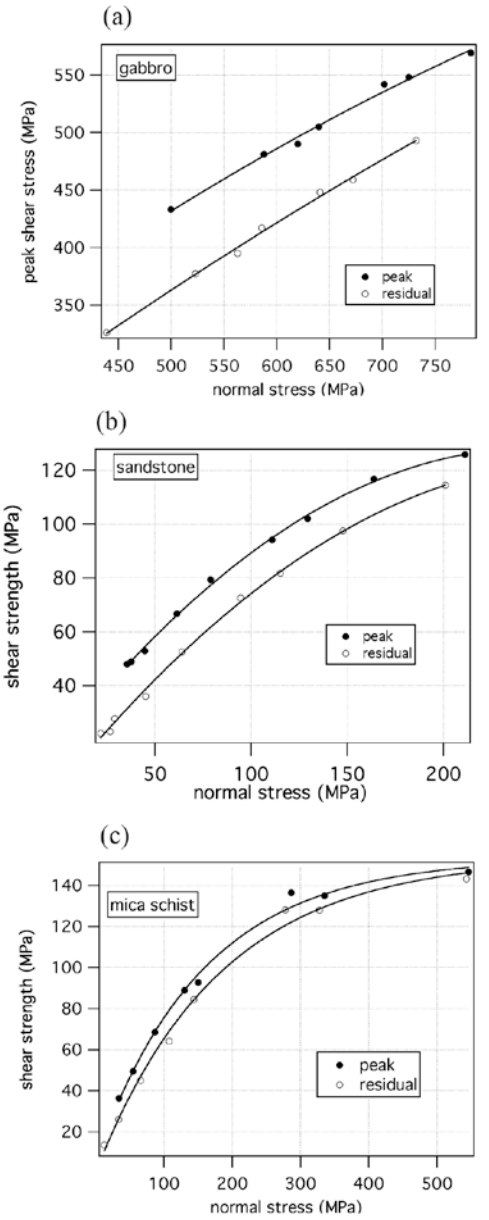

Figure 13.2 Peak and residual shear strengths defining the strength loss during failure for three rock types. Tests were conducted at constant confining pressure, so failure produces a reduction in both shear strength and normal stress across the failure plane. Shear and normal stress are estimated from the measured confining pressure and differential stress, and the orientation of the fault as measured from the recovered sample (see equations in the text). (a) A strong gabbro [*Wong*, 1986]. (b) Intermediate strength sandstone [*Bernabe and Brace*, 1990]. (c) A weak mica schist [*Shea and Kronenberg*, 1993].

ever, for isolated porosity at depth, especially under conditions of rapid burial or underthrusting, consolidation and dewatering processes can compress pore fluids to exceed hydrostatic pressure. Under some circumstances, burial and tectonic forcing may lead to repeated episodes of hydraulic fracture. Overpressure is of considerable interest and presumed importance in subduction fault-zone mechanics owing to known high volume fluid sources (buried porous sediments, dehydration reactions) [e.g., *Saffer and Bekins*, 2002], the apparent

weakness of subduction faults [*Wang and He*, 1999], and indirect evidence of elevated pressure [e.g., *Moore and von Huene*, 1980; *Westbrook and Smith*, 1983].

Intact crystalline rock, particularly quartzofeldspathic rock, has significant cohesion, where as preexisting faults more often do not. In this latter case, the failure strength (equation (13.1a)) has the simpler form

$$|\tau| = \mu_f \sigma_e \tag{13.1b}$$

known as Amontons' law. The strength quantity most easily measured and most often used in studies of faulting is the simple ratio of shear to normal stress. Throughout this paper, this ratio μ, is referred to as friction or frictional resistance, and for equation (13.1a) is related to the friction coefficient μ_f, by

$$\mu = \frac{|\tau|}{\sigma_e} = \frac{S_0}{\sigma_e} + \mu_f \tag{13.1c}$$

The laboratory observations indicate that the failure strength of crustal rock increases with normal stress; since the ambient level of stress in the crust is controlled by the overburden stress $\sigma_v = (\rho - \rho_{H_20})gz$, effective normal stress increases linearly to a limiting depth. Throughout this paper, rocks or faults are regarded as pressure dependent, as in equation (13.1), meaning that their failure strength or sliding strength increases with effective pressure.

Temperature also increases with depth in the Earth, eventually reaching the high temperatures and pressures where bulk material strength is controlled by deformation mechanisms other than those underlying the behavior described by equation (13.1). Examples of high temperature/pressure mechanisms are dislocation glide, dislocation creep, and pressure solution. All of these processes are ductile; that is, they accommodate large permanent deformation without loss of strength. For pressure solution and dislocation creep, the ductile flow strength, equal to the differential stress σ_Δ during yielding, rapidly decreases with temperature as follows from the creep law of the form

$$\dot{\varepsilon} = C\sigma_d^n \exp\frac{-E}{RT} \tag{13.2}$$

where R is the gas constant, E is the activation energy, n is a dimensionless constant with values in the range 1–4 depending on the particular mechanism, and C is a constant (MPa^{-n}/s).

Laboratory observations suggest earthquakes should be limited to conditions where the differential stress does not exceed the ductile flow strength of rocks, because ductile deformation precludes dynamic stress drop. Thus,

using equations (13.1) and (13.2) as representative, the majority of crustal seismicity occurs at conditions where strength equation (13.1) is lower than equation (13.2). Diagrams, originated by *Goetze and Evans* [1979], such as figure 13.3a, where quartz strength is assumed representative of the continental crust and olivine of oceanic crust, can crudely explain depth-dependent features of natural seismicity (figures 13.3b and 13.3c). However, uncertainties in the form of the flow law [*Brace and Kohlstedt*, 1980; *Kirby*, 1980] and uncertainty of the Earth's temperature gradient, depth variation of lithology, and the strain rate dependence of equation (13.2) do not allow rock strength or other material properties to be well constrained by natural seismicity.

Furthermore, while the intersection of equations (13.1) and (13.2) is often referred to as the brittle-ductile transition, when considering particular distributions of seismicity, using brittle to describe this transition can be completely misleading. Rheologically, brittle describes materials whose ability to resist deformation decreases with increasing permanent deformation, indicat-

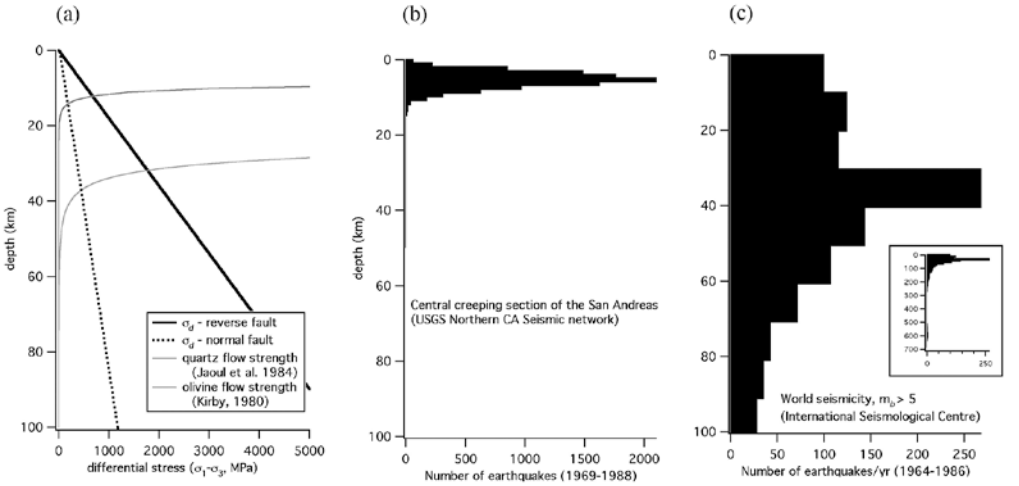

Figure 13.3 The brittle-ductile transition and the depth extent of seismicity. (a) Brittle and ductile strength. The brittle strength was calculated from equations (13.1) ($S_0 = 0$, $\mu = 0.6445$) for normal (dashed) and reverse (solid) faulting assuming that the vertical stress is coincident with one of the principal stresses [*Anderson*, 1951]. The ductile strengths were calculated from equation (13.2), assuming strain rate $\dot{\varepsilon} = 10^{-12}$ and a temperature gradient of 20°K/km, using data from *Jaoul et al.* [1984] ($A = 11.6$, $n = 1.8$, $E = 150.6$ kJ/mol) for wet quartzite and data from *Kirby* [1980] ($A = 1.2 \times 10^{10}$, $n = 4.8$, $E = 502$ kJ/mol) for wet olivine g. (b) Seismicity from the central creeping section of the San Andreas fault, recorded by the U.S. Geological Survey northern California seismic network from 1969 to 1988 [from *Blanpied et al.*, 1991]. (c) World seismicity for events with body wave magnitude $m_b > 5$ as recorded in the International Seismological Centre catalog from January 1964 to February 1986. The inset shows the complete data set [from *Frolich*, 1989].

ing strength loss with strain. Instead of rheologically brittle, many pressure-dependent materials of interest to subduction zone mechanics are rheologically ductile, do not allow material strength loss with strain, and therefore do not permit seismic stress drop. For such materials, there is brittle-ductile transition from a brittle pressure-dependent regime with associated faulting, to a rheologically ductile but pressure-dependent semibrittle regime (transitional or cataclastic flow) (e.g., review by *Evans et al.* [1990]). The semibrittle regime is not associated with strength loss and may not be associated with well-localized deformation. So there may be two transitions with increasing depth: a brittle to semibrittle and a semibrittle to fully plastic; the former is the brittle-ductile transition. The latter is a transition with increasing depth from a pressure-sensitive, approximately temperature and strain rate insensitive rheology such as equation (13.1) to a pressure insensitive, strongly temperature and strain-rate dependent regime (13.2). As this review considers seismic and aseismic faulting in the shallow crust, in the remainder of this paper, only brittle and semibrittle pressure-sensitive behavior of rock failure and fault slip are considered.

Framework for Addressing Rock Failure and Fault Strength

While sliding friction and rock failure can, in some instances, be described adequately by equation (13.1) with constant pressure dependence, more usually, rock failure and friction have a nonlinear pressure dependence. Furthermore, without additional information, equations such as equation (13.1) provide little insight into why particular rock types have high strength or high internal friction μ_f. Another drawback is that simple threshold failure relations do not predict failure time well, particularly at natural low loading rates. In addition, sliding stability is not addressed by relations such as equation (13.1). Seismic stress drop requires a loss of strength sufficiently rapid with shear strain to radiate seismic energy. If instead, the failure relation accounts for the size of the strength loss, the rate and time dependence of failure and the loading/unloading characteristics of the fault system, the fault properties necessary for seismic slip can be established.

To describe low-temperature rock failure and fault slip a simple physical model, similar to *Mogi* [1974] and *Savage et al.* [1996] can be used. Assume that rock failure and fault slip involve only two kinematic actions: deformation of intact rock and relative motion between two rigid rock surfaces or fragments. The deformation of intact rock might involve some combination of fracturing and ductile flow, and it may occur on any scale, e.g., tensile fracture of a single particle within a fault gouge, or generating a throughgoing shear fracture in large intact mass. Similarly, the motion between rigid rock surfaces might represent sliding on a discontinuity at large or small scales, or slip between particles in a fault gouge, between large contacting asperities across a fault, or rolling contact between particles in a fault gouge. At any particular instant during

a failure test or fault slip experiment, the total fault or incipient fault area A is divided into two distinct areas: intact material with area A_i and strength τ_i that must be broken or otherwise inelastically strained to accommodate a further increment of fault creation or fault slip, and broken area. Within the broken area is area of asperity contact A_f across fractures or between fragments within the fractured rock, with strength τ_f. The remaining fractured area A_d is the area crossing open pore space. Because noncontacting area has no strength, the shear resistance is the sum of the intact resistance T_i and the contacting resistance T_f, the total shear resisting force is

$$T = T_i + T_f = A_i\tau_i + A_f\tau_f \tag{13.3a}$$

and the total resisting shear strength is

$$\tau = \frac{A_i\tau_i}{A} + \frac{A_f\tau_f}{A} \tag{13.3b}$$

Changes in shear resistance, for example due to changes in normal stress (fig. 13.2) or displacement (strain) (fig. 13.1a), are attributable to changes in one or more of A_i, τ_i, A_f and τ_f, and the general description of changes in shear resistance is

$$d\tau = \frac{\partial\tau}{\partial A_i}dA_i + \frac{\partial\tau}{\partial\tau_i}d\tau_i + \frac{\partial\tau}{\partial A_f}dA_f + \frac{\partial\tau}{\partial\tau_f}d\tau_f \tag{13.3c}$$

Depending on the conditions and material type, different terms in equation (13.3c) dominate. The subsequent discussion of laboratory observations of rock failure and rock friction, and constitutive equations will refer to the specific terms of equation (13.3c) thought to underlie changes in fault strength with displacement, time, and slip.

Rock Failure

This section summarizes processes underlying pressure dependence of rock failure strength and the cause of strain rate and time dependence of strength. The required conditions for failure with stress drop and those that lead to seismicity are illustrated using a simplified constitutive description.

Dilatancy

The source of pressure dependence of intact rock failure strength and the pressure dependence of fault sliding strength can be illustrated using equation (13.3c) [*Mogi*, 1974; *Savage et al.*, 1996]. If the shear strength of intact regions is a

material constant τ_s (the ultimate strength from single crystal deformation experiments [*Savage et al.*, 1996]) and the shear strength of contacting regions is a material constant τ_f, then changes in fault strength are due entirely to changes in contacting and intact area. For example, the pressure dependence

$$\frac{d\tau}{d\sigma_e} = \frac{\tau_i}{A}\frac{dA_i}{d\sigma_e} + \frac{\tau_f}{A}\frac{dA_f}{d\sigma_e} \tag{13.3d}$$

is due to increases with normal stress of either the intact area or the area of asperity contact within the broken regions. Both increases in intact area and contact area can only occur at the expense of dilatant volume.

Consistent with the qualitative representation (equation (13.3d)), pressure dependence of the failure strength (fig. 13.2) in rock failure tests is thought to be due to inelastic dilatancy, the generation of open (mode I) microcracks, fracture networks, and granular comminuted rock. Dilatancy reduces the contacting area within the highly stressed rock volume, ultimately across the incipient fault plane. Dilatational strain requires work done against the normal stress across the incipient fault or against confining stress, e.g., $\sigma_3 \int d\varepsilon_v$. Thus work necessary to weaken the fault to the point of failure increases with confining pressure, and the failure strength is confining pressure dependent. In most cases, because pressure dependence decreases with increasing confining pressure (figs. 13.2b and 13.2c), the "ease of dilatancy" decreases with increasing pressure (also see Chemical Effects of Pore Fluid section).

Some aspects of the dilatant volume associated with failure are seen in laboratory tests where volume strain is measured as differential stress is increased to failure at constant confining pressure (fig.13.4) [*Brace et al.*, 1966]. Initially, the volume decreases with increasing stress, reflecting elastic compression. For highly porous rock (not shown), there is additional inelastic compaction due to pore collapse [e.g., *Wong*, 1990]. Eventually, at high stress, open pores, contrasts in elastic properties of adjacent minerals and small amounts of slip at weak grain boundaries act as stress concentrators [*Peng and Johnson*, 1972; *Tapponnier and Brace*, 1976], producing large local stresses [*Peng and Johnson*, 1972; *Horii and Nemat-Nasser*, 1986; *Sammis and Ashby*, 1986; *Ashby and Sammis*, 1990; *Lockner et al.*, 1992]. The local stresses contain a component of tension that induces dilatant crack propagation. The onset of measurable dilatancy is shown as C′ in figure 13.4. As crack density increases, cracks begin to interact and a protofault nucleates: a shear fracture connecting en echelon arrays of the dilatant microcracks [*Peng and Johnson*, 1972; *Horii and Nemat-Nasser*, 1986; *Sammis and Ashby*, 1986; *Costin*, 1987; *Kemeny and Cook*, 1987; *Ashby and Sammis*, 1990; *Du and Aydin*, 1991; *Lockner et al.*, 1992; *Reches and Lockner*, 1994]. At this point, labeled C in figure 13.4, a macroscopic fault propagates in-plane owing to its own stress field usually with continuing dilatancy [*Lockner et al.*, 1991, 1992]. The amount of dilatancy prior to failure increases with porosity [*Brace*, 1978].

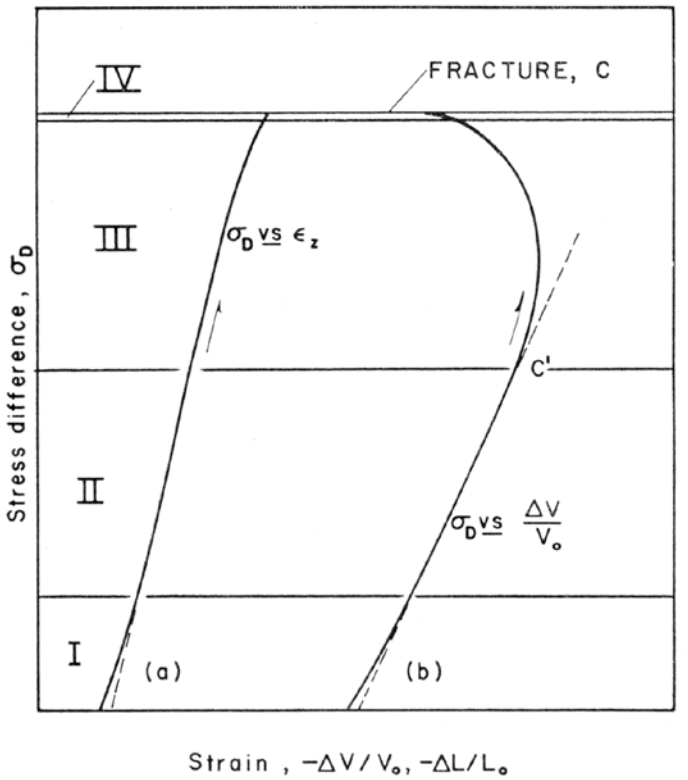

Figure 13.4 Strain and dilatancy during brittle failure [from *Brace et al.*, 1966]. Differential stress (stress difference) versus two strain measures; at left (a) is axial strain and at right (b) is the volumetric strain. Axial strain and differential stress are defined in the caption to figure 13.1. Volumetric strain is the sum of the axial strain, and twice the radial strain of the cylindrical sample; volumetric strain is also defined as $(V - V_0)/V_0$, where V is sample volume and V_0 is the initial volume. The horizontal lines define different parts of stress strain behavior. Region I is a nonlinear elastic region associated with closing open fractures. Region II is linear elastic with compressive volumetric and axial strain. Region III is the inelastic region associated with dilatant cracking and large volume increase. C′ marks the onset of region III. Region IV is that of macroscopic fracture and failure occurs at C.

In weak phyllosilicate rocks, weak pressure dependence reflects low dilatancy [*Escartin et al.*, 1997]. For example, anitigorite and lizardite serpentinites are markedly weaker than nonhydrous silicate rocks such as granite and dunite ($\mu_f = 0.73–0.43$), and serpentinites have lower pressure dependence $\mu_f = 0.35$. The difference in pressure dependence indicates low bulk dilatancy (fig. 13.5, compare with fig. 13.4). As serpentine has weak [001] cleavage, shear is accommodated preferentially along these cleavage surfaces resulting in crys-

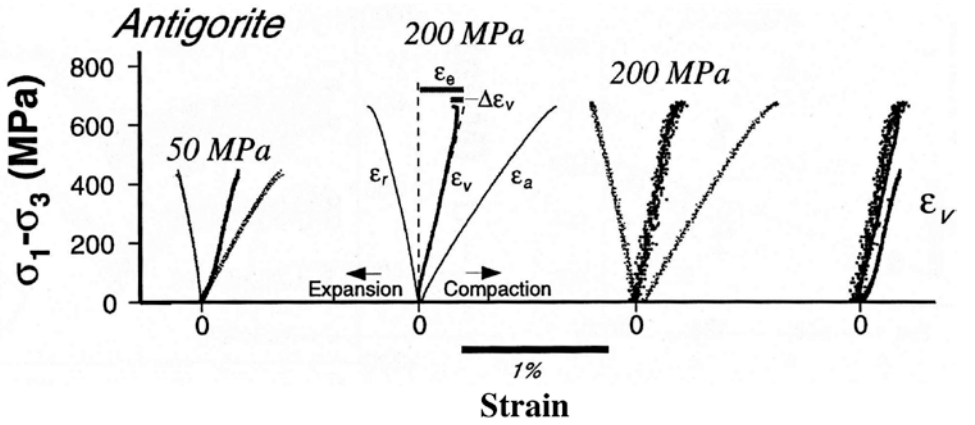

Figure 13.5 Strain and dilatancy during failure of weak serpentine [from *Escartin et al.*,1997]. Differential stress versus axial, radial, and volumetric strain measures for three experiments, one at 50 MPa confining pressure and two at 200 MPa. The volumetric strains for all three cases are superimposed at right. Axial strain (here ε_a) and differential stress are defined in the caption to figure 13.1. Volumetric strain (ε_v) is defined in the caption to figure 13.4. Radial strain is $(r - r_0)/r_0$, where r is cylinder radius and r_0 is the initial radius. Volumetric strain is constructed from the measured values of ε_a and ε_r as described in the caption to figure 13.4. The net volumetric strain at failure (coinciding with the peak stress) is compaction, as opposed to the strong material shown in figure 13.4 that shows net dilatancy.

tallographically controlled (nonopening) mode II shear fractures. Deformed serpentinite has scarce mode I cracks that produce the strong pressure dependence in quartzofeldspathic rock. Dilatancy that does occur in serpentinite is restricted to rigid motion owing to roughness along the shear planes [*Escartin et al.,* 1997] and in dilatant jogs within regions of shear step-over.

Anisotropy and Failure Strength

The comparison between serpentines [*Escartin et al.*, 1997] and quartzofeldspathic rocks [*Brace et al.,* 1966] suggests that weak pressure dependence and intrinsic material weakness are associated with low dilatancy and strong pressure dependence with high dilatancy. This causal relationship is consistent with the failure strengths of other rocks and minerals with strongly anisotropic material properties at low temperature and low stress, e.g., foliated metamorphic rocks, schists, and gneisses [*Shea and Kronenberg*, 1993], shale ($\mu_f = 0.33$ [*Donath*, 1961], $\mu_f = 0.3$ [*Ibanez and Kronenb*erg, 1993]), and muscovite single crystals ($\mu_f = 0.4$ [*Mares and Kronenberg*, 1993]). The experiments on muscovite single crystals illustrate that preferred orientation (p.o.) of anisotropy and the geometric relationship between the p.o. and the principal stress directions also are involved in pressure dependence and weakness (fig. 13.6). If the musco-

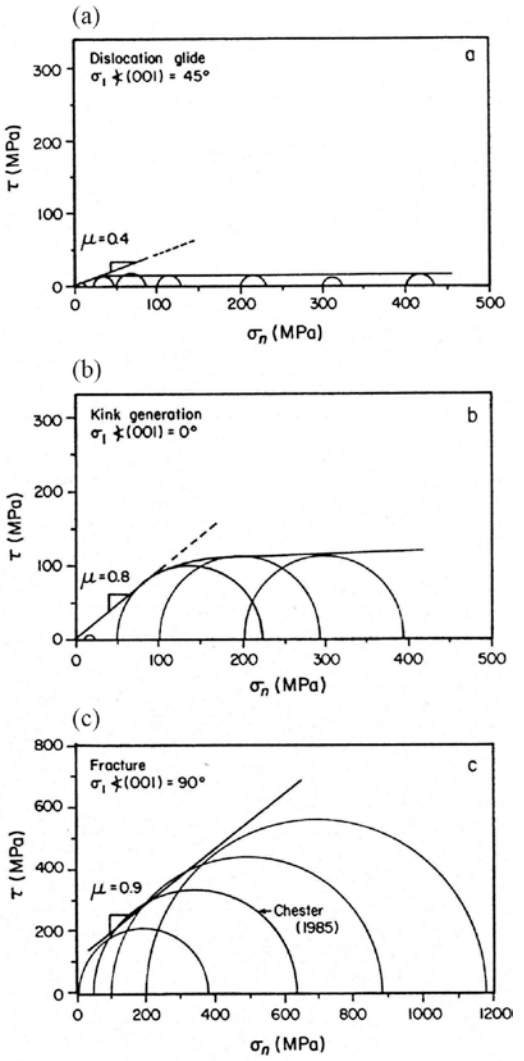

Figure 13.6 Effect of stress orientation on strength of "weak" material. Strength of muscovite single crystals in three different orientations. Reprinted from Journal of Structural Geology, 15, *Mares and Kronenberg*, Experimental deformation of muscovite, 1061–1075, Copyright (1993), with permission from Elsevier. Schematics at left show the orientation of the basal cleavage [001] with respect to a vertical greatest principal stress σ_1. At right are the Mohr diagrams corresponding to deformation tests at different confining pressures in these orientations. (a) σ_1 at 45° to [001]. Sample is weak in a relative sense with low-pressure dependence, and absolutely weak in the sense that the transition to the plastic regime occurs at 50 MPa. (b) σ_1 at 0° to [001]. Sample is stronger in the relative and absolute senses; pressure dependence is twice that in figure 13.6a, and the transition to the plastic regime occurs at twice the normal stress. (c) σ_1 at 90° to [001]. Sample is extremely strong with pressure dependence larger than quartzofeldspathic rocks, and the transition to the plastic regime occurs at higher than the maximum testing strength (>400 MPa normal stress).

vite cleavage direction [001] is aligned 45 to greatest principal stress, then the pressure dependence is weak (μ_f = 0.4) and the transition to the pressure-independent regime, here controlled by dislocation glide, occurs at <50 MPa. If instead the cleavage is parallel to σ_1, the pressure dependence is twice as large (μ_f = 0.8) and the transition to the pressure-independent regime occurs at between 100 and 150 MPa. Furthermore, if the cleavage is perpendicular to σ_1, then muscovite is extremely strong, has very high pressure dependence (μ_f = 0.9), and the transition to true ductile shearing occurs at stresses higher than attained in the highest stress tests >750 MPa. In this severely misoriented regime the sample fails by brittle fracture accompanied by significant stress drop. Similar anisotropy of failure strength is seen in shale [*Donath*, 1961], schists, and phyllities [*Shea and Kronenberg*, 1993]. So even intrinsically weak minerals can be very strong, and strongly dilatant in polycrystalline form if there is no p.o. or if there is a p.o. but the fabric is misoriented with respect to the stress field. Observable intrinsic weakness in rocks therefore requires anisotropy, preferred orientation of the anisotropy, and that the fabric is aligned optimally for failure.

Failure With Strength Loss

Under certain pressure and temperature conditions for many materials, faulting of intact rock is associated with strength loss. Other materials can fail at the same conditions with no stress drop at all; these different responses reflect differences in microscopic behavior. Strength loss during failure of intact rock is expected if the fault sliding strength is lower than the incipient fault strength (e.g., fig. 13.2) or if the fault sliding strength is slip rate dependent. Here, the focus is on the former; the latter case is discussed below. If the processes associated with fault formation produce a fault that is weaker than the incipient fault, then a peak strength is followed by strain weakening. At low pressure the strength of preexisting faults (see below) is usually lower than the peak strength in an intact failure test; thus strength loss is expected at low confining stress for most materials.

The physical process underlying the strength loss can be rationalized by using equation (13.3). Again, taking the intact and contact strengths as material constants, the difference between the failure strength τ^p and the residual sliding strength τ^r of a failure test involves differences in the intact and asperity contact areas

$$\Delta\tau = \tau^p - \tau^r = \frac{\tau_i}{A}(A_i^p - A_i^r) + \frac{\tau_f}{A}(A_f^p - A_f^r) \tag{13.4}$$

where the superscripts *p* and *r* refer to the peak and residual values. For equation (13.4) both the peak and residual strengths involve resistance due to con-

tributions from intact rock and sliding contact [*Mogi*, 1974; *Savage et al.*, 1996]. The contribution of intact resistance to residual strength is justified by laboratory results where wear debris and gouge are always observed as by-products of fault slip on preexisting faults and initially clean joint surfaces. Nonzero strength loss requires net reduction of intact and contacting area, which cannot occur unless dilatant volume is generated during the strength loss. So strength loss, like the pressure dependence of failure strength, is due to dilatancy, reflecting weakening due to shear-induced reduction of intact and contacting area across the fault surface.

To illustrate the tacit correlation between the strength loss, here measured as change in friction (see caption), and the pressure dependence of failure strength are data from selected rock failure tests on schist [*Shea and Kronenberg*, 1993], Berea sandstone [*Bernabe and Brace*, 1990] and gabbro [*Wong*, 1986] (fig. 13.7). For a particular rock type, the strength loss is a fraction of the pressure dependence, and as the pressure dependence decreases, the strength loss decreases. The implication is that low pressure dependence results from low dilatancy and any associated strength losses during faulting are small. The clearest expression of this expected relation between pressure dependence and strength loss for any particular rock is at the transition to truly ductile behavior where both the pressure dependence and the strength loss must vanish.

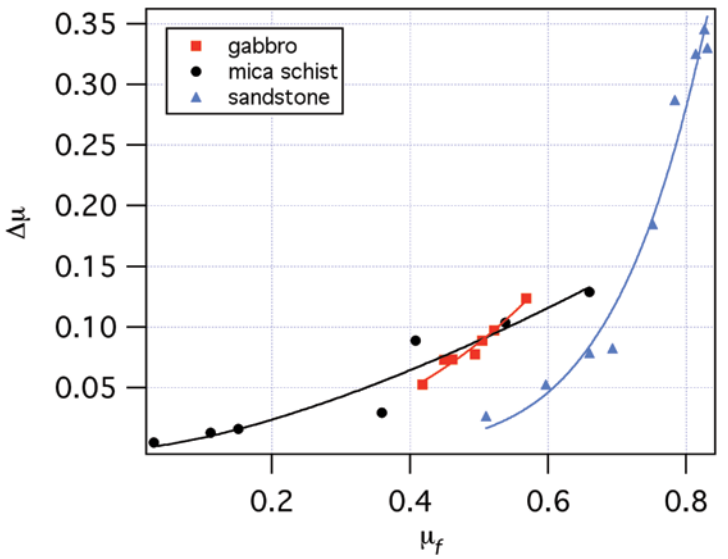

Figure 13.7 Relations between strength drop $\Delta\mu$ and pressure dependence $\mu_f = \partial\tau/\partial\sigma_e$ from failure tests for three rock types. These are the same experiments shown in figure 13.2. The strength drops are expressed as changes in friction between the peak strength and the residual strength, accounting for the change in normal stress that accompanies the strength loss. The pressure dependence was estimated from the failure envelope (fig. 13.2).

The transition with increasing confining pressure from the brittle strain weakening response to ductile deformation can be a transition to semibrittle deformation [e.g., *Escartin et al.,* 1997] or to a pressure-independent regime [e.g., *Shea and Kronenberg*, 1993]. For quartzofeldspathic rocks, strength loss can persist to high confining stresses [e.g., *Byerlee*, 1968]. In anisotropic material with preferred orientation the transition occurs at much lower pressure (e.g., fig. 13.6a). In any case, the transition from the strain-weakening regime is associated with reduction in the pressure dependence or elimination of the pressure dependence. Mechanistic and stress-strain behavior spanning the brittle-ductile transition are summarized in figure 13.8, and readers are directed to the review paper by *Evans et al.* [1990] for additional details.

In characterizing fault strength during failure it is important to recognize that stress threshold models of failure such as equation (13.1) do not relate well to the processes that determine the timing and occurrence brittle failure. In particular, microcrack initiation and growth produces the accelerating inelastic dilatancy that precedes failure (fig.13.4). There is measurable precursory

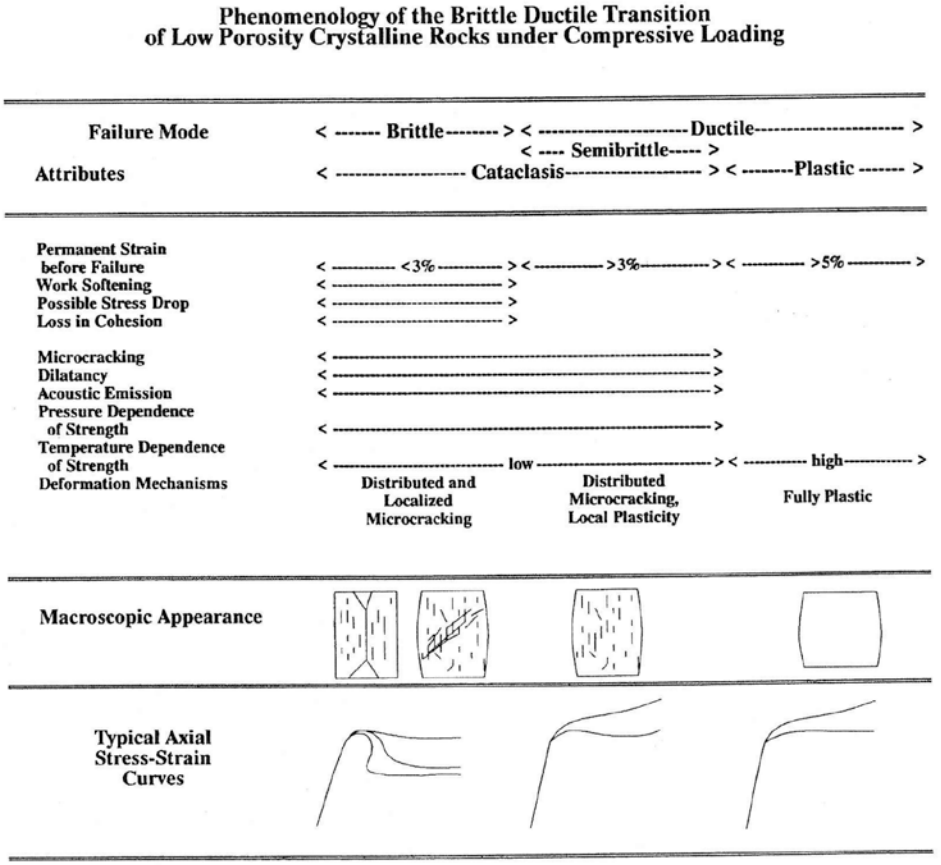

Figure 13.8 Rheological, mechanistic, and microstructural characteristics of the brittle-ductile transition. Figure from the comprehensive review of *Evans et al.* [1990].

inelastic creep prior to the peak strength and significant displacement associated with the postpeak loss of strength (fig. 13.4). Thus the loss of strength is not instantaneous at a strain or displacement threshold, and the weakening associated with fault formation is gradual, involving a displacement or strain length scale. To determine the seismic potential of faulting, the displacement rate of weakening is key.

Second-Order Effects on Strength

That rock failure is not abrupt in strain (fig. 13.4) requires it also to be gradual in time. As shown in figure 13.9, failure is delayed. There is lag time between

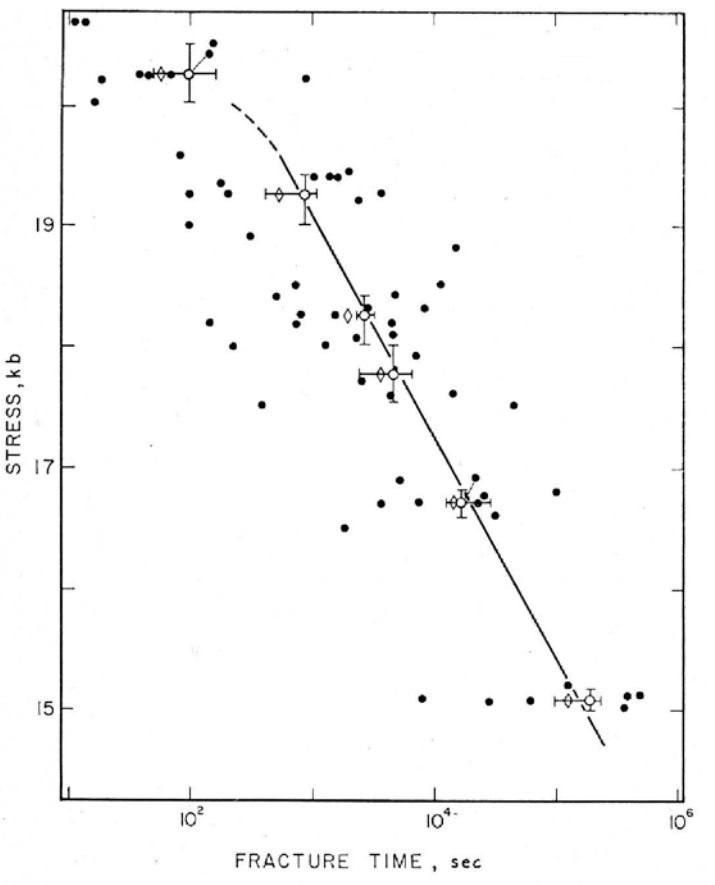

Figure 13.9 Dependence of failure time on stress from experiments on quartz single crystals in water at room temperature. Figure from *Scholz* [1972]. In these tests at ambient conditions a uniaxial stress sufficient to induce failure is applied and held constant until failure occurs. This is the phenomenon known as static fatigue. Solid symbols are individual failure tests. The open symbols are the mean failure times with error bars, and the open triangles are median failure times. The line is a fit to the means.

the application of a critical stress and the time of failure. This delay originates from a small viscous component to rock strength. At constant loading rate and low temperature, rock failure strength and creep strength depend weakly and logarithmically on the loading strain rate approximately following the empirical relationship [e.g., *Rutter,* 1974; *Lockner*, 1998]

$$\dot{\varepsilon} = \dot{\varepsilon}_o \exp(\tau - \tau_o / \mathbf{A}) \tag{13.5a}$$

reflecting an underlying strain rate dependent deformation mechanism. The empirical constant **A** scales the size of the rate dependence. Because of the role of microcracking in rock failure, many studies, dating to *Scholz* [1968c] have related the rate dependence (equation (13.5a)) to the growth rate of single tensile cracks in double-cantilever experiments on glass [e.g., *Lawn*, 1993] and single mineral crystals [*Atkinson*, 1984]. Figure 13.10 shows examples of this "subcritical" behavior, rate data from single cracks propagating in fused silica glass, [*Lawn*, 1993], synthetic quartz, and Westerly granite [*Atkinson and Meredith*, 1987]. In figure 13.10 the horizontal axis is crack propagation velocity and the

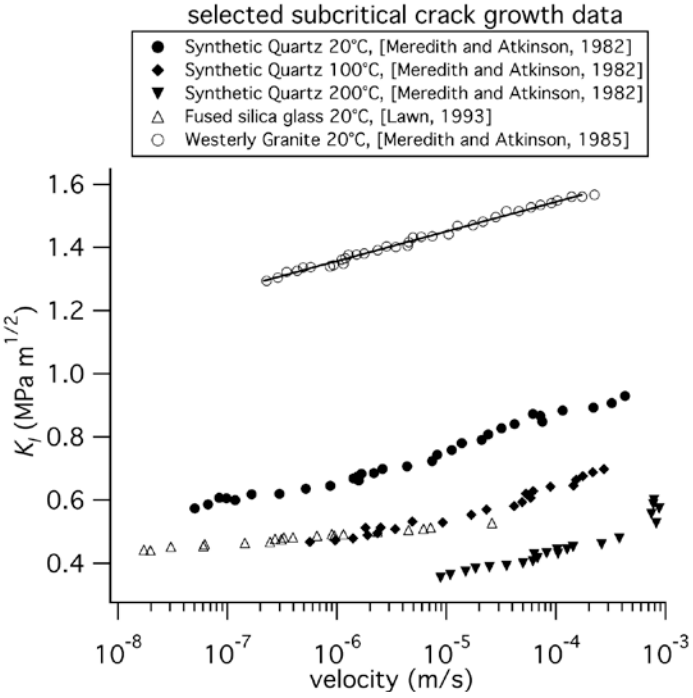

Figure 13.10 Subcritical crack growth. Crack stress intensity K_I versus velocity for fused silica glass [*Lawn*, 1993], synthetic quartz [*Atkinson and Meredith*, 1987a], and Westerly granite [*Atkinson and Meredith*, 1987a]. The stress intensity is proportional to the remotely applied stress; thus the vertical axis reflects the driving stress for subcritical crack extension. Also shown is a fit to the granite data using $K_I = K_0 + \xi \ln V$, with $\xi = 0.041$ MPa m$^{1/2}$.

vertical axis is the stress intensity K_I; stress intensity is related to the remotely applied driving stress σ_r and to the crack length c as $K_I \propto \sigma_r\sqrt{c}$. Subcritical fracture growth has a nonlinear viscous rheology; as the stress on the sample increases, crack velocity increases, or alternatively, as the crack propagation velocity increases, the crack strength increases. There is temperature dependence indicating that a thermally activated mechanism controls growth. Arguably, subcritical crack growth occurs in all instances of natural faulting and in laboratory rock fracture as indicated by damage such as pervasive dilatant and shear microcracks, macroscopic fracture, and wear material (gouge).

For well-studied minerals and for other brittle materials, propagation rate is determined by the rate of chemical reaction at the crack tip (the rate at which chemical bonds are broken) [*Charles and Hillig*, 1962; *Atkinson and Meredith*, 1987a] following [*Charles and Hillig*, 1962]

$$v = v_o \exp\left(\frac{-E + \Omega\sigma_t - \Omega_m\Gamma/\rho}{RT}\right) \tag{13.5b}$$

where T is temperature in degrees Kelvin, E is the stress free activation energy, Ω is the activation volume, Ω_m is molar volume, Γ is the interfacial energy, R is the gas constant (8.3144 J/mol °K), and ρ is the radius of curvature at the crack tip. The dependence of rate on stress has the same form as the empirical relationship (equation (13.5a)), and precursory creep and volumetric strain observed in rock failure tests [*Scholz*, 1968a; *Lockner*, 1998] are expected from the collective growth of many subcritical fractures.

Precursory Creep and Static Fatigue

Accounting for a rate-dependent strength, equation (13.5) produces much better simulations of laboratory observations than threshold models such as equation (13.1). Observations such as slow, controlled strength loss (fig. 13.1) or rapid seismic strength loss (fig. 13.11) can be characterized using an equation for fault strength (constitutive relation) and one for elastic interaction with the surroundings. The fault strength relation accounts for the reduction of contact area by progressive dilatancy and for the second-order strain-rate dependence,

$$\begin{aligned} \tau &= \tau^r + \frac{\Delta\tau(d_* - \delta)}{d_*} + \mathbf{A}\ln\frac{V}{V_L} \qquad \delta < d_* \\ \tau &= \tau^r + \mathbf{A}\ln\frac{V}{V_L} \qquad\qquad\qquad\quad \delta \geq d_* \end{aligned} \tag{13.6a}$$

The first term on the right side is the residual resistance of the fault sliding at the loading rate V_L. For slip less than d_*, the second term is the fault strength

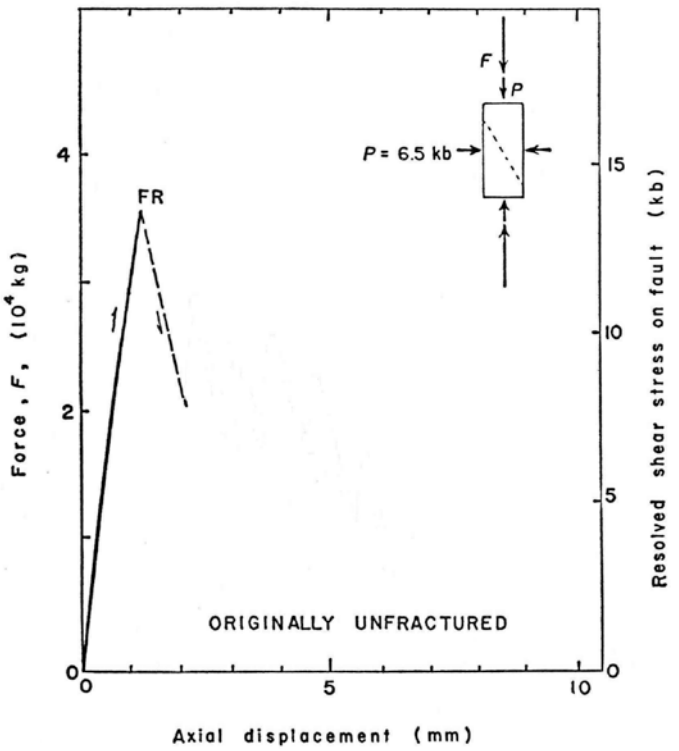

Figure 13.11 Rock failure with rapid slip and seismic radiation. Reprinted with permission from Science, 153, *Brace and Byerlee*, Stick-slip as a mechanism for earthquakes, 990–992, Copyright [1966] AAAS. This is the force displacement record during failure of granite at 650 MPa confining pressure. Stress drop occurs at the point labeled FR; subsequent motion of the fault and the loading system during the stress drop is uncontrolled, and the stress drop occurs effectively instantaneously. The dashed line connects the measurements before and after the rapid slip event.

loss due to dilatancy, represented by slip weakening, which operates over the characteristic displacement d_*. The weakening relationship is linear, as most often assumed in representations of material and earthquake failure [*Ida*, 1972; *Palmer and Rice*, 1973], dynamic rupture modeling [*Andrews*, 1976], and in some laboratory-derived friction representations [*Dieterich*, 1992]. $\Delta\tau$ is the strength loss associated with fault formation. The other term represents the viscous effect having same form as observed in subcritical crack growth experiments [*Atkinson*, 1984] (fig. 13.10) and in rock failure tests (equation (13.5a)) [*Scholz*, 1968c; *Lockner*, 1998]. The strain rate dependence of rock strength is a second-order effect, e.g., having a value $d\tau/\sigma_e d\ln V$ of 0.008 to 0.022 for granite [*Lockner*, 1998] compared to the failure strength τ/σ_e = 1.5 to 0.6 between 300 and 2000 MPa normal stress [see *Savage et al.*, 1996]. Equation (13.6a) is intended to be illustrative, but it may be useful for quantitative analysis as well.

An elastic element is used to describe the elastic loading and unloading behavior of the fault surroundings [*Dieterich*, 1978a, b]. Elastic coupling of the fault to the surroundings is through a stiffness k. The stress $\boldsymbol{\tau}$ supplied to the fault is specified by assuming a constant loading rate V_L and inertia is ignored:

$$\boldsymbol{\tau} = k(\delta_L - \delta) \tag{13.6b}$$

δ_L is the loading displacement $\delta_L = tV_L$, and δ is fault slip. In laboratory experiments, stiffness is the combined stiffness of the intact portion of the sample and the testing apparatus, whereas in the Earth the stiffness is related to the elastic modulus of the rock and for simple representations is inversely proportional to the characteristic dimension of the portion of fault that is slipping [e.g., *Byerlee*, 1970; *Walsh*, 1971; *Dieterich*, 1978a; *Dieterich*, 1979].

Equating the fault strength τ (equation (13.6a)) with the fault stress $\boldsymbol{\tau}$ (equation (13.6b)) well illustrates the range of behavior seen in laboratory faulting experiments, for example fault generation under conditions of strain neutral creep, faulting with controlled strength loss, and seismic faulting (fig. 13.12). These example simulations are conducted at identical conditions using different values of the strength loss. In the case of faulting with no observed stress drop the entire strength loss $\Delta\tau$ is accomplished during the prepeak creep while the fault slip rate is simultaneously accelerating. In this case the $\mathbf{A}\ln V$ term in equation (13.6a) entirely masks the strength loss. For stable stress drop the strength loss is complete before the slip rate reaches seismic slip rates.

Precursory creep and delayed failure in laboratory failure tests result in a related phenomenon known in mechanical engineering, material science, and rock mechanics as static fatigue (fig. 13.9), an inherent time delay between the application of a stress increase and the occurrence of rock failure induced by the stress change [e.g., *Griggs*, 1936; *Scholz,* 1972; *Kranz*, 1980]. Static fatigue behavior is predicted by (equation (13.6a)). In a fatigue test, stress is raised to a particular level τ_s at time $t = 0$ and then held constant; the sliding rate evolves from the starting velocity V_s at $t = 0$ according to

$$V = \frac{V_s \mathbf{A} d_*}{\mathbf{A} d_* - \Delta\tau t V_s} \tag{13.7a}$$

where $V_s = V_* \exp[(\tau_s - \tau^r - \Delta\tau)/\mathbf{A}]$ and V_* is an arbitrary slip velocity (fig. 13.13). The delay time t_d between the application of the stress that induces failure and actual time of failure is

$$t_d = \frac{\mathbf{A} d_*}{\Delta\tau V_*} \exp[(\tau_s - \tau^r - \Delta\tau)/\mathbf{A}] \tag{13.7b}$$

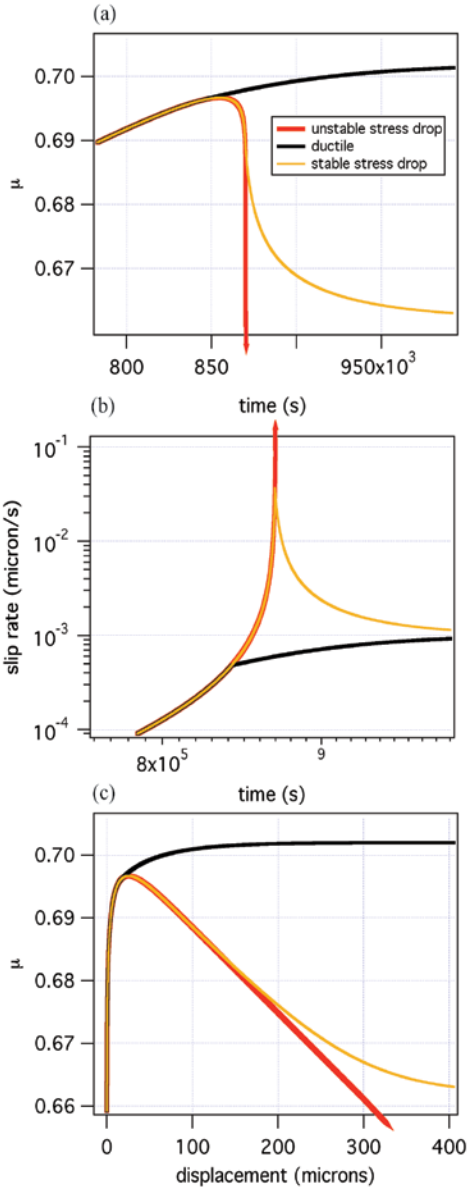

Figure 13.12 Characteristics of simulated laboratory failure with the failure relationship equation (13.6). Three cases corresponding to ductile (black), semibrittle (yellow), and brittle (red) are calculated with σ_n = 100 MPa, k = 0.01 MPa/μm, V_L = 0.001 μm/s, τ_0 = 70 MPa, A = 0.8 MPa, $\Delta\tau/d_* = 0.06$ MPa/μm, and an initial slip rate of 1×10^{-10} μm/s. For the ductile case the strength loss is $\Delta\tau$ = 1 MPa, and stress drop is progressively larger for the semibrittle ($\Delta\tau$ = 5 MPa) and brittle ($\Delta\tau$ =30 MPa) cases. (a) Friction (τ/σ_n) versus time. As the parameters are the same except for the slip weakening term in equation (13.6), the calculations follow the same stress-strain path until the net slip becomes significant and the paths diverge. For the brittle case the stress drops rapidly in an uncontrolled fashion. For the semibrittle case, strength drops rapidly initially but is damped. The ductile response is monotonic. (b) Slip velocity versus time. (c) Friction versus displacement.

Longer delay times result from smaller stress changes. If earthquake failure is controlled by the same processes as in laboratory rock failure, the failure time of an earthquake triggered by a particular stress change depends on the size of stress change and on how close the fault is to failure prior to the stress change (proximity to failure). That rock failure time that is related to stress change in this way has been known since *Griggs* [1936]. Figure 13.13 shows static fatigue of granite [*Kranz*, 1980].

As the relationship between stress change and failure time is nonlinear, when one considers populations of faults with an initially random distribution

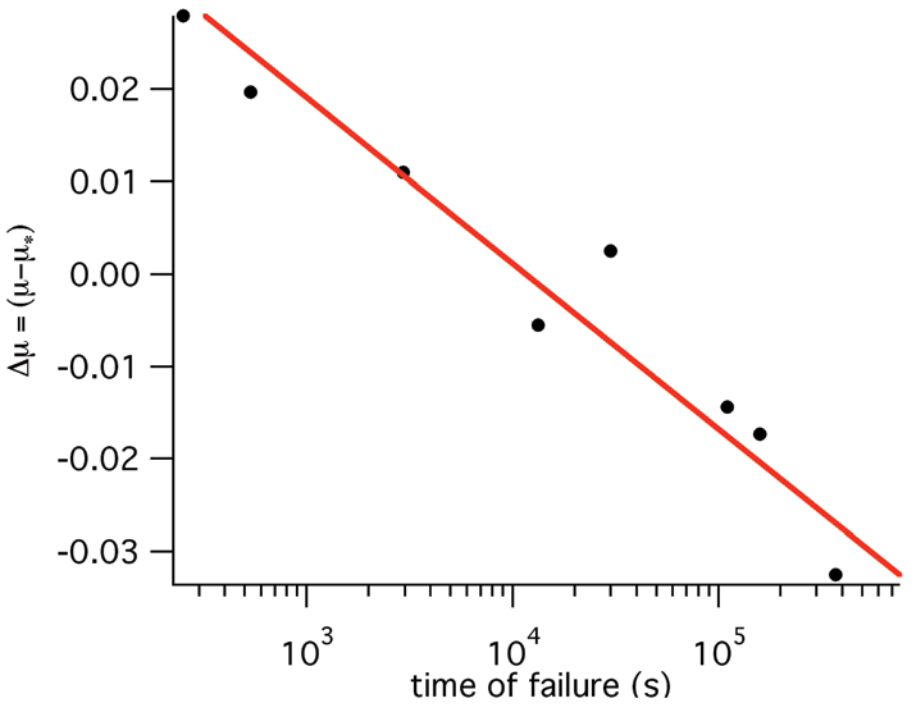

Figure 13.13 Model fit to static fatigue data. Experimental static fatigue data from rock fracture of granite at room temperature and 53 MPa confining pressure [*Kranz*, 1980]. Failure stress was converted to friction assuming a 30° angle between the greatest principal stress and the incipient failure plane. $\Delta\mu$ was calculated using μ at 10^4 s as the arbitrary reference μ_*. Shown is a fit using equation (13.7b), which produces a value of $\mathbf{A}/\sigma_n = 0.0078$.

of proximity to failure, a stress change produces a seismicity rate due to triggered events that is initially very high and decreases with time following the stress change. This is the behavior seen in induced acoustic emissions, microseismicity, and Omori aftershock sequences, as was noted by *Mogi* [1962], and subsequently by many researchers [e.g., *Scholz*, 1968b; *Knopoff*, 1972; *Das and Scholz*, 1981; *Yamashita and Knopoff*, 1987; *Hirata*, 1987; *Reuschle*, 1990; *Marcellini*, 1995, 1997]. Many of these authors have developed fracture growth based models of aftershocks.

Conditions for Seismic Failure

Accelerating deformation rate is only possible if strength drops so that stored elastic energy from the surrounding rock can be used to drive further deformation. Accelerating slip rate depends on inequality between strength and the stress available to drive shear deformation, which is supplied by the loading

system. In the laboratory the test sample, piston, and load frame store elastic energy just as the brittle crust stores energy around a fault during tectonic loading. When the yield strength is reached, deformation will commence and stored elastic energy is converted to frictional heat or surface energy as the fault zone shears. If an increment of deformation reduces the strength faster than the driving stress is reduced, an unstable condition develops in which deformation can accelerate into an earthquake and some of the stored elastic energy is radiated as seismic waves [*Byerlee*, 1970; *Dieterich*, 1979].

The conditions that distinguish faulting with seismic strength loss from aseismic slip can be deduced directly from equation (13.6) by equating equations (13.6a) to (13.6b). The rate of stress change with displacement from equation (13.6b) is $d\boldsymbol{\tau}/d\delta = k(V_L/V - 1)$. So, if the fault is sliding faster than V_L, the stress is decreasing; if sliding is slower than V_L, stress increases. The displacement rate of strength change at constant sliding velocity from equation (13.6a) is $\partial\boldsymbol{\tau}/\partial\delta = -\Delta\tau/d_*$. Equating the rate of strength change with the rate of stress change gives

$$k = \frac{\dot{\tau}}{V} + \frac{\Delta\tau}{d_*} \tag{13.8a}$$

where the stressing rate $\dot{\tau} = kV_L$. Remember that constant slip rate is assumed in equation (13.8a), so equation (13.8a) is the stiffness that allows constant slip rate given a particular stressing rate and displacement rate of strength loss [see also *Dieterich*, 1992]. As all terms of equation (13.6c) are positive, if $\Delta\tau/d_* > k$, then the equality (13.8a) cannot possibly be met. Under this circumstance the slip rate is not constant and increases to increase the fault strength through the $\mathbf{A}\ln V$ term in equation (13.6a). However, because the elastic reduction in stress with slip k is smaller than the strength loss $\Delta\tau/d_*$, each increment of slip requires a further increase in slip rate to maintain stress (equation (13.6b)) equivalent to strength (equation (13.6a)). This is the recipe for accelerating slip rate, possibly to seismic rates. Thus

$$\Delta\tau/d_* > k \tag{13.8b}$$

is a necessary condition for seismic stress drop. In the rock friction literature an unbounded increase in slip rate with slip is referred to as a slip instability [e.g., *Rice*, 1983; *Rice and Ruina*, 1983; *Ruina*, 1983] and for linearly and approximately linear slip weakening relations, equation (13.8b) is considered the necessary condition for earthquake nucleation. This condition for instability can also be illustrated graphically (see fig. 13.14).

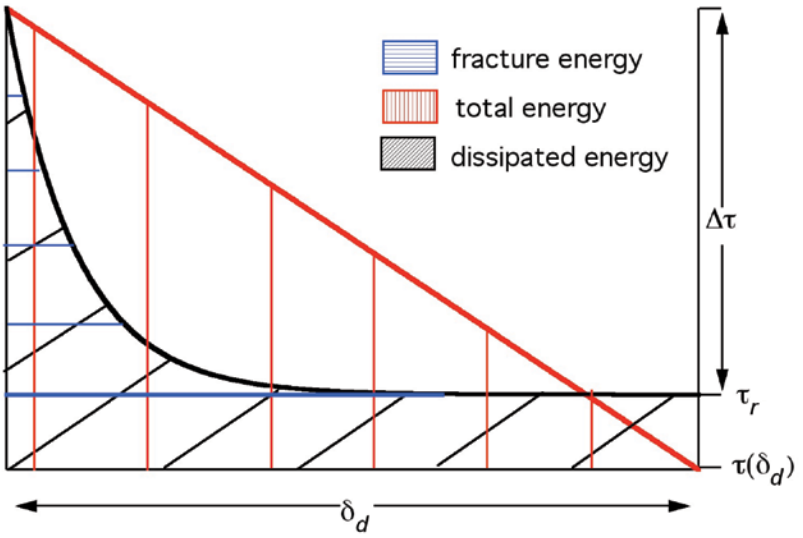

Figure 13.14 Schematic diagram showing the energies per unit fault area (e.g., Joules/m^2) released and dissipated during strength loss in a laboratory experiment. Energy per fault area can be expressed equivalently as stress times displacement; stress and displacement are the axes of the figures, and the energy/fault area corresponds to an area on the plot (e.g., the blue hatched region which corresponds to fracture energy). The displacement rate of stress drop is fixed by the machine stiffness (heavy red line); the area under this stress line is the total energy released per unit fault area. The strength loss (heavy black line), which can occur more rapidly with displacement than the stress drop, defines the energy dissipated by fault slip, and the effective shear fracture energy G_e (blue horizontal hatching), The effective shear fracture energy is the portion of dissipated energy associated with the strength loss. The requirement for earthquake nucleation, equation (13.9d), is illustrated here graphically. For nucleation to occur the total energy must exceed the dissipated energy; in other words, the red area exceeds the black area.

Effective Shear Fracture Energy In instances where the strength loss with displacement is not linear, a more general condition can be derived from an energy balance. For slip acceleration the total work W accomplished in dropping the stress in the source region must exceed that absorbed or dissipated in the fault zone E_f, $W - E_f > 0$. The energy difference $W - E_f$ is the energy available to accelerate the slip rate and to be radiated as seismic energy. Ignoring small amounts of dilatancy, the total work (energy per unit fault area) is

$$W = \int_{\delta_o}^{\delta_d} \tau d\delta \tag{13.9a}$$

This stress drop is accomplished in some displacement δ_d. The total work can be divided into that associated with the stress drop and the energy $\boldsymbol{\tau}(\delta_d)\delta_d$. The partitioning is shown in the stress versus displacement diagram (fig. 13.14). The total energy released (in Joules/m^2 = Pa m), is the area under the heavy red line. That associated with the stress drop is the area $k\delta_d^2/2$.

The energy absorbed in the fault zone consists of shear-generated heat and that of inelastic processes such as ductile yielding and creation of new surface area by fracturing. These dissipative energy changes per unit area within the fault zone can be represented by changes in the shear resistance integrated over the total displacement

$$E_f = \int_{\delta_o}^{\delta_d} \tau d\delta \tag{13.9b}$$

If the collective energy E_f is divided into the energy associated with the strength loss G_e and the energy τ_r associated with sliding the residual strength, then G_e is defined as [*Rice*, 1980]

$$G_e = \int_{\delta_o}^{\delta_d} \tau d\delta - \tau_r \delta_d \tag{13.9c}$$

With reference to figure 13.14, the effective shear fracture energy G_e is the hatched region; the energy expended in dropping the fault strength from a failure strength $\boldsymbol{\tau}_f$ to the residual strength τ_r. The energy difference is $W - E_f = k\delta_d^2/2 + \boldsymbol{\tau}(\delta_d)\delta_d - \tau_r\delta_d - G_e$, and the necessary requirement for earthquake nucleation is

$$k\delta_d^2/2 + \boldsymbol{\tau}(\delta_d)\delta_d > \tau_r\delta_d + G_e \tag{13.9d}$$

Equation (13.9d) can be rewritten without explicit reference to the residual strength and residual stress as

$$k > 2\left(\Delta\tau/\delta_d - G_e/\delta_d^2\right) \tag{13.9e}$$

For linear slip weakening, this expression is equivalent to equation (13.8b).

The fracture energy concept in laboratory rock mechanics originates from the Griffith energy balance for tensile fracture [*Griffith*, 1920]. For a fracture to propagate, the energy release rate, the total energy per unit area of crack advance, must exceed the energy adsorbed by the creation of new surface area as the crack advances. The critical energy release rate G_c, so defined when the energy released equals the energy adsorbed, is thus the energy associated with inelastic breakdown processes of the material at the crack tip. In the case of

purely brittle behavior, G_c can be equated with the specific surface energy (the surface energy per unit area) Γ of the fractured material, $G_c = 2\Gamma/\Delta A$, where ΔA is the increment of surface area that is created as the crack advances. This shear fracture energy is often defined, as in equation (13.8), using a simple linear slip-weakening model where the fault strength drops from the failure strength to the sliding strength over a characteristic displacement d_*, defining a strength loss $\Delta\tau_d$ [*Ida*, 1972; *Palmer and Rice*, 1973]. So long as the spatial size of the breakdown region is small with respect to the crack dimensions, the energy per unit area of new surface created is $G_c = \Delta\tau_d d_*/2$ [*Palmer and Rice*, 1973], equivalent to G_e in figure 13.14.

However, despite its name, laboratory experiments and theory suggest that the effective fracture energy relevant to rock failure and the onset of unstable slip between rock surfaces results primarily from changes in fault strength with displacement, rather than energy dissipated by the creation of new surface area. If a rupture is thought of as a single ideal surface, the slip-weakening distance corresponds to the interatomic spacing [*Ida*, 1973] and is many orders of magnitude smaller than the d_* observed in laboratory shear fracture experiments. Furthermore, such small values of d_* will not give reasonable seismological predictions [*Ida*, 1973; *Andrews*, 1976]. By carefully accounting for the number and size of stress-induced microcracks during rock failure, *Wong* [1982] found that the total energy over the area of the fault A inferred from measured fault strength and inelastic strain during the breakdown, that is integrating to obtain the total energy associated with the shaded region in figure 13.14 ~ $\Delta\tau_d d_* A/2$, is 10–100 times greater than the energy stored in new fracture surface area $2\Gamma S_v w$, where S_v is the surface area per unit volume that is created as the crack advances, and w is the fault-zone width. In contrast, a similar comparison between a stress-strain estimate of fracture energy and an accounting for increased microcrack surface area during tensile fracture shows complete agreement [*Friedman et al.*, 1972]. Comparing the tensile case of *Friedman et al*. [1972] with *Wong* [1982] suggests that the difference between effective and true shear fracture energy seen by *Wong* [1982] is due to frictional heating associated with the breakdown, as shear heating should be much smaller during tensile fracture. For breaking intact rock, *Wong* [1986] found G_e to increase with increasing normal stress, as *Okubo and Dieterich* [1981] found for dynamic slip of a preexisting fault, confirming that the effective shear fracture energy is a pressure-dependent quantity.

The idea that effective shear fracture energy is due mostly to displacement-dependent changes in shear resistance, rather than the creation of fracture surface area, implies that models of laboratory-observed strength breakdown during fault slip are appropriate for use in simulating earthquake rupture nucleation.

Slip Rate For rock failure tests, the fault strength loss is bounded (fig. 13.1) and the acceleration can be limited to subseismic slip rates if the strength loss is not large enough. If the rate of strength reduction is fixed $d\tau/d\delta$, the maxi-

mum slip velocity associated with equations (13.6a) and (13.6b) depends on the strength loss as

$$V = \frac{V_s + \dot{\tau}/\gamma[1 - \exp(-\gamma\delta/\mathbf{A})]}{\exp(-\gamma\delta/\mathbf{A})]} \tag{13.9f}$$

where $\gamma = \Delta\tau/d_* - k$. Slip rate depends nonlinearly on the strength loss and to achieve seismic slip velocities during rock failure a sufficient loss is needed.

In summary, earthquake nucleation involving the failure of intact rock requires strength loss more rapid with slip than the unloading stiffness of the surroundings (equation (13.8b)), and strength loss of sufficient size (equation (13.9f)) to achieve seismic velocities. Materials with low pressure dependence have low dilatancy and will tend to have small strength losses associated with faulting. Weakly pressure-dependent materials such as shale and serpentinite will therefore tend to not meet the conditions of high displacement rate of strength loss (equation (13.8b)) and sufficiently large strength loss (equation (13.9f)) and tend to aseismic slip more so than strongly dilatant rocks.

Rock Friction

Laboratory fault surfaces are rock that is machined flat and roughened with grinding compound. The applied stresses are supported by a small number of contacts and the fault is dilatant with pore volume fixed by the character of the small-scale roughness (fig. 13.15). Force applied normal to the plane F_n is concentrated at the asperity contacts. Assuming that resistance to shear comes from the sliding strength of asperity contacts, the shear resistance from equation (13.3) is

$$\tau \approx \frac{A_f \tau_f}{A} \tag{13.10a}$$

Further assuming that the contact shear resistance is a material constant, the pressure dependence of strength is

$$\frac{d\tau}{d\sigma_e} \approx \frac{\tau_f}{A}\frac{dA_f}{d\sigma_e} \tag{13.10b}$$

If the pressure dependence is constant and there is low cohesion, as is often observed in laboratory tests for dry weak materials [e.g., *Scruggs and*

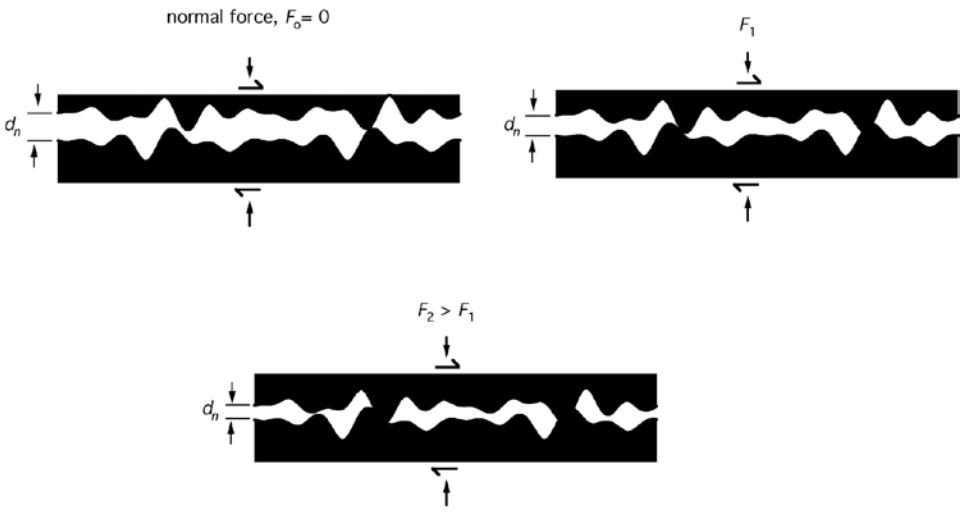

Figure 13.15 Schematic diagram of two rough surfaces in contact as normal stress is increased, clockwise from top left. Direct observations of rough surfaces in contact show that most of the surface area is not in contact, that applied normal forces F_n are concentrated at few asperity contacts across the discontinuity, and the fault contains open pore space [e.g., *Dieterich and Kilgore*, 1994]. As the normal force is increased, the asperity contact area increases through elastic or inelastic processes, and the dilatant volume is reduced.

Tullis, 1998] (fig. 13.16), then sliding friction adheres to Amonton's law (equation (13.1b)).

For constant pressure dependence, $dA_f/d\sigma_e$ in equation (13.10b) must be constant such that contact area increases in proportion to the applied normal stress. An additional requirement of constant pressure dependence follows from the relationship between contact area and macroscopic normal stress, $A_f = A\sigma_e/\sigma_f$, which produces constant $dA_f/d\sigma_e$ only when the asperity contact normal stress σ_f is constant. Thus the observation of approximately constant pressure dependence and the assumption of constant contact shear resistance requires that the contact normal stress be independent of the macroscopic normal stress ($d\sigma_f/d\sigma_e = 0$).

This section describes laboratory observations of sliding friction in the context of classic and rock-specific (rate and state) theories of friction, paying particular attention to physical processes thought to be underlie the observations, emphasizing the contrasts between weak and strong materials, and considering the implications of these contrasts for seismicity. An objective of theories of sliding friction is to explain the linear pressure dependence that is observed for virtually all materials [*Bowden and Tabor*, 1950; *Greenwood and Williamson*, 1966] including dry rock [*Dieterich and Kilgore*, 1996]. As friction theories assume nominally flat surfaces that are rough only at small scales

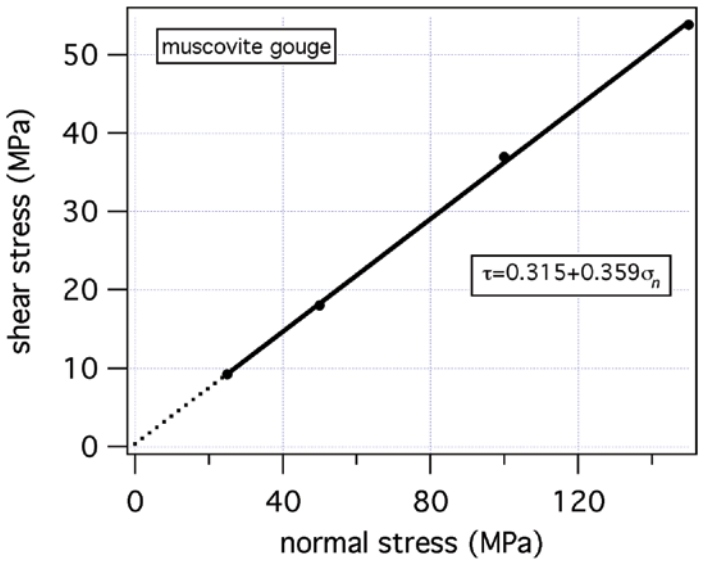

Figure 13.16 Linear pressure dependence of weak fault zone, a 1-mm layer of muscovite gouge. Friction is constant over the normal stress range, and cohesion (0.32 MPa) is low as expected for fault gouge at room temperature [*Scruggs and Tullis*, 1998].

[e.g., *Bowden and Tabor*, 1950; *Greenwood and Williamson*, 1966], these theories can be used to interpret laboratory rock friction results.

Friction Due to Inelastic Asperity Contact

One easy way to have the asperity contact normal stress be independent of the applied macroscopic normal stress is to assume that contact stress is limited by a material property. Classic friction theory [*Bowden and Tabor*, 1950] assumes that the stress at the asperity contacts is limited by the material yielding strength $\sigma_f = \sigma_y$, usually equated with the indentation hardness. At yield the average contact area is $\bar{A}_f = F_n/n\sigma_y$, where n is the number of contacts. If the normal stress $\sigma_e = F_n/A$ is increased, the contact area $\bar{A}_f = A\sigma_e/\sigma_y$ increases in proportion owing to the fixed yielding strength. If shear load F_s is applied to the surface sufficient to cause shear displacement, the contact shear yield strength is $\tau_f = F_s/n\bar{A}_f$. The shear stress is $\tau = F_s/A$. Thus the shear $\tau = \tau_f \bar{A}_f/A$ and normal stresses can be written without specific reference to the forces. So long as τ_f and σ_y are material constants, the ratio of shear stress to normal stress is a constant

$$\mu = \frac{\tau}{\sigma_e} = \frac{\tau_f}{\sigma_y} \tag{13.11a}$$

the coefficient of friction [*Bowden and Tabor*, 1950]. This theory of friction was developed to explain friction of metals that deform at highly stressed contacts by dislocation creep. This particular yielding mechanism is not possible for most silicates at room temperature, but there is considerable evidence that yielding is possible at room temperature for common minerals [e.g., *Scholz and Engelder*, 1976; *Dieterich and Kilgore*, 1994] (see Second-Order Effects section below).

Friction Due to Elastic Asperity Contacts

For rough surfaces, increasing normal stress produces larger area at individual contacts and an increasing number of contacts as the rough surfaces are brought closer together. An increase in the number of contacts tends to reduce the average contacting area somewhat. Experimental determination of the normal stress dependence of average contact dimension and contact stress of rough surfaces in contact [*Dieterich and Kilgore*, 1996] suggest that for some materials the increase in area of individual contacts is nearly exactly counterbalanced by an increase in the number of contacts such that the average contact dimension is essentially independent of normal stress (J. Dieterich, personal communication 2003). At the same time, the average contact stress remains nearly constant and the total contact area increases linearly with normal stress. While this result is not inconsistent with yielding at asperity contacts, it suggests that the observed friction is determined to a large degree by the statistics of the surface roughness. If the surface roughness is key, then linear pressure dependence can arise even if the contact-scale interactions are elastic rather than inelastic [*Greenwood and Williamson*, 1966]. The distribution of asperity heights on man-made and some natural surfaces is such that increments of increased normal stress bring the appropriate number of new asperities into contact to maintain constant average contact stress [*Greenwood and Williamson*, 1966; *Walsh and Grosenbaugh*, 1979; *Brown and Scholz*, 1985]. *Greenwood and Williamson* [1966] showed that for surfaces with roughness of laboratory test surfaces, with asperities assumed elastic, the total area of asperity contact increases essentially linearly over 4 orders of magnitude of increased load. Though they assume a nonlinear elastic contact compliance, the resulting linear pressure dependence is entirely independent of the assumed contact-scale elastic interaction. Instead, the pressure dependence of contact area is determined by the statistics of the surface topography. In this case the contact normal stress σ_f is constant but not a material constant and the friction coefficient

$$\mu = \frac{\tau}{\sigma_e} = \frac{\tau_f}{\sigma_f} \tag{13.11b}$$

is constant.

Laboratory rock friction appears to have both elastic [e.g., *Scholz*, 1988] and inelastic [*Dieterich*, 1972] components. This is discussed in more detail in the Relative Roles of Elastic and Inelastic Processes section below. The important point is that the pressure-dependent behavior of dry sliding strength is due to dilatancy. As in equation (13.10a), the pressure dependent reflects changing of contacting area with normal stress that accompanies changes in dilatant volume. In this regard, slip of preexisting faults and failure of intact rock is similar. The cause of intrinsic weakness of preexisting faults is also the same as for intact rock; materials with weak pressure dependence are weakly dilatant and strongly anisotropic, with a preferred orientation in the shearing direction [e.g., *Morrow et al*., 2000, *Moore and Lockner*, 2004]. The weakest materials, talc, graphite, wet smectite, and chrysotile serpentinite, slide between cleavage surfaces that produce little rigid dilatancy and minimal tensile fracturing. Thus, in general for preexisting faults, dry pressure dependence directly reflects the dilatancy associated with shear.

Second-Order Effects

Time Dependence While simple inelastic theories of friction imply instantaneous deformation at asperity contacts, real materials instead show time-dependent yielding. In static contact, time-dependent yielding results in both increasing contact area and fault normal closure. Figure 13.17 shows changes in asperity contact area with time of static contact in transparent samples [*Dieterich and Kilgore*, 1994]. Contact area increases approximately linearly with the log of contact time. Similarly, in laboratory slide-hold-slide tests [*Dieterich*, 1972; *Johnson*, 1981] (fig. 13.18a) fault normal convergence occurs at constant normal stress when sliding velocity is approximately zero [*Beeler and Tullis*, 1997]. In hold tests the fault surface slides initially at a steady-state velocity and then the loading velocity is set to zero and held for some duration, the hold time t_h. During the hold the fault surfaces are held in a condition approaching stationary contact, and there is measurable closure of the fault surfaces (fig. 13.18c), consistent with creep normal to the fault surface at asperity contacts, increase of contact area, and reduction of the dilatant volume of the fault. The closure is linear or nearly linear in log time, consistent with the area change results. This fault normal closure is also associated with an increase in frictional resistance (fig. 13.18b) [*Dieterich*, 1972; *Nakatani and Mozichi*, 1995, *Karner and Marone*, 1998], which has been previously observed for other materials [*Dokos*, 1946; *Rabinowicz*, 1958]. The increase in resistance is measured somewhat indirectly. Following the period of approximately stationary contact, the loading velocity is returned to its original value resulting in progressive increase in shear stress. The shear stress increases, reaches a peak τ_{peak}, and subsequently returns to its previous steady-state value. The amount of strengthening that occurs during the hold period is given by the difference between τ_{peak} and the steady-state strength. *Dieterich* [1972] found $\mu_{peak} = \tau_{peak}\sigma_e$ to increase linearly with log of

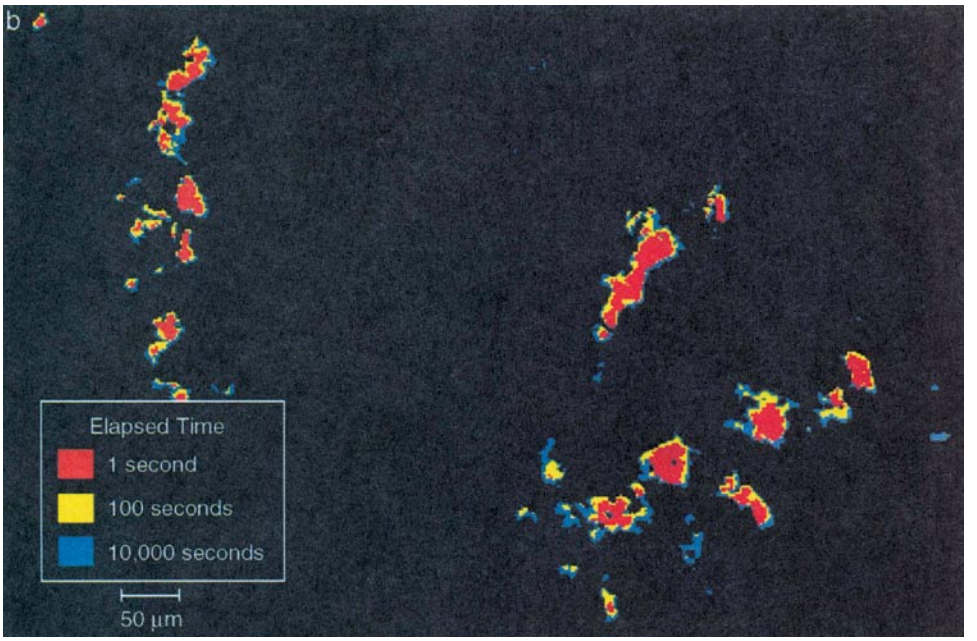

Figure 13.17 Three superimposed transmitted light photomicrographs of asperity contact area on an analogue laboratory fault surface. Reprinted from Pure and Applied Geophysics, 143, *Dieterich and Kilgore*, Direct observation of frictional contacts: New insights for state-dependent properties, 283–302, Copyright (1994), Birkhäuser Verlag, Switzerland. The pictures were taken at 1, 100, and 10,000 s contact time and the contacting areas are colored to illustrate the time-dependent growth of contact area by yielding.

hold time $b \ln t_h$, but it is a second-order effect, for example a strengthening coefficient for granite of 0.01 relative to the frictional strength of 0.7.

Shear-Induced Weakening, Shear-Induced Dilatancy and Age Dependence On the basis of the hold and static contact tests, it is tempting to represent contact normal strength as time dependent, but that is incomplete. While there may be time-dependent effects ongoing during sliding at appreciable rates, friction at constant sliding rates is not an explicit function of time. Whatever yielding process occurs during approximately static contact is modulated by other effects at appreciable slip rates.

Because asperity contacts are very small, they have limited time of contact while the fault is sliding at a significant rate. Therefore any time-dependent creep process operating at an asperity has a limited duration, and there will be ongoing reduction in the contact area due to shearing. After slip equivalent to the contact dimension, the asperity will no longer be in contact. So during slip, there are two competing processes, time, which tends to increase contact area, and slip, which tends to replace yielding contacts and bring undeformed asperi-

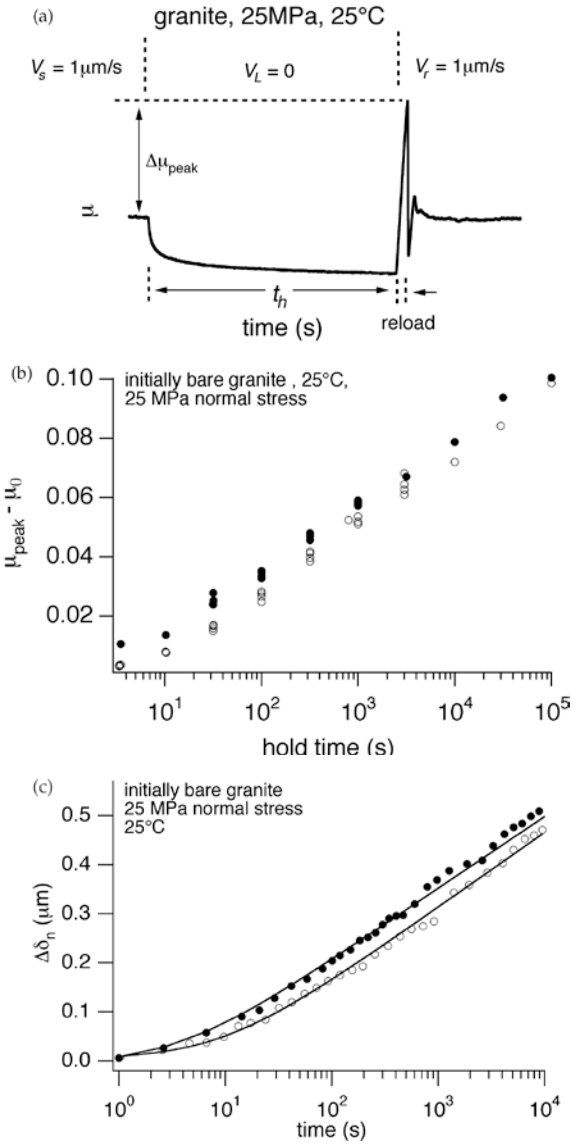

Figure 13.18 Slide-hold-tests. (a) Slide-hold-slide test procedure in friction versus time. The sample slides initially at a steady-state starting/reload velocity $V^{s/r}$. At some time the loading velocity is set to zero, and the measured strength as the fault creeps a bit due to the nonzero shear stress, relaxing the elastic distortion of the testing machine. After some length of time the sample is reloaded by resetting the load point velocity to $V^{s/r}$. Strength increases, reaches a peak μ_{peak} and subsequently returns to its previous steady-state value. (b) The amount of strengthening ($\mu_{peak} - \mu_0$) from slide-hold-slide tests on initially bare Westerly granite, as a function of hold time [after *Dieterich*, 1972]. (c) Time dependence of fault thickness measured during the hold portion of a slide-hold-slide test for initially bare Westerly granite. Solid lines are fits to the data using an empirical equation $\delta_n = \delta_{n0} + \alpha \ln(t + c_3)$, where δ_{n0} is δ_n at the start of the hold and α and c_3 are constants.

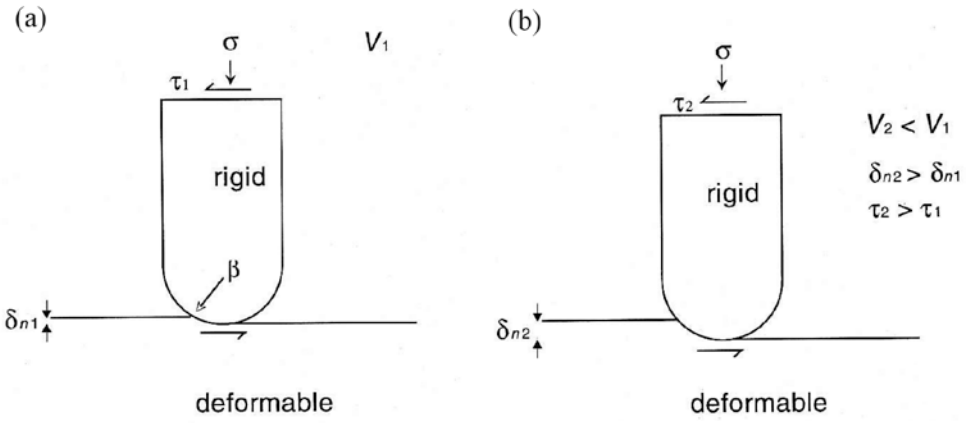

Figure 13.19 Schematic of rigid asperity model. Here, β is the radius of the spherical asperity tip. (a) High sliding velocity, with asperity riding high. (b) Low sliding velocity, with asperity sinking deeper [after *Scholz and Engelder*, 1976].

ties into contact. This concept of competition between slip and time can be represented by the average age θ of the asperity contacts. For constant slip rate V, average age takes the value $\theta = d_c/2V$, where d_c is a representative dimension of asperity contacts on the fault surface; conversely, during static contact $d\theta = dt$.

Interactions between time-dependent and displacement-dependent effects have implications for volume change that can be considered using an asperity model consistent with the experiments of *Engelder and Scholz* [1976] (fig. 13.19). Consider a rigid asperity at constant normal force, indenting a deformable material. Assume that the rheology of the deformable material in the absence of slip requires contact area to increase with time, consistent with the hold data (fig. 13.18) and the size variation of indentations in quartz with time [*Scholz and Engelder*, 1976] (see fig. 13.26). At steady-state sliding velocity the depth of penetration of the asperity δ_n decreases with sliding velocity, owing to the asperity shape and the reduced residence time for penetration at higher velocity. Therefore, at high sliding velocity the contact area and the contact's resistance to slip (fig. 13.19a) are small. When the velocity is decreased, there will be a transition from one steady-state depth to another (i.e., the change from that of figs. 13.19a to 13.19b), over a distance related to the asperity dimension. Fault normal strain (as measured by δ_n), contact area A, and shear resistance will vary similarly with displacement as the sliding velocity is varied.

For this model, at steady-state prior to an imposed step change in velocity, there is no net dilation or compaction. However, there is a dynamic balance between ongoing time-dependent compaction and ongoing shear-induced dilatancy. Using the appropriate requirement at steady-state $d\varepsilon_n = 0$, the balance can be written as

$$\left[\left(\frac{\partial \delta_n}{\partial \delta_s}\right)_t\right]_{ss} = -\frac{1}{V}\left[\left(\frac{\partial \delta_n}{\partial t}\right)_{\delta_s}\right]_{ss} \tag{13.12}$$

If the velocity is increased, the fault will dilate. The amount of time-dependent interpenetration of the substrate by the asperity depends on the residence time of the asperity over a particular spot, and the residence time depends on the sliding velocity; thus fault-zone thickness is inherently velocity dependent. That time-dependent yielding is modulated by slip-induced dilatancy during sliding is evident in experiments where fault normal motion is monitored during changes in sliding velocity (rate stepping tests) [*Morrow and Byerlee*, 1989; *Marone et al.*, 1990; *Wang and Scholz*, 1994]. Changes in sliding velocity produce an immediate displacement-dependent change in fault normal closure (fig. 13.20).

These observations have been incorporated into rock friction theory by allowing the asperity contact strength to be an explicit function of age [e.g., *Dieterich*, 1979]. Using the Amonton form equation (13.11), the normal strength is

$$\sigma_f = \sigma_o + f(\theta) \tag{13.13a}$$

where σ_0 is a reference value of contact stress and f is some function of age that produces the log time-dependent effect seen in the area, closure, and strength data during static contact and the implied changes in contact area with slip (figs. 13.18 and 13.20).

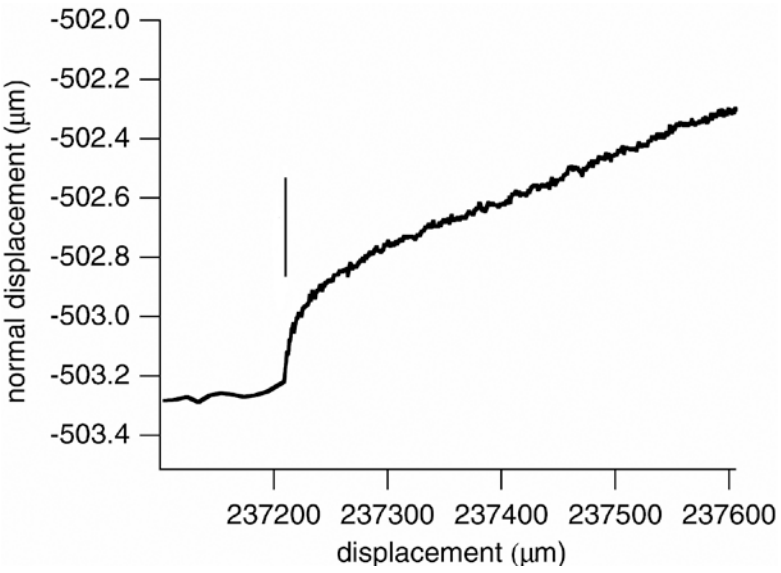

Figure 13.20 Response of fault thickness to changes in sliding rate for a 1-mm-thick granite gouge layer at 25 MPa normal stress and room temperature. An increase in sliding from 1 to 10 μm/s is imposed at displacement marked by the vertical line. The fault zone dilates in response to the change of deformation rate [after *Morrow and Byerlee*, 1989; *Marone et al.*, 1990].

Rate Dependence Sets of slide-hold-slide tests at different loading/reloading rates [*Kato et al.*, 1992; *Marone*, 1998] show more apparent restrengthening during the hold at higher loading velocity (fig. 13.21). This suggests that fault strength depends on slip rate or loading rate in addition to age. A slip-rate effect is also seen in rate stepping tests where slip velocity is changed. An increase in sliding velocity produces the age-dependent effect discussed in the previous section: a displacement-dependent reduction in fault strength and dilation. Superimposed on this is an immediate change in fault strength of the opposite sense (fig. 13.22). Thus, in both hold and rate stepping tests, there is a positive rate-dependent effect. This viscous effect has been incorporated into friction theory by allowing the shear strength of asperity contacts to depend on sliding rate [*Dieterich*, 1979]

$$\tau_f = \tau_o + g(V) \tag{13.13b}$$

The observations show that the rate dependence has the same logarithmic form as seen in rock fracture tests (equation (13.5a)) and that the effect is second order (for example, a rate-dependent coefficient a for granite of 0.008 relative to the frictional strength of 0.7).

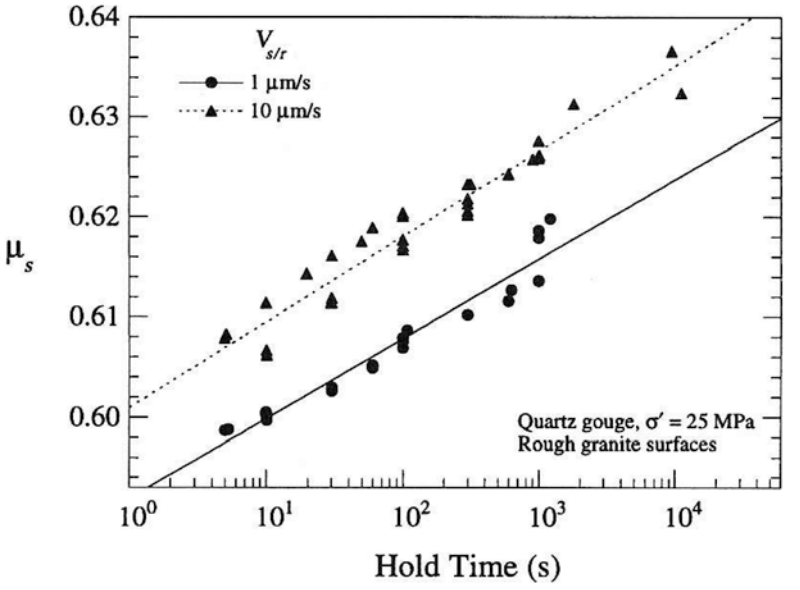

Figure 13.21 Direct measure of the instantaneous rate dependence of rock friction [*Marone*, 1998]. Reprinted, with permission, from the Annual Review of Earth and Planetary Sciences, Volume 26 (c) 1998 by Annual Reviews, www.annualreviews.org. Peak strengths from slide-hold-slide tests conducted at different load/reloading rates. The peak strengths depend systematically on the sliding rate.

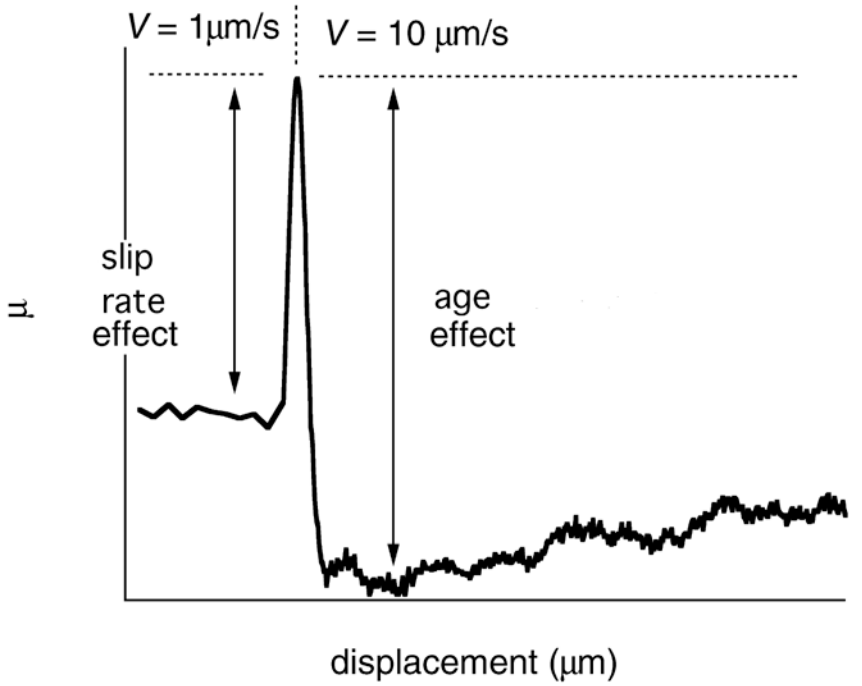

Figure 13.22 Fault strength for granite at 25 MPa normal stress and room temperature in response to an imposed change in sliding velocity. The loading velocity is increased by an order of magnitude at displacement corresponding to the vertical dashed line. The net rate dependence $d\mu_{ss}/d\ln V$ is the sum of two opposing effects, the instantaneous rate effect and an age dependence that is reset by constant slip rate.

Constitutive Relations for Friction

The second-order dependencies of fault strength on age and slip rate (equations (13.13a) and (13.13b)) can be combined with equation (13.10) into a friction relation

$$\mu = \frac{\tau_f}{\sigma_f} = \frac{\left[\tau_o + g(V)\right]\left[\sigma_o - f(\theta)\right]}{\left[\sigma_o + f(\theta)\right]\left[\sigma_o - f(\theta)\right]} \tag{13.13c}$$

Discarding the product of second-order terms leads to the form of friction relation developed by *Dieterich* [1979], which is the basis of *Ruina* [1983] and *Rice and Ruina's* [1983] rate and state friction equations:

$$\mu = \frac{\tau_o}{\sigma_o} + \frac{g(V)}{\sigma_o} - \frac{\tau_o f(\theta)}{\sigma_o^{\,2}} \tag{13.13d}$$

On the right side of equation (13.13d), the first term is first order, the second term is the second-order positive direct dependence of contact shear resistance on sliding velocity, and the third term is the second-order negative dependence of contact normal strength on contact age. Experimental observations constrain the rate and age dependencies: $g(V) = \mathbf{A}\ln(V/V_0)$ (fig. 13.22) and $g(\theta) = \beta\ln(\theta/\theta_0)$ (fig. 13.18). Expressing the first-order term as $\tau_0/\sigma_0 = \mu_0$ gives

$$\mu = \mu_o + \frac{\mathbf{A}\ln(V/V_0)}{\sigma_o} - \frac{\mu_o\beta\ln(\theta/\theta_0)}{\sigma_o} \tag{13.14}$$

Some implications of equation (13.14) are discussed subsequently in the Some Physical Implications section below. Equation (13.14) can be expressed using more conventional notation as

$$\mu = \mu_o + a\ln(V/V_0) + b\ln(V_0\,\theta/d_c) \tag{13.15a}$$

where the standard coefficients are $a = A/\sigma_0$ and $b = -\mu_0\beta/\sigma_0$ and $\theta_0 = d_c/V_0$. An expression for the slip and time dependencies that underlie dependence of friction on age is derived from a partial derivative expansion of $\theta = h(\delta, t)$ and the requirements that age increases linearly with time in the absence of slip (fig. 13.18) and decreases exponentially with slip, $\left(\frac{\partial\theta}{\partial t}\right)_\delta = 1$ and $\left(\frac{\partial\theta}{\partial d}\right)_t = -\frac{\theta}{d_c}$, respectively. This leads to [*Ruina*, 1983; *Linker and Dieterich*, 1992]

$$\frac{d\theta}{dt} = 1 - \frac{\theta V}{d_c} \tag{13.15b}$$

The steady-state value of age is $\theta_{ss} = dc/V$ and the steady-state value of friction is $\mu_{ss} = \mu_0 + (a\text{-}b)\ln(V/V_0)$.

Simulations of Aseismic Laboratory Observations

Equations (13.15) reproduce the observations of time, slip, and rate dependence seen in aseismic laboratory hold and rate stepping tests and simulations with equations (13.15) illustrate how constitutive parameters *a* and *b* can be inferred from experimental measurements. The log time dependence of the peak stress in hold tests is reproduced and the change in peak stress with log of hold time is the constitutive parameter *b* (fig. 13.23a). In hold tests conducted at different loading reloading rates, the difference in hold peak strengths from the different loading reloading rates is $a\ln(V_2/V_1)$. The spac-

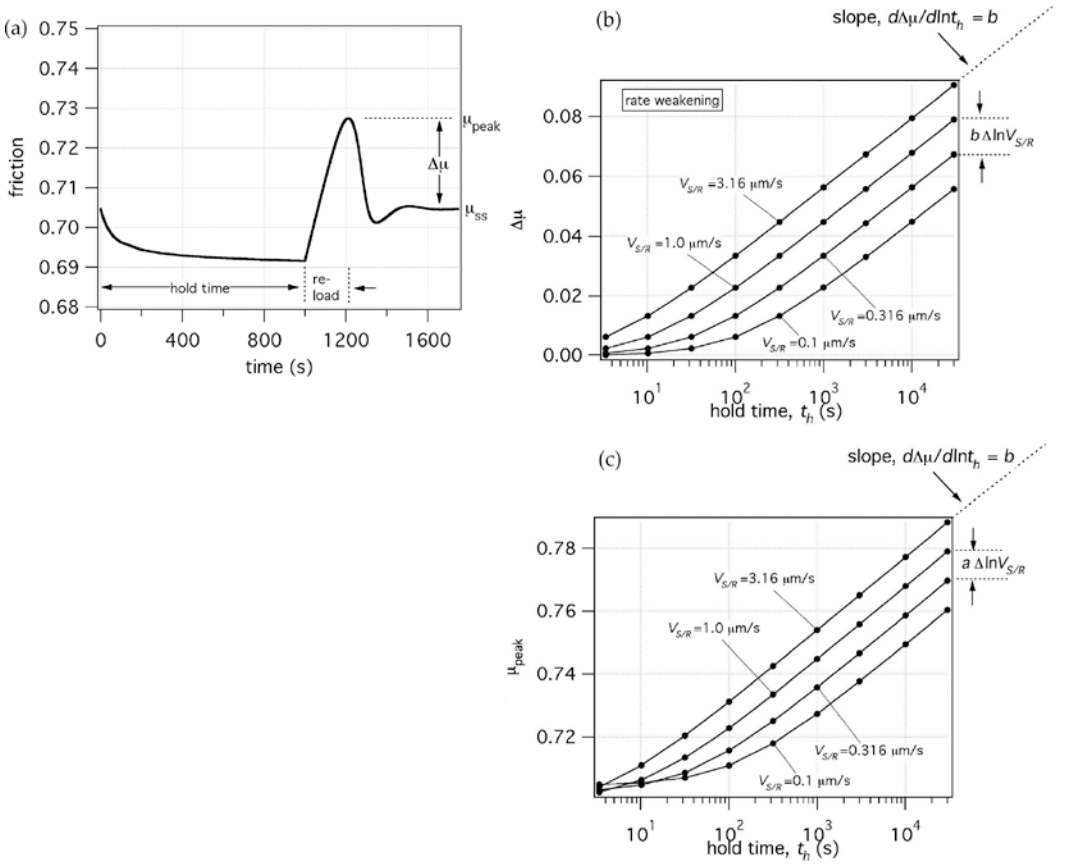

Figure 13.23 Numerical simulations of slide-hold-slide tests with rate and state constitutive equations (13.15). For all simulations the starting and reloading velocities are equal, $a = 0.008$, $b = 0.010$, $d_c = 5$ μm, $\mu_0 = 0.7$, and $V_0 = 0.1$ μm/s. The machine stiffness normalized by normal stress k/σ_n =0.0021 1/μm. This is a compliant testing machine; however, the individual constitutive parameters a and b are directly measured in the simulated tests. (a) Simulation of a single 1000-s slide-hold-slide test. (b) Slide-hold-slide delta friction versus log hold time for 36 different hold time and loading/reloading velocities. Test at the same starting/reloading velocity are connected by lines. The spacing between the sets and the slope of the lines reflect the rate of aging. (c) Peak strength versus log hold time for 36 different hold time and loading/reloading velocities. Tests at the same starting/reloading velocity are connected as in figure 13.23b. The spacing between the sets reflects the instantaneous rate dependence, and the slope reflects the rate of aging.

ing between the changes in friction between the peak and steady-state $\Delta\mu$ for the different sliding velocities is $b\ln V_2/V_1$ for rate-weakening faults (fig. 13.23b); for rate-strengthening faults the spacing is $(2a\text{-}b)\ln V_2/V_1$. Rate stepping test simulations produce the typical response of a direct rate dependence

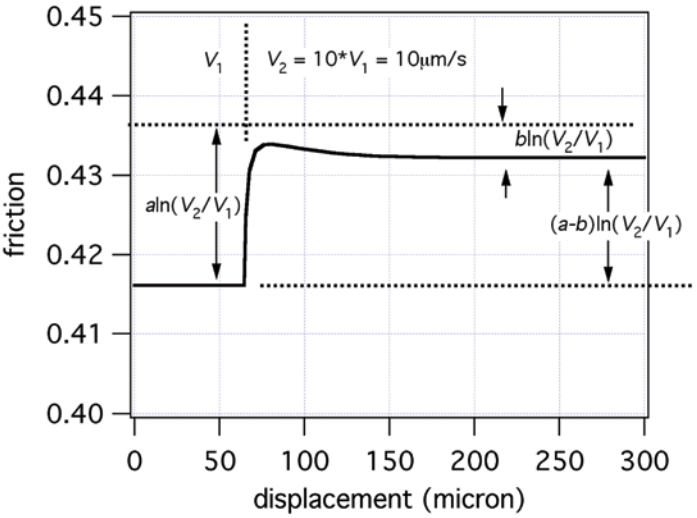

Figure 13.24 Numerical simulation of a rate step test with rate and state constitutive relation (13.15), $a = 0.008$, $b = 0.001$, $d_c = 20$ μm, and $\mu_0 = 0.4$. The machine stiffness normalized by normal stress is $k/\sigma_n = 0.0021$ 1/μm. The steady-state rate dependence $d\mu/d\ln V = (a\text{-}b)$ is measured directly in this test; however, owing to the finite compliance of the system, the individual parameters a and b are not directly apparent from the simulation. This indicates that, unlike for hold tests (fig. 13.23), the individual parameters a and b cannot be directly inferred from rate stepping tests and must be retrieved from data using an indirect procedure such as numerical inversion.

followed by the slip-dependent change of age. The net change of friction is $(a\text{-}b)\ln V_2/V_1$ (fig. 13.24).

Stick-Slip and the Condition for Frictional Instability

Seismic slip rather than aseismic sliding is also observed in some laboratory experiments (fig. 13.25). Stick-slip is periodic or quasi-periodic seismic stress drop resulting from constant loading. Simulations using equations (13.15) produce stick-slip at the appropriate loading conditions. Stick-slip simulations with equation (13.15) and direct observations show that the steady-state rate dependence controls aspects of the cycle duration and amplitude [*Gu and Wong*, 1991; *Wong and Zhao*, 1990] Peak strength goes as $d\mu_{peak}/d\ln V_L = (b\text{-}a)$ [*Gu and Wong*, 1991]. The amplitude of the static stress drop also varies with loading rate V_L approximately as $d\mu_{static}/d\ln V_L \approx (b\text{-}a)(1 + \zeta)$, where ζ is the fractional overshoot. If earthquakes correspond to slip on preexisting fault surfaces, as opposed to failure of intact rock, then the conditions leading to

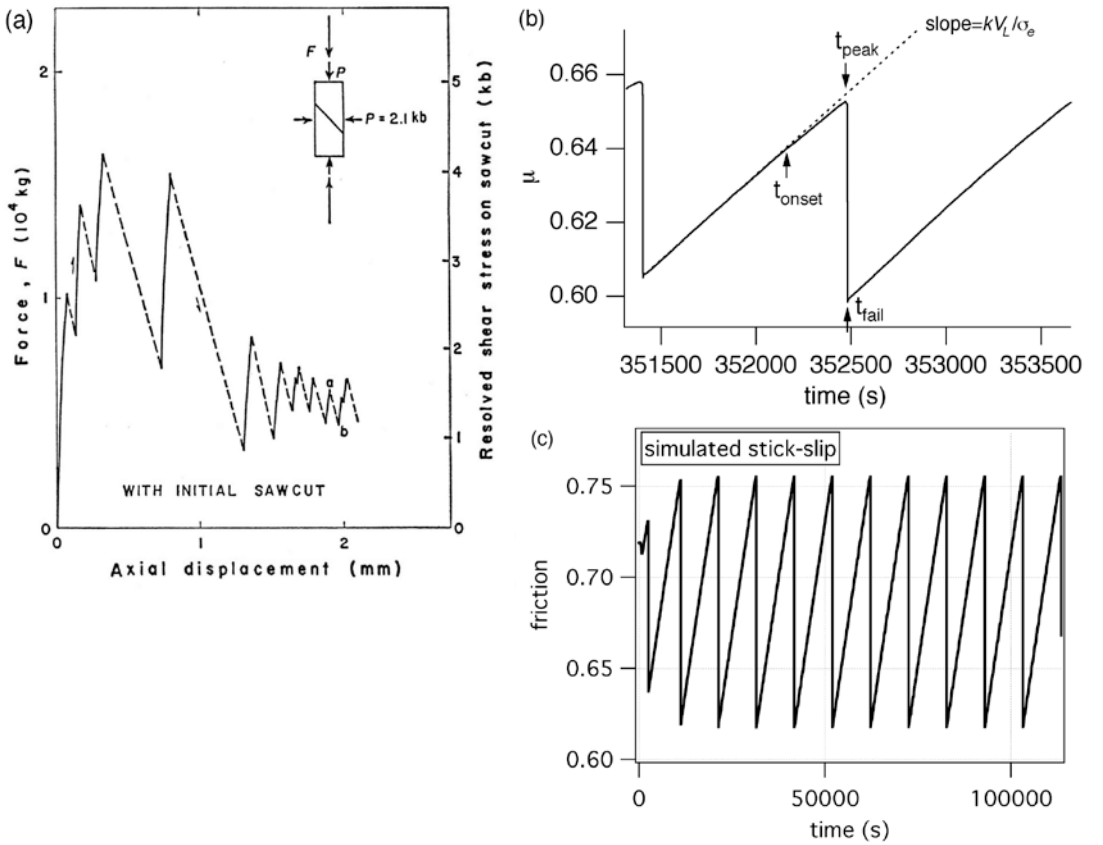

Figure 13.25 Stick-slip sliding. (a) Original stick-slip sliding on sawcut granite fault at 210 MPa confining pressure and room temperature. Reprinted with permission from Science, 153, *Brace and Byerlee*, Stick-slip as a mechanism for earthquakes, 990–992, Copyright [1966] AAAS. (b) A laboratory experiment on a granite sawcut at 50 MPa confining pressure showing evidence of precursory slip; the loading deviates from the linear elastic load indicating on-going slip prior to peak strength. (c) Simulation of laboratory stick-slip using rate and state variable equation (13.15), $a = 0.008$, $b = 0.012$, $d_c = 0.8$ μm, $V_0 = 1$ μm/s, and $\mu_0 = 0.7$. The machine stiffness normalized by normal stress is $k/\sigma_n = 0.00137$ 1/μm. This is dynamic slip of single degree of freedom slider block and simulates the effects of radiated energy using the radiation damping procedure of *Rice* [1993]. Normal stress is 21.2 MPa, shear wave velocity is 3000 m/s, and the shear modulus is 30 GPa. The calculation is started from steady-state sliding at 0.009 μm/s. The system is perturbed by increasing the loading rate to 0.01 μm/s, inducing the unstable slip.

stick-slip faulting in friction experiments are relevant to studies of earthquake nucleation. Thus stick-slip sliding is considered to be the laboratory equivalent of repeating earthquake cycles [*Brace and Byerlee*, 1966], and the onset of slip instability is analogous to earthquake nucleation.

If the elastic stiffness of the loading system is expressed as $d = d\tau/d\delta$, where δ is fault slip, then the requirement for slip instability at constant normal stress can be expressed in terms of a critical stiffness [*Dieterich*, 1979]

$$k_c = -\frac{d\mu}{d\delta}\sigma_e \tag{13.16a}$$

where $d\mu$ is the drop in friction. A slip instability can occur for $k < k_c$. This relation has been verified experimentally for faults with artificial but well-characterized displacement weakening [*Lockner and Byerlee*, 1990]. However, for the constitutive equation (13.15) in addition to the intrinsic displacement dependence of strength, there are time and rate dependencies that must be considered. Instead of $d\mu/d\delta$, for equation (13.15) the sign of the steady-state rate dependence $d\mu_{ss}/d\ln V$ is key in determining whether faulting is potentially seismic. When the dependence of steady-state frictional strength on the logarithm of sliding velocity is negative ($d\mu_{ss}/d\ln V < 0$), any perturbation that causes the fault to accelerate will lead to a loss of strength and will encourage further slip acceleration [*Rice and Ruina*, 1983]. In this case, slip instability is possible. Conversely, for neutral or positive rate dependence ($d\mu_{ss}/d\ln V \geq 0$), increasing slip rate produces no strength decrease so sliding will be stable. Linearized perturbation analysis of equation (13.15) [*Rice and Ruina*, 1983; *Ruina*, 1983] results in an expression for critical stiffness analogous to equation (13.16a)

$$k_c = -\frac{d\tau_{ss}}{d\ln V}\frac{1}{d_c} = \frac{(b-a)\sigma_e}{d_c} \tag{13.16b}$$

where τ_{ss} is the steady-state frictional resistance and d_c is the characteristic displacement of the age-dependent term. Accordingly, instability is favored by more negative values of $d\tau_{ss}/d\ln V$ and by low values of k [*Rice and Ruina*, 1983; *Gu et al.*, 1984].

Laboratory measurements of (*a-b*) have been conducted using initially bare rock surfaces (ground, flat, parallel rock roughened with abrasive) and simulated gouge layers (powdered rock flour sheared between rigid blocks). Thick quartzofeldspathic gouge layers have positive rate dependence unless shear displacement becomes localized within the layer [*Dieterich*, 1981; *Marone et al.*, 1990; *Marone and Kilgore*, 1993] (also see review of *Marone* [1998]). While gouge layers show variability in the sign of (*a-b*), initially bare rock surfaces of quartzofeldspathic rock [*Dieterich*, 1978b; *Tullis and Weeks*, 1986] are rate weakening ($b\text{-}a > 0$). Slip between bare rock surfaces remains localized even at large displacement and such faults show little tendency for fault-zone width growth after an initial period of rapid wear [*Biegel et al.*, 1989] because they are flat at long wavelengths (see *Power et al.* [1988] and as discussed below).

In contrast to experiments, a continually expanding fault zone is expected for natural faults [*Robertson*, 1983]. Increased thickness of natural fault zones may result from geometrical and dynamic effects during shear. Natural rock surfaces such as fracture and joint surfaces have a fractal roughness [*Brown and Scholz*, 1985], As a result, increasing displacement of an initially matched shear fracture (protofault) leads to an increasing volume of mismatched surface irregularity and therefore increasing wear material (gouge) with displacement [*Power et al.*, 1988]. During earthquake slip, large dynamic stresses that develop in front of an advancing shear rupture during propagation may be higher on off-fault planes than on the fault plane itself [*Rice*, 1980]. These high stresses may induce branching or off-fault deformation that may lead to nonplanar ruptures, fault surface roughening and gradual growth of the damage zone with successive earthquakes. Thus natural large displacement fault zones are wide, for example, the San Andreas fault zone, with total offset of hundreds of kilometers, has a thickness of as much as a kilometer in places [*Sibson*, 2002]. The experimental observations thus require that slip during earthquake nucleation is localized so that $d\mu_{ss}/d\ln V < 0$, even within very wide fault zones. At least in experiments to date, fault slip in simulated gouge layers at the largest displacements measured does not localize to the degree that the rate dependence is negative [*Beeler et al.*, 1996], though localization does occur and persist at short displacements in some experimental geometries [*Marone*, 1998]. It is not known exactly how such localization arises in experiments or in mature natural fault zones. The remainder of this paper focuses on the physical implications of slip between initially bare rock surfaces where shear is localized and which are better understood and less complicated than measurements made on simulated gouge.

Some Physical Implications

Constraints on Contact-Scale Mechanism, Mostly for Strong Materials

Laboratory measurements have not determined the physical processes responsible for the rate or time-dependent mechanisms. A significant limitation to equation (13.15) in its application to earthquake phenomenon is this uncertain physical basis. So long as rate and state effects are not attributed to thermally activated deformation mechanisms, it will remain difficult to extrapolate the observations in pressure and temperature to conditions other than those of the particular experiments, to establish the dependence of the effects on environmental factors such as the presence or absence of fluids and fluid chemistry, and to determine how the specific rate-dependent effects compare with others that might compete at significant depth in the Earth. However, some inferences about the mechanisms underlying rock friction can be made from existing laboratory data. For instance, the logarithmic dependencies of

friction on slip rate and on contact time are consistent with low temperature deformation studies and chemical reaction rates, as follows. At modest temperatures and pressures, deformation mechanisms at highly stressed asperity contacts such as subcritical crack growth [*Atkinson*, 1984] and dislocation glide [*Evans*, 1984] have deformation rates that depend logarithmically on pressure or stress, e.g.,

$$v = v_* \exp(-E/RT) \tag{13.17a}$$

where the activation energy $E = E_* - \sigma_c \Omega$ is the difference between a nominal value and the product of stress at the crack tip σ_c and the activation volume Ω [e.g., *Rice et al.*, 2001, *Nakatani*, 2001]. Equation (13.17a) is the Arrhenius equation that is characteristic of processes controlled by the rate of chemical reaction.

Rate Dependence If the expression (13.17a) is solved for stress as a function of rate, stress is

$$\sigma_c = \frac{E_*}{\Omega} + \frac{RT}{\Omega} \ln \frac{v}{v_*} \tag{13.17b}$$

That equation (13.17a) underlies second-order dependencies of friction and rock failure on time and on slip rate is a common argument in the rock mechanics literature. As previously discussed in the paper, many studies since *Scholz* [1968c] have related the rate dependence of rock fracture strength (equation (13.3a)) to the rate dependence of single tensile crack growth rate in double-cantilever experiments on glass [*Lawn*, 1993] and single mineral crystals [*Atkinson*, 1984]. More recently, it was found that both friction and intact failure tests yield values of the *a* coefficient in the range 0.003–0.009 for granite at low temperature [*Lockner*, 1998]. Similar agreement between *a* for friction and intact rock was found by *Tullis and Weeks* [1987] for carbonate rocks; they argued that a common mechanism was responsible. In the case of granite, the similarity between rock failure and rock friction rate dependence lead *Lockner* [1998] to suggest that subcritical crack growth is the mechanism underlying this effect in both friction and rock failure of granite.

Direct comparison between the rate dependence of subcritical crack growth and that of rock friction can be made using a normalization scheme that follows from one proposed by *Tullis and Weeks* [1987] for comparing results of rock friction to intact failure tests. For crack growth, rather than equation (13.5b), which is specific to water-assisted crack growth (stress corrosion), a general form is

$$v = v_* \exp\left(\frac{-E_* + \varsigma K_i}{RT}\right) \tag{13.17c}$$

where ζ is an empirical constant and E_* is an activation energy [*Wiederhorn and Bolz*, 1970. K_i is the stress intensity factor that relates the applied macroscopic stress σ, crack dimension c, and the specific experimental geometry

to the crack tip stress as $K_i \propto \sigma\sqrt{c}$. In crack growth experiments, K_i is independent of crack dimensions and $K_i \propto \sigma$ [*Atkinson and Meredith,* 1987b]. Expressing equation (13.17c) with crack velocity v as the independent variable leads to

$$\sigma \propto \left[\frac{E_*}{\varsigma} + \frac{RT}{\varsigma} \ln \frac{v}{v_*} \right] \tag{13.17d}$$

Normalizing this expression by the resistance σ_* resulting from slip at the reference slip rate v_* is

$$\frac{\sigma}{\sigma_*} = 1 + \frac{RT}{E_*} \ln \frac{v}{v_*} \tag{13.17e}$$

Here, the normalized rate dependent coefficient (RT/E_*) is the actual rate dependence $(RT/\zeta_{..})$ divided by the nominal stress (E_*/ζ), and can be interpreted as the rate dependence of the remotely applied stress driving crack propagation, divided by the nominal value of that stress. The unknown constant of proportionality is eliminated by the normalization.

An analogous expression for friction can be derived from the standard rate and state equation (13.15) by following the same procedure of normalizing by an absolute friction μ_0 resulting from the arbitrary slip rate V_0

$$\frac{\mu}{\mu_0} = 1 + \frac{\mathbf{A}}{\tau_0} \ln \frac{V}{V_0} + \frac{\beta}{\sigma_0} \ln \frac{\theta}{\theta_0} \tag{13.17f}$$

Note with reference to equation (13.15a), the coefficient of the rate-dependent term $(\mathbf{A}/\tau_0)$ is the actual contact shear strength coefficient normalized by the nominal contact shear strength and has the same interpretation as the coefficient in equation (13.17e). Similarly, the coefficient of the age-dependent term in equation (13.17f) (β/σ_0) is the actual coefficient normalized by the nominal contact normal strength.

To compare the rate dependence of crack growth experiments to friction data, the rate of crack propagation v must be equated with the fault slip rate V or fault-zone strain rate. The difference between the fault slip rates and crack growth rates in the raw experimental data is very large; rate stepping test velocity for friction is in the 1–10 μm/s range while crack growth rates are up to 1×10^{-2} m/s. If v is equated with V, implying that frictional slip produces crack growth at the same rate, and the reference velocity is 1.8 μm/s, then for marble the ratio $RT/E_* = 0.055$ from equation (13.17e) does not compare favorably with the analogous friction parameter $a/\mu_0 = 0.011$. With this assumption of $v = V$ a discrepancy of similar size results for quartz and granite. While this discrepancy might be due to very large differences in the rate of crack growth associated with a particular fault sliding velocity, the sense of the difference in

velocity necessary to account for the difference in normalized rate dependence is unexpected. To produce a normalized rate dependence similar to that seen in the friction experiments, the reference velocity for crack growth must greatly exceed the compressive wave speed. Obviously, frictional slip cannot produce subcritical crack growth velocity approaching the elastic wave speed.

In the following estimates of the normalized rate dependence of crack growth in geologic materials the crack growth during laboratory friction experiments is arbitrarily assumed to occur at subcritical rates of 1 m/s (v_* in equation (13.17e) is 1 m/s). This is ~1 order of magnitude higher than the largest rates in subcritical crack growth experiments. The normalized coefficient for subcritical crack growth in Westerly granite at room temperature from *Atkinson and Meredith* [1987a] is 0.021, while the analogous normalized rate-dependent coefficient from Westerly rock friction tests [e.g., *Beeler et al*., 1996] is 0.011, roughly ½ the crack growth value. The normalized rate-dependent coefficient from room temperature experiments on synthetic quartz and natural quartzite [*Atkinson and Meredith* [1987a, 1987b] is 0.033–0.035, while the coefficient from quartzite friction tests is 0.009, less than ⅓ the crack growth value. Essentially identical results are found for Carrara marble; for crack growth the room temperature normalized rate dependence is 0.032, while the normalized friction data of *Tullis and Weeks* [1987] has rate dependence of 0.011, about ⅓ the crack growth value.

The conclusion is that quartzofeldspathic rocks and marble show rate dependencies that are not consistent with crack growth rate dependencies. While there is great uncertainty in the proper reference crack velocity to use in comparisons of friction and crack growth data, the difference cannot be reconciled by adjustments in the rates chosen as the reference. A possible exception is the rock analogue, silica glass whose crack growth normalized rate dependence is 0.018 [*Lawn*, 1993]; similar normalized values were found by *Weeks et al*. [1991]; however, the quality of the friction data is poor.

On the basis of a comparison between the size of the rate-dependent coefficient at low-strain rate for faulting of serpentinite and rock failure of biotite at room temperature, *Reinen et al.* [1994] argued that dislocation glide controls the rate dependence of serpentinite at low slip rate. This argument, which ignores temperature dependence of the rate-dependent process, was discounted somewhat by *Escartin et al.* [1997], who showed that dislocation does not occur in rock failure tests at room temperature in serpentinite. Similarly, dislocation is not expected in quartzofeldspathic materials at room temperature. However, the *Reinen et al.* [1994] argument probably does apply at asperity contacts on fault surfaces of other weak phases that deform via dislocation glide at room temperature, for example biotite, muscovite, and illite (see Some Other Aspects of Rock Friction section below), and applies to strong materials known to deform via dislocation motion at room temperature such as olivine [*Evans and Goetze*, 1979].

Time-Dependent Strengthening The time-dependent increase in static friction [*Dieterich*, 1972] (fig. 13.18) is also seen in analogue materials, soda lime

glass, and lucite plastic where it has been shown to result directly from ductile flow or distributed fracturing at highly stressed asperity contacts on the fault surface [*Dieterich and Kilgore*, 1994]. Similar behavior can also be seen directly in single asperity hardness tests, where a loaded indenter of diamond or sapphire is placed in contact with material surfaces. Surfaces of quartz or olivine show a time-dependent change in indent area [*Scholz and Engelder*, 1976] (fig. 13.26), as previously shown in metals and oxides [*Westbrook and Jorgenson*, 1965], implying time-dependent increase in the shear strength of the contact. Indentation tests showing the same kind of effect have been conducted on the glass and lucite analogue materials [*Dieteich and Kilgore*, 1994]. In this case, the indentation tests were compared directly with the tests measuring time-dependent frictional strengthening in which contact area was monitored directly. There is good agreement between area changes with time in these two types of tests on analogues. Furthermore, if an Arrhenius flow law (equation (13.17a)) is used to model indentation tests, under certain circumstances the contact area increase follows the logarithmic increase seen in most hold tests and that is approximately seen indentation tests [*Berthoud et al.*, 1999]. This strongly suggests that the Arrhenius representation is also appropriate for representing time-dependent processes on friction surfaces.

However, the physical processes responsible for time-dependent yielding during hold tests or during indentation tests on analogue materials are unknown and have not been clearly related to the similarly unknown processes operating in minerals. Direct comparison between rates of time-dependent strengthening and indentation rates in minerals does not yield consistent re-

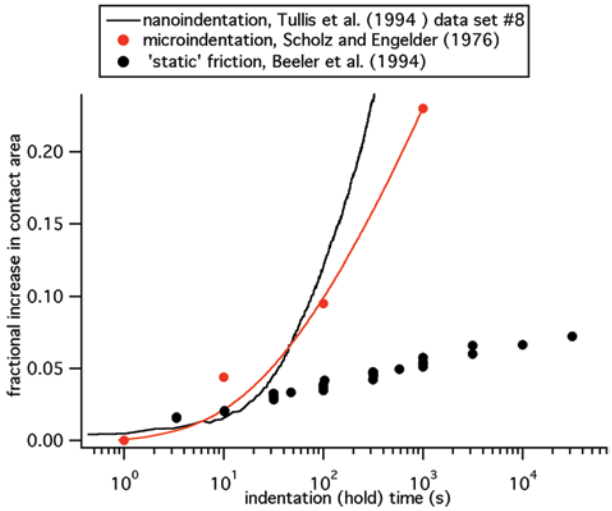

Figure 13.26 Comparison between quartz indentation data and change in quartzite friction with hold time. The data are from microindentation [*Scholz and Engelder*, 1976], nanoindentation [*Tullis et al.*, 1994], and slide-hold-slide tests. The red line is a fit to the microindentation data using an equation for static indentation based on the Arrhenuis rheology (equation (13.17a)).

sults (fig. 13.26) [*Goldsby et al.*, 2004]. The indentation rates are significantly faster, and at least for quartz, there is no known mechanism of ductile flow at these conditions [*Westbrook*, 1958; *Evans*, 1984]. It is possible that the mechanisms of contact-scale deformation are different in indentation and friction sliding tests because, even if the contact normal stress were the same in both kinds of tests, the frictional contacts support large shear stresses that are absent in the indentation tests. *Sharp et al.* [1993] estimate that the normal force necessary to induce fracture under a sliding contact is roughly one tenth that for a static contact, and they estimate that materials deforming plastically during static indentation are markedly more brittle during sliding contact. Thus differences in the deformation mechanism in these two kinds of tests are expected. However, contrary to what is actually observed, the difference in shear stress should produce more rapid rates of strengthening in hold tests.

More recent nanoindentation tests on quartz indicate plastic deformation [*Masuda et al.*, 2000] and recovered indents, examined both with atomic force microscopy and transmission electron microscopy (TEM), showed no evidence of dislocation motion or fracture. The deformation seems to have been accommodated by a previously unrecognized lattice misorientation mechanism they term "lattice creasing," which may involve generation of small amorphous regions or lattice distortion [*Masuda et al.*, 2000]. *Kailer et al.* [1999] present more detailed microstructural observations that demonstrate that indentation leads to amorphization of quartz. Possibly, similar deformation is associated with frictional sliding; *Yund et al.* [1990] report amorphous material results from frictional slip, though it is unclear whether the amorphous material is a high-pressure phase or highly comminuted granular material. So, it is plausible, even likely, that the deformation mechanisms operating in indentation tests and frictional sliding tests in minerals do not involve conventional dislocation or fracture growth mechanisms.

The most significant constraint on mechanism of time-dependent strengthening observed in laboratory friction tests comes from the study of *Dieterich and Conrad* [1984]. Hold tests were conducted on bare surfaces of quartzite in dry argon and at controlled and room humidity in air. The time-dependent strengthening effect vanished in the dry tests indicating that it is a water assisted effect. More recent tests on quartz gouge by *Frye and Marone* [2003] find a likely related correlation between time-dependent strengthening and water. For these gouges, ~5% relative humidity produces negligible aging, whereas >10% relative humidity leads to healing observed at ambient conditions. While these studies have not allowed the specific mechanism to be identified the prevailing theory of Dieterich [*Dieterich and Conrad*, 1984] is that the effect of water seen in these friction tests is the same effect seen in microindentation tests in nonmetallic solids where extremely dry conditions inhibit yield at highly stressed contacts [*Westbrook and Jorgenson*, 1965].

Determining the mechanisms responsible for frictional strengthening in laboratory experiments is not possible without direct microstructural examination of the deformed material. Such examinations are rarely performed. A

preliminary study to match mechanical data from static and sliding indentation tests with detailed optical, scanning electron microscopy (SEM) and TEM observation of the deformed mineral surfaces was undertaken by B. Evans and D. Kohlstedt [*Viswanathan et al*., 1995; *Viswanathan and Kohlstedt*, 1996; *Eckhardt et al*., 1996]. In experiments on calcite and olivine, deformation consisted of cooperative fracture, dislocation motion, and sliding contact; on the basis of those preliminary results, static indentation and frictional sliding of rock surfaces involve mixed brittle and ductile processes. It is hard to imagine a more fundamentally important study in rock friction than one that establishes the physics of contact-scale deformation, as Evans and Kohlstedt intended. However, owing to lack of funding, that study was not completed.

Temperature Dependence While there is little agreement on mechanisms associated with rate and state effects it is accepted that whatever the mechanism, the temperature dependence of second-order friction effects is consistent with the Arrhenius relation, which requires a linear scaling (equation (13.17b)) RT/Ω of the rate-dependent coefficient with temperature. Linear temperature dependence was first suggested by *Stetsky* [1978]. Later *Chester* [1994] developed a temperature-dependent friction formulation based on laboratory quartz friction data at hydrothermal conditions that incorporated the Arrhenius dependence of the direct rate and aging effects. Using his formulation, Chester successfully modeled rate step data from hydrothermal experiments on quartz to determine the individual temperature dependence of the rate and age dependencies, finding that both effects have similar temperature dependence with an average activation energy 90 kJ/mol. This is consistent with the activation energy of crack growth in quartz [*Atkinson and Meredith*, 1987b]. Similarly, *Blanpied et al.* [1998] analyzed hydrothermal rate stepping tests in granite to determine the temperature dependence of the individual parameters a and b. Though they did not determine them, activation energies can be inferred from their analysis and tabulated data.

The most compelling observations of this temperature dependence are *Nakatani*'s [2001], whose experimental technique isolated the direct rate dependent coefficient a at temperatures between 25° and 800°C in a feldspar gouge layer (fig. 13.27). While the low-temperature activation energy for the process underlying a again is in the range of 90 kJ/mol, suggestive of subcritical crack growth, Nakatani argues against crack growth and implies that ductile flow of some form is responsible. Again, there is no consensus on mechanism, only on the form of the temperature dependence. Comparable direct determinations of the temperature dependence of b have not been made.

Relative Roles of Elastic and Inelastic Processes

While either inelastic or elastic friction theories predict a constant friction coefficient [*Bowden and Tabor*, 1950; *Greenwood and Williamson*, 1966], laboratory tests can easily distinguish between these two end-member models. Tests by

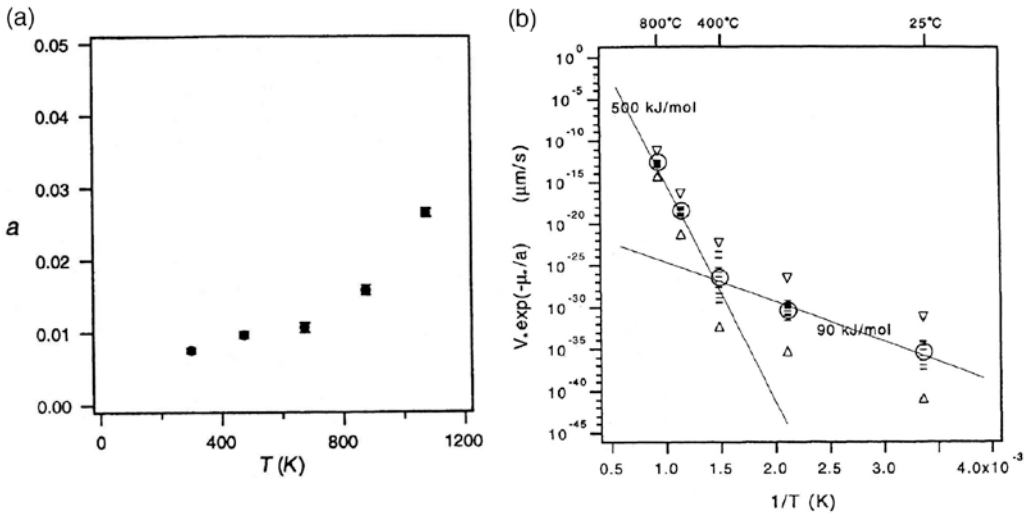

Figure 13.27 Data on the temperature dependence and activation energy of the instantaneous rate dependence of friction of sodium feldspar gouge [from *Nakatani*, 2001]. (a) Approximately linear dependence of *a* on temperature, consistent with expectations from the Arrhenius rheology (e.g., equation (13.17). (b) Inferred activation energy from the same experiments as in figure 13.27a, assuming an equation of the form of equation (13.17).

Linker and Dieterich [1992] provide the current state of knowledge on the roles of elastic and inelastic processes in rock friction, albeit for granite and room temperature. Both reversible (elastic) and displacement-dependent (inelastic) changes in shear resistance occur when the normal stress is changed [*Linker and Dieterich*, 1992] (fig. 13.28a). The reversible changes in shear stress with normal stress probably reflect the increase in the number of contacts and increase in area of existing contacts as a function of normal stress due to elastic closure as in the work of *Greenwood and Williamson* [1966]. The inelastic changes with associated displacement dependence are of the same sense as the elastic changes and probably reflect changes in dilatant volume due to time-dependent ductile flow at asperity contacts, modulated by slip. In other words, the inelastic effects are due to the same kind of age dependence as seen in constant normal stress experiments [*Linker and Dieterich,* 1992]. The reversible changes are as large as or larger than the inelastic changes so a significant portion of the pressure dependence of fault strength in experiments is probably due to elastic changes in contact area and dilatant volume.

Normal stress effects are well modeled by modification of the rate and state equation (13.15) [*Linker and Dieterich*, 1992]; the following formulation is equivalent to *Linker and Dieterich* [1992] but is slightly modified to more clearly reflect the partitioning between elastic and inelastic changes in contact area associated with normal stress change. For step changes in normal stress at con-

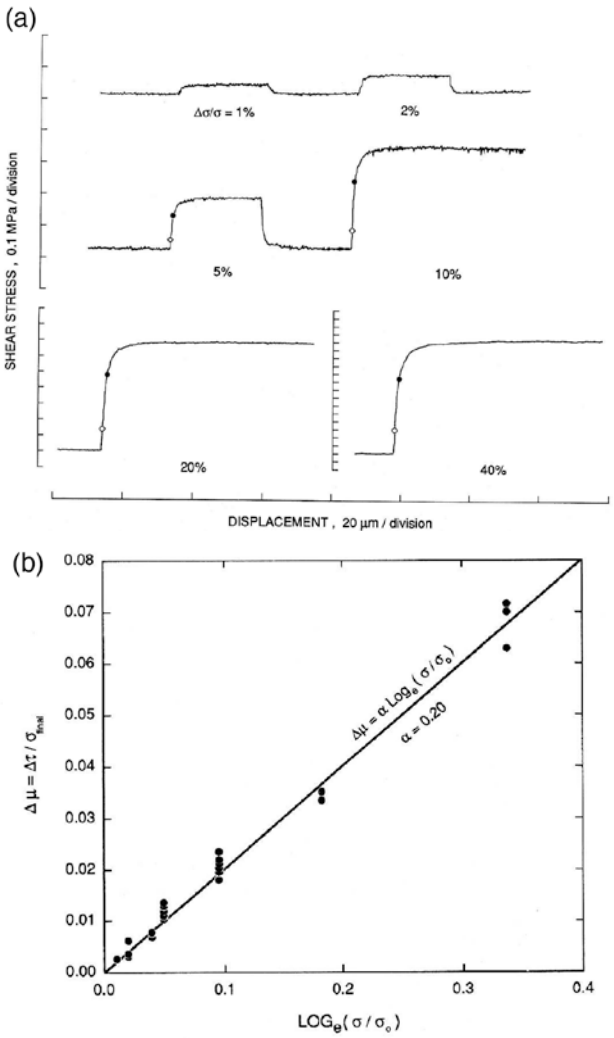

Figure 13.28 Effect of changes in normal stress on shear stress for bare granite at room temperature and 5 MPa normal stress [*Linker and Dieterich*, 1992]. (a) Shear stress versus displacement for changes in normal stress of 1, 2, 5, 10, 20, and 40% of the ambient value. Note that the 40% change is shown at a compressed vertical scale compared to the other tests. The response has three components; there is an instantaneous change marked by the open circle. This is a machine effect due to Poisson expansion of the fault surface as the fault normal stress is changed. There is an additional instantaneous change from the open circle to the solid circle; this is interpreted as elastic increase in contact area due to the increased normal stress. Subsequently, with displacement, there is a further increase in shear resistance that is interpreted as inelastic, time-dependent yielding of asperity contacts. (b) Summary of tests of the type shown in figure 13.28a as a function of the size of the normal stress change. Here σ is the final normal stress, σ_0 is the initial normal stress, and $\Delta\mu$ is the inelastic component of the change in shear stress, normalized by the final normal stress.

stant slip rate, the inelastic change in shear stress depends logarithmically on the size of the shear stress change as

$$\frac{\Delta\tau}{\sigma_e} = \alpha \ln \frac{\sigma_e}{\sigma_0} \tag{13.18a}$$

(fig. 13.28b), where σ_0 is the starting normal stress [*Linker and Dieterich*, 1992]. If these shear stress changes are equated with changes in steady-state contact age $\Delta\tau/\sigma_e = b \ln(\theta_{ss}/\theta_0)$, state changes with normal stress as

$$\theta_{ss} = \theta_0 \ln\left(\frac{\sigma_e}{\sigma_0}\right)^{\alpha/b} \tag{13.18b}$$

Linker and Dieterich [1992] assume that at the time of the normal stress change, the contact age is instantaneously offset by the amount given by equation (13.18b). However, changing contact age without significant slip or time passage is confusing. In the present treatment it's assumed there is no instantaneous change in age, rather there is reversible instantaneous change in shear resistance that represents the elastic change in contacting area. A normal stress change subsequently induces the asperity contact population to evolve to a new steady-state age that represents the inelastic change in contacting area at the new normal stress. A modification of the standard evolution law (equation (13.15b)), which has the required steady-state value and that behaves otherwise identically to equation (13.15b), is

$$\frac{d\theta}{dt} = \left(\frac{\sigma_e}{\sigma_0}\right)^{\alpha/b} - \frac{V\theta}{dc} \tag{13.19a}$$

σ_0 can be considered a constant reference value, and the steady-state value of age is $\theta_{ss} = (d_c/V)(\sigma_e/\sigma_0)^{\alpha/b}$. To maintain steady-state friction independent of normal stress, equation (13.19a) is used with the modified relation for friction

$$\mu = \mu_o - \alpha \ln(\sigma_e/\sigma_0) + a \ln(V/V_0) + b \ln(V_0\,\theta/d_c) \tag{13.19b}$$

Here, steady-state friction is assumed independent of normal stress, and the total pressure dependence of strength is $d\tau/d\sigma_e = \mu_{ss}$. For this relation (13.19) the total pressure dependence is the sum of the elastic pressure dependence $\mu_{ss} - \alpha$, and the inelastic pressure dependence α. The ratio of inelastic to total pressure dependence is α/μ_{ss}, and α is some measure of the role of inelastic fault normal creep in rock friction. The value α is bounded $0 \le \alpha \le \mu_{ss}$ [*Dieterich and Linker*, 1992]. For materials corresponding to purely inelastic friction [*Bowden and Tabor*, 1950] $\alpha = \mu_{ss}$; for purely elastic friction [*Greenwood and Williamson*, 1966] $\alpha = 0$. For Westerly granite $\mu_{ss} = 0.7$ and $\alpha = 0.2$ and roughly 30% of the pressure dependence results from inelastic creep.

Stability Condition for Normal Stress Changes As described immediately above, information about contact-scale process associated with the second-order friction effects can be derived from normal stress stepping tests in the laboratory; unfortunately, such tests are rarely implemented. The stability of slip following normal stress change is important in natural circumstances of nonplanar faults, such as in most subduction zones, and where faults intersect the Earth's surface. Stability of an expression equivalent to equation (13.19) was analyzed using an inclined slider-block geometry with spring angle ϕ by *Dieterich and Linker* [1992]. The value ϕ is the angle between the loading direction and the fault. Ignoring second-order effects for the moment, the inclusion of coupling between slip and normal stress can have a stabilizing or destabilizing effect. Since $\tau = \mu\sigma_e$, if normal stress goes down with slip, the shear resistance goes down. In this way, decreasing normal stress reduces the resistance to slip rate acceleration, a potentially unstable situation. The second-order effect on normal stress is a tendency for the normal stress to initially change by a bit less than $\mu\Delta\sigma_e$ so that, in the potentially unstable case of decreasing normal stress, the $\alpha\ln\sigma$ term stabilizes slip [*Dieterich and Linker*, 1992]. These characteristics are well reflected by the *Dieterich and Linker* [1992] stability criteria for equations (13.19a) and (13.19b):

$$k_c = \frac{(b-a)\sigma_e}{d_c[1+(\mu_{ss}-\alpha)\tan\phi]} \tag{13.19c}$$

The critical stiffness increases for negative friction angle (normal stress decreases with slip), encouraging instability. However, this tendency is counteracted somewhat by nonzero α.

Dilatancy and Slip Instability

In applying the stability criteria (13.16a) or (13.19c) to models of crustal seismicity to date [e.g., *Tse and Rice*, 1986; *Stuart*, 1988] it is always assumed that the steady-state rate dependence is independent of the ambient fault strength μ_0, as the empirical parameters (*b*-*a*) and α are assumed independent of nominal frictional strength. Were this true aseismic faulting is no less likely in intrinsically weak materials than in strong materials, despite some observational evidence to the contrary in weak transform environments [*Boettcher and Jordan*, 2004] and in subduction zones [*Byrne et al.*, 1988; *Moore and Saffer*, 2001]. However, close examination of the underpinning of rate and state equations suggests the steady-state rate dependence and the nominal strength are not independent. In equation (13.14) the constitutive parameter *b*, which controls the size of the age dependence is $b = -\mu_0\beta/\sigma_0$, recalling that μ_0 is the nominal strength, σ_0 is the contact normal stress and β is the intrinsic time dependence of the contact normal stress. So *b* depends directly on the nominal frictional strength and the *a* parameter is not so tied to μ_0; all other factors being equivalent, intrinsically

weak materials should tend to have smaller aging, more positive rate dependence and therefore more aseismic response than strong materials.

This relationship between b and μ_0 results from an interpretation of empirical constitutive equations. However, it is consistent with the role of dilatancy in controlling seismic potential, as follows. Recall from the earlier discussion of pressure dependence of intact rock failure and friction that pressure dependence is a consequence of reduction of dilatant volume with increasing normal stress. In this sense, pressure dependence measures "ease of dilatancy"; large pressure dependence associated with large changes in dilatant volume. Thus weak materials are less easily dilated than strong materials. Recall also from the discussion of second-order effects that at constant fault normal stress in the absence of slip, contact area increases with time (fig. 13.17), fault strength increases (fig.13.18), and dilatant volume is reduced. This time-dependent reduction in dilatant volume is counterbalanced by slip-induced dilatancy (fig. 13.20), and the aging effect is directly related to dilatancy. The parameters μ_0 and b are expected to be strongly correlated. Equation (13.15) reflects this connection naturally. As b is a small fraction of total pressure dependence, e.g., 1–2 % for strong quartzofeldspathic material with $\mu = 0.7$ $b = 0.01$, it is reasonable to expect that for weak materials with low friction say $\mu = 0.2$ that b is proportionally smaller at 0.003. However, this is a speculative and untested hypothesis.

Note also that the normal stress effect on friction (equation (13.19)) is dilatancy related: α is the inelastic pressure dependence of strength having value equivalent to up to 30% of the total pressure dependence for granite. Though there is no data for α for any weak material, the inelastic dilatancy is expected to be a similar percentage of the total. So for a material with $\mu = 0.2$, α should be proportionally small at 0.06. This is also an untested prediction.

Some Other Aspects of Rock Friction

Other aspects of rock friction and the character of frictional sliding on monomineralic weak faults are illustrated using experiments of *Scruggs* [1997] conducted on gouge layers of muscovite between rings of porous ceramic in a high-pressure, computer-interfaced rotary shear apparatus [*Tullis and Weeks*, 1986; *Reinen et al*., 1994]. Muscovite was chosen so that results could be compared with single-crystal deformation experiments of *Mares and Kronenberg* [1993]. Additionally, a number of surface physics and surface forces measurements have been made on muscovite cleavage fragments in the presence of fluids [*Israelachvili*, 1992], making it an ideal material for initial studies of the physics of high-pressure mineral friction. Muscovite has similar crystal structure and friction as illite, and therefore is an appropriate analogue for studying aspects of subduction zone faulting within the illite stability field.

The gouges were prepared by crushing and passing the fragments through standard sieves at room temperature and humidity; the size fraction smaller

than 74 μm is used. The amount of gouge used resulted in an ~1.0-mm-thick layer when compacted under load. Surface preparation of the ceramic forcing blocks was performed at room temperature and humidity. The rock rings were ground to height with a surface grinder and then abraded with #100 SiC grit on a glass plate. At the start of an experiment, confining pressure was raised to the appropriate value. Axial load was then raised to bring the normal stress to final load. Both shear stress (torque) and axial load were measured with a combined load and torque cell located within the pressure vessel. Constant rate loading was provided by an electrohydraulic stepping motor. Fault displacement is measured directly by a high-resolution resolver [*Weeks and Tullis*, 1992]. Changes in gouge thickness are determined from the relative length of the sample column recorded by a linear variable differential transformer (LVDT). Data were recorded digitally at fixed time intervals, with a maximum frequency of 10 samples/s. Measurements were obtained simultaneously for gas pressure, axial load, torque, room temperature, displacement (rotation angle), and the length of the loading column.

Sliding tests on muscovite were conducted at 25, 50, 100, and 150 MPa, and the shear stresses are linear with increasing normal stress defining friction $\mu = \mu_f = 0.364$ [*Scruggs and Tullis*, 1998] (fig. 13.16). Similarly, the steady-state rate dependence of shear strength is linear with increasing normal stress (fig. 13.29a). The rate dependence is positive and rate stepping tests show a very small age-dependent effect, roughly ⅙ of the direct rate-dependent effect (fig. 13.29b). Measured in this way, there appears to be very little ongoing time-dependent creep and shear-induced dilatancy relative to the direct rate dependence of shearing. This conclusion is borne out by slide-hold-slide tests; these show a small component of time-dependent strengthening $b = 0.0007$ (fig. 13.29c). The coefficient b inferred from these tests is also insensitive to normal stress. These results are consistent with the assumptions leading to equation (13.14), suggesting that at all pressures in this range, the nominal and second-order effects are independent of normal stress.

Degree of Localization

Characteristic Displacement These tests illustrate two other aspects of rock friction observed in laboratory tests. In rate stepping tests, the age-dependent effect has a characteristic length $d_c \approx 125$ μm more than 25 times larger than observed in step tests on bare surfaces of granite or quartz. It seems unlikely that d_c this large is controlled by asperity contact dimension alone and slip to return friction to its residual level ($\sim 4 \times d_c$) is of the order of the gouge thickness. As suggested first by *Marone and Kilgore* [1993], deformation in gouge can be distributed rather than localized, and if it is distributed, the observed characteristic sliding dimension must be longer and related to both to the asperity contact dimension and the width of the deforming zone, as follows. For fully localized slip, the steady-state value of fault age can be related to the contact strain $d\delta/d_{c,}$ where d_c is the representative contact dimension. The contact shear

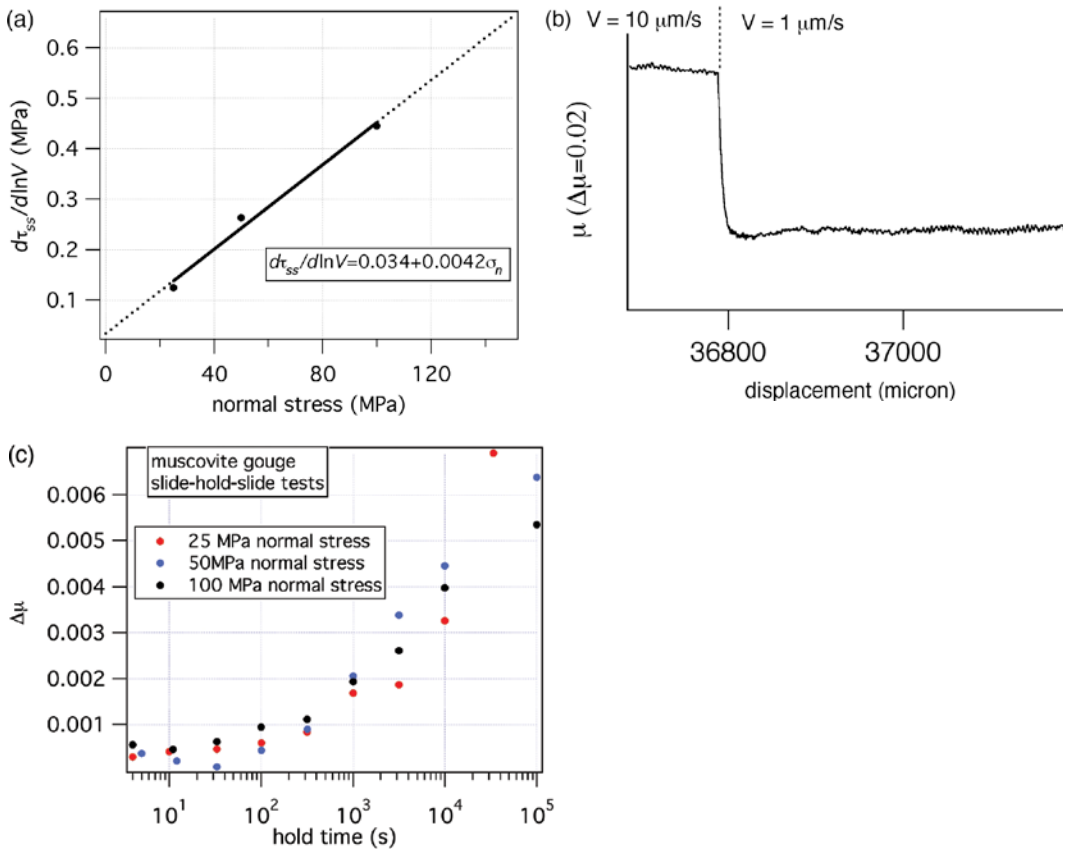

Figure 13.29 Muscovite gouge rate dependence and time dependence from *Scruggs*, 1998]. (a) Steady-state rate dependence from rate stepping tests at three normal stresses. The rate steps were between 1 and 10 μm/s. The points represent the average of 52, 62, and 50 measurements made at 25, 50, and 100 MPa, respectively. The standard deviation is between 13 and 8% for these measurements. There is no evidence of significant changes in the rate dependence with normal stress in this range. A fit to the data gives a slope of 0.0042, which is *a-b* from equation (13.15). (b) Typical rate step from 10 to 1 mm/s, showing the relatively large instantaneous rate dependence and the small age dependence. (c) Results of slide hold slide tests at the same three normal stresses shown in figure 13.29a. There is no evidence of significant changes in the rate of time dependent strengthening with normal stress. The rate of strengthening is very small, compare with typical quartzofeldspathic rates (fig 13.18).

strain rate then is $\gamma_c = V/d_c = 1/\theta_{ss}$. If instead strain is distributed within a layer, slip occurs on many slip surfaces within the layer. The number of slip surfaces is related to the average grain size D and the thickness of the deforming layer w, $N_c \propto w/D$. The characteristic length is the average contact dimension d_c times the number of slip surfaces $D_c = d_c N_c$. So for gouge the characteristic displacement is expected to be larger than for bare surfaces by an amount

related to the thickness of the deforming layer $D_c \propto d_c w/D$. For gouge the contact strain rate is $\gamma_c = 1/\theta_{ss} = V/D_c \propto VD/wd_c$.

Effective Cutoff Time The characteristic length also influences aspects of slide hold tests results via the effective cutoff time [*Nakatani*, 2001]. Time-dependent strengthening in hold tests can only be measured at hold times longer than an effective characteristic time. The effective characteristic time is approximately the age at the start of the hold. For example, if a hold test could be conducted where fault slip ceased immediately during the hold period, then age (equation (13.15b)) would change with time during the hold as $\theta = \theta_o + t$ and age would contribute to fault strengthening as $b\ln(\theta_o + t)$. The parameter θ_0 is the starting value of state and the effective cutoff time of *Nakatani* [2001]. As hold tests start at steady state, the cutoff time is $\theta_{ss} = \theta_o = D_c/V$ and will scale directly with the characteristic slip distance. The muscovite experiment illustrates the long cutoff time for gouge (fig. 13.29c) relative to bare surfaces of granite or quartzite.

Shear Localization and Rate Dependence Because of the longer displacement length scale for gouge layers, gouges can be more stable than bare surfaces (e.g., equation (13.16b)). In addition, the actual rate dependence of gouge layers is more positive than for bare surfaces of the same composition [*Byerlee and Summers*, 1976; *Marone et al.*, 1990]. Although explanations of this difference in rate dependence have been proposed, most notably that the difference is related to the shear dilatancy rate [*Marone et al.*, 1990], the source of the difference in rate dependence is not known [*Marone*, 1998].

A convincing explanation notwithstanding, the degree of localization in gouge should directly reflect the rate dependence. Velocity-dependent fault strength relations lead directly to a strain localization/delocalization criteria derived by requiring that work is minimized. Ignoring dilation, mechanical work is normally written as $W = \int \tau d\gamma$ but when $d\tau/d\gamma$ does not change sign, W can be equivalently expressed as $W = \int \gamma d\tau$. Then $dW = \gamma d\tau$, and an increment of work is $dW/d\delta = \gamma d\tau/d\delta$. Reduction of work requires $dW/d\delta < 0$ and so shear stress must decrease with displacement $0 > d\tau/d\delta$. For a velocity-dependent material, $\tau = f(\dot{\gamma})$ and

$$\frac{d\tau}{dw} = \frac{\partial \tau}{\partial \dot{\gamma}} \frac{d\dot{\gamma}}{dw} \tag{13.20a}$$

Here, the engineering shear strain is $\gamma = \delta/w$ and w is the thickness of the deforming zone. The shear strain rate is $\dot{\gamma} = V/w$. Taking derivative of strain rate with respect thickness leads to

$$d\tau = -\frac{V}{w^2} \frac{\partial \tau}{\partial \dot{\gamma}} dw \tag{13.20b}$$

equivalently

$$\frac{d\tau}{d\delta} = -\frac{V}{w^2}\frac{\partial\tau}{\partial\dot{\gamma}}\frac{dw}{d\delta} \tag{13.20c}$$

Using the requirement of decreasing shear strength with shear strain yields

$$0 > -\frac{V}{w^2}\frac{\partial\tau}{\partial\dot{\gamma}}\frac{dw}{d\delta} \tag{13.20d}$$

$\partial\tau / \partial\dot{\gamma}$ is the rate dependence of fault strength, which can be either negative or positive and because V and w are both positive, equation (13.20) defines the localization criteria. If the velocity dependence is positive, then $dw/d\delta$ is positive and the shear zone widens with displacement. *Mair and Marone* [1999] found that D_c increased with slip velocity for a case in which shear is distributed, consistent with delocalization. Conversely, if the velocity dependence is negative $dw/d\delta$ is negative and the shear zone localizes. In rate-strengthening gouges such as the muscovite example, the deformation will tend to be distributed leading to the large characteristic slip distance.

Constraints on Contact-Scale Deformation Mechanism

The experimentally inferred coefficients a and b from the muscovite experiments can be compared for consistency of mechanism with the rate dependence of intact strength measured at room temperature in single crystals of muscovite by *Mares and Kronenberg* [1993]. The normalization scheme developed in the Constraints on Contact-Scale Mechanism, Mostly for Strong Materials section is applied to correct for the unknown contact stresses in friction tests. The dislocation glide flow law [e.g., *Mares and Kronenberg*, 1993], has the Arrhenius form (equations (13.17) and (13.5a)), where the appropriate stress measure in this case is the differential stress $\sigma_\Delta = \sigma_1 - \sigma_3$, $\dot{\varepsilon} = \dot{\varepsilon}_* \exp[-(E_* - \sigma_\Delta\Omega)/kT]$. The reference strain rate $\dot{\varepsilon}_*$ is not arbitrary. To use an arbitrary reference, strain rate proportional to $\dot{\varepsilon}_*$, define $\dot{\varepsilon}_0 = c\dot{\varepsilon}_*$. Doing so makes the nominal strength $\sigma_{\Delta 0} = E_*/\Omega + \mathbf{A}\ln c$. The rate-dependent coefficient is $\mathbf{A} = kT/\Omega$. The normalized equation analogous to equation (13.17e) is

$$\frac{\sigma_\Delta}{\sigma_{\Delta 0}} = 1 + \frac{\mathbf{A}}{\sigma_{\Delta 0}}\ln\frac{\dot{\varepsilon}}{\dot{\varepsilon}_0} \tag{13.21}$$

for comparison with equation (13.17f). Geometric differences between measured differential stress σ_Δ in rock deformation tests and shear stress τ in friction tests, $\tau = 0.5\sigma_\Delta \sin 2\beta$, where β is the angle between the fault normal and the greatest principal stress, are eliminated by the normalization. To compare the instantaneous rate-dependent coefficients, the slip velocity in equation (13.17f) must be converted to strain rate and the nominal strength should be

associated with the same reference strain rate $\dot{\varepsilon}_0$ for both equations (13.17f) and (13.21). Taking d_c from the friction relation to be ½ the average contact dimension, the strain rate for friction is $\dot{\varepsilon} = V/2d_c$.

Microstructural analysis of muscovite single crystals deformed at pressure between 50 and 400 MPa and temperatures between 20° and 400°C with σ_1 at 45° to the 001 plane, indicates deformation predominately by dislocation glide [*Mares and Kronenberg*, 1993]. Analysis of the three 400°C rate stepping experiments of *Mares and Kronenberg* [1993] (fig. 13.30), taking $\dot{\varepsilon}_0 = 1 \times 10^{-1}$, produces a normalized coefficient of rate dependence of dislocation glide $\mathbf{A}/\sigma_{\Delta 0} = 0.034$. To compare with room temperature friction data, the difference in temperature (673K to 295K) introduces factor of 2.3 reduction in **A** of the single-crystal data. The *Mares and Kronenberg* [1993] single-crystal data extrapolated to room temperature is then $\mathbf{A}/\sigma_{\Delta 0} = 0.015$.

To estimate the normalized coefficient of rate dependence for room temperature friction of muscovite, $\dot{\varepsilon} = V/2d_c$ is assumed. There is ambiguity in the strain rate due to shear being possibly distributed in a 1-mm-thick layer. If the deformation is distributed within the layer, the characteristic distance d_c is related both to the average contact dimension and the thickness of the actively deforming layer [*Marone and Kilgore*, 1993]. The value d_c = 125 μm inferred from rate stepping tests is larger than bare surface experiments, consistent with more distributed deformation. Fortunately, the normalization is insensitive to differences in strain rate of this magnitude; using a d_c of 9–125 μm, μ_0 varies from 0.359 to 0.372 and $\mathbf{A}/\tau_0 = 0.017$ for either choice. This normalized

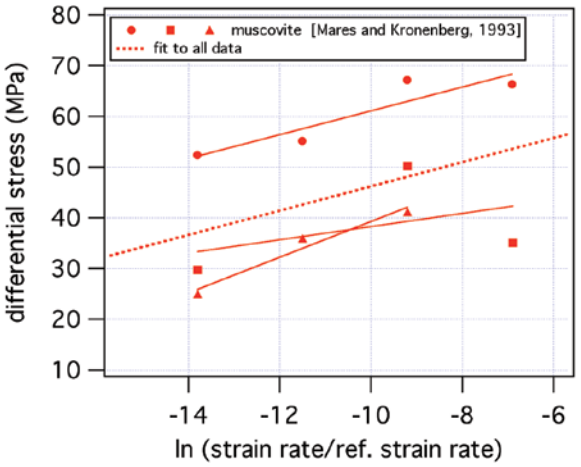

Figure 13.30 Rate dependence of low-temperature plasticity in muscovite at 400°C and 200 MPa confining pressure [*Mares and Kronenberg*, 1993]. These are rate stepping test data from three experiments. The dashed line represents the average strength and rate dependence. The lower axis has been normalized by a reference strain rate of 1×10^{-1}/s.

rate dependence is nearly identical to the single-crystal glide value, suggesting that the instantaneous rate dependence in muscovite could be related to dislocation motion. If glide does control the instantaneous rate dependence of friction, a would scale linearly with temperature, consistent with recent process based rock friction theories [e.g., *Rice et al.*, 2001; *Nakatani*, 2001] and direct measurements made by *Nakatani* [2001].

In low-velocity friction tests on serpentinite, *Reinen et al.* [1994] observed a transition to a more strongly rate-dependent process. Similar low-velocity rate stepping and hold tests on muscovite do not produce such a transition and the rate dependence in the velocity range 0.001–10 μm/s is approximately constant. A preliminary conclusion is that dislocation glide is possibly responsible for the direct rate dependent effect in muscovite. As the age-dependent coefficient $b/\sigma_0 = 0.0028$ is small, it seems to be unrelated to conventional low-temperature crystal flow.

Bond Strength in Sheet Silicates Consistent with the implied role of dislocation in muscovite rate dependence are recent results on the frictional strength of truly dry muscovite and other weak sheet silicate minerals (micas, clays) where that base level friction is controlled by the interlayer bond strengths [*Morrow et al.,* 2000; *Moore and Lockner*, 2004] (fig. 13.31). Experiments on 6-sheet silicate minerals by *Morrow et al.* [2000] and 10-sheet silicate minerals by *Moore and Lockner* [2004], carefully vacuum dried and deformed under dry conditions, show a systematic relationship between measured friction and the estimated bond strength [*Giese*, 1978, 1980*; Bish and Giese*, 1981]. Bond strength in this case is the separation energy, the energy necessary to separate individual sheets along the [001] basal cleavage. Separation energy was calculated by Giese and coauthors by considering energy change of electrostatic bonding with distance of separation. This correlation between measured fault strength and calculated bond strength extends from the weakest (talc) to lizardite serpentine, gibbsite, and kaolinite whose dry friction is equivalent to Byerlee's law. The electrostatic bond energy of these minerals exceed ~70 kcal/mol and the brittle mica margarite, which has separation energy nearly 3 times these more weakly bonded sheet silicates has the same frictional strength (fig. 13.31). These observations suggest a threshold bond strength below which interlayer bond energy determines friction and above which other mineralogy independent processes determine the nominal frictional strength. At least for the sheet silicates with separation energies below 70 kcal/mol, nominal dry frictional strength is determined by breaking interlayer bonds rather than pure sliding between previously broken cleavage fragments [*Moore and Lockner*, 2004]. This inference is consistent with direct measurement of the shear strength of previously cleaved mica sheets and observations that indicate the adhesive strength of cleaved surfaces is comparable to the interlayer bond strength [*Bailey and Courtney-Pratt*, 1955; *Israelachvili and Adams*, 1976]. Asperity contact-scale processes determining the strength of weak sheet silicate minerals are likely to

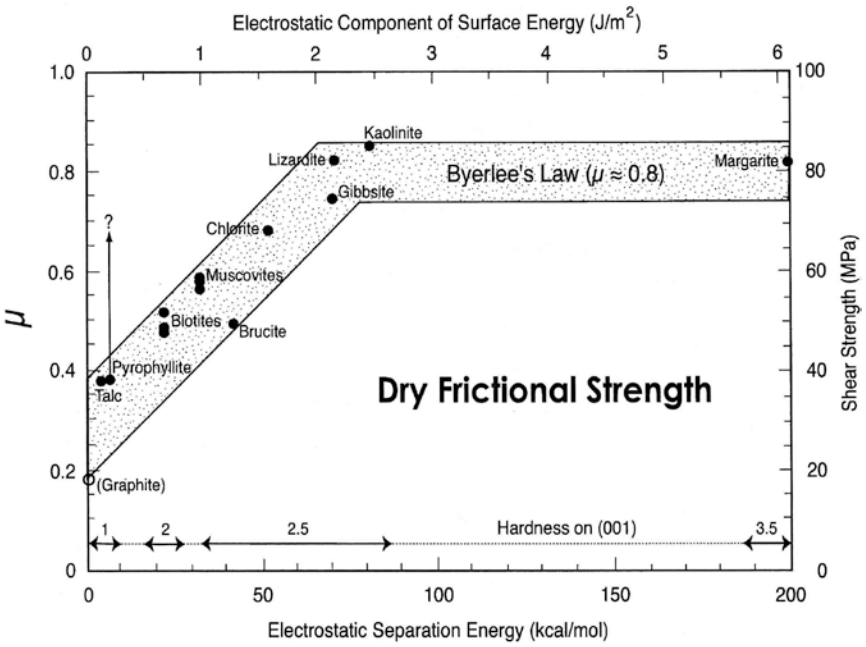

Figure 13.31 Variation of dry peak friction (left) versus estimated electrostatic separation energy for sheet silicate minerals at room temperature and 100 MPa confining pressure. The samples were oven and vacuum dried, and deformed dry. Hardness measured on the basal plane is shown as an alternative axis at bottom. Figure from *Moore et al.* [2004].

be fundamentally different than those of stronger phases whose strengths are well characterized by Byerlee's law [*Byerlee*, 1978].

Effects of Pore-Fluid Pressure on Fault Strength and Stability

The presence for water can have a large effect on fault strength and stability. Discussion of chemical effects of water on strength is deferred to the next section. Absolute fault strength depends to first order on pore pressure through the effective pressure relation (see the Rock Failure section). Pore pressure affects fault stability in two ways. First, effective normal stress reduces the seismic potential by reducing the critical stiffness for unstable slip (equation (13.16b)). As the effective normal stress goes down, the displacement rate of strength loss $(b-a)\sigma_e/d_c$ decreases. The other way that pore pressure affects fault stability is through dilatancy hardening [*Frank*, 1965; *Rice*, 1975; *Rudnicki and Chen*, 1988]. Dilatancy hardening is an increase in the effective pressure

caused by decreasing pore pressure and increasing porosity owing to shear-induced dilatancy. As all faults appear to dilate prior to seismic slip, if the fault zone is not fully drained, the pore pressure goes down as failure is approached and the effective normal stress goes up causing the fault to become incrementally stronger.

The implications of dilatancy hardening on sliding stability are an extension of the constant normal stress equation (13.14b) [*Segall and Rice*, 1995]. Dilatancy associated with changes in sliding velocity (fig. 13.20) [*Morrow and Byerlee*, 1989; *Marone et al.*, 1990] can be characterized by assuming a steady-state porosity associated with each slip rate and that porosity evolves exponentially with slip,

$$\frac{d\phi}{dt} = -\frac{V}{d_c}(\phi - \phi_{ss}) \tag{13.22a}$$

Figure 13.32 shows comparison by *Segall and Rice* [1995] of a simulation with equation (13.22a) to data of *Marone et al.* [1990]. Steady-state porosity is assumed purely rate dependent

$$\phi_{ss} = \phi_o + \varepsilon \ln\left(\frac{V}{V_o}\right) \tag{13.22b}$$

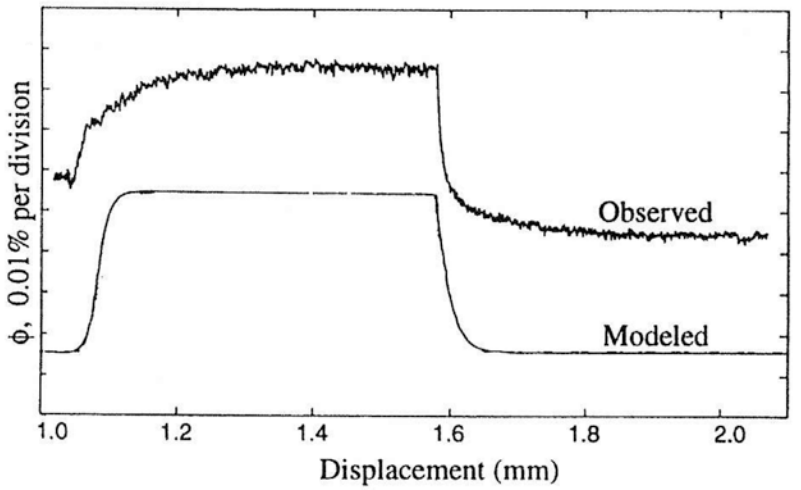

Figure 13.32 Observed and modeled changes in porosity due to a change in slip velocity from 1 to 10 μm/s for a 3-mm quartz gouge layer at room temperature and 150 MPa normal stress. The data are from the study of *Marone et al.* [1990], the model is calculated with equations (13.22a) and (13.22b) by *Segall and Rice* [1995]. The figure is from *Segall and Rice* [1995].

At constant normal stress and undrained conditions (constant fluid mass) the rate of pore pressure change is fixed by the rate of inelastic porosity change

$$\frac{dp}{dt} = -\frac{d\phi_m}{dt}\frac{1}{\phi(\beta_f + \beta_\phi)} \tag{13.22c}$$

where β_f and β_ϕ are the fluid and pore compressibilities respectively. Equations (13.22) and (13.15) describe slip within a saturated fault zone. Using the effective pressure relation $\tau = \mu(\sigma_n - p)$ and assuming that the undrained steady-state rate dependence results from the sum of intrinsic rate dependence and a contribution due to dilatant pore pressure change leads to

$$\left.\frac{d\tau_{ss}}{d\ln V}\right|_m = \left.\frac{d\tau_{ss}}{d\ln V}\right|_p - \mu\left.\frac{dp}{d\ln V}\right|_m \tag{13.23a}$$

The first term on the right is the drained rate dependence $(a - b)(\sigma_n - p)$. The second right-side term is found by *Segall and Rice* [1995] from equation (13.22) to be

$$\left.\frac{dp}{d\ln V}\right|_m = -\frac{\varepsilon}{\phi(\beta_f + \beta_\phi)} \tag{13.23b}$$

giving

$$\left.\frac{d\tau_{ss}}{d\ln V}\right|_m = (a-b)(\sigma_n - p) + \frac{\mu_{ss}\varepsilon}{\phi(\beta_f + \beta_\phi)} \tag{13.23c}$$

Substituting this result into equation (13.16b) gives the undrained critical stiffness [*Segall and Rice*, 1995]

$$k_c = \frac{1}{d_c}\left[(b-a)(\sigma_n - p) - \frac{\mu_{ss}\varepsilon}{\phi(\beta_f + \beta_\phi)}\right] \tag{13.23d}$$

This expression includes both effects of pore pressure on stability: the first term on the right-hand side describes the sensitivity to effective stress where high pore pressure (low effective stress) decreases the critical stiffness. This is a stabilizing effect of high pore pressure. The second right-side term is dilatancy hardening; as the ratio of the dilatancy coefficient to porosity ε/ϕ increases, the critical stiffness goes down.

As shown by the derivation of equation (13.23d) and by simulations and analysis conducted by *Segall and Rice* [1995], the presence of undrained pore

pressure tends to stabilize faults and high pore pressure significantly discourages seismicity. *Segall and Rice* [1995] concluded for laboratory-measured values of μ_{ss}, ε, a-b, and d_c for quartz that it is not possible to have seismic slip on faults that are apparently weak enough to satisfy the San Andreas heat-flow constraint $\mu < 0.2$). Partly, this result is due to the high values of ε and μ_{ss} from the limited existing laboratory data from quartz gouge layers. These constraints lead to the conclusion that apparently weak fault zones tend to be more aseismic than strong ones.

However, the implications of equation (13.23) for intrinsically weak, low dilatancy materials such as clays and phyllosilicates, as may exist in subduction zones, are unexplored. By using data from quartz, dilatancy hardening and intrinsic strength assumed by *Segall and Rice* [1995] are at their respective maximums, making the second right-side term large, favoring stability. Intrinsically weak, low dilatancy materials will have much smaller contributions from the second term. On the other hand, as argued in the Dilatancy and Slip Instability section above, intrinsically weak materials tend to have small b coefficients, making them less likely to be intrinsically unstable, keeping in mind that the relation between intrinsic stability and intrinsic strength proposed in the Dilatancy and Slip Instability section is speculative. Because some seismic subduction zones may be intrinsically weak [e.g., *Moore and Saffer*, 2001] and may have pore pressure elevated above hydrostatic [e.g., *Moore and von Huene*, 1980], given the present state of knowledge, it would be unwise to unequivocally relate sliding stability and apparent fault strength.

Chemical Effects of Pore Fluid

To this point, the pressure dependence of strength has been explicitly assumed to arise from increased area of contact (simplifications of equation (13.3c)). An implication of this assumption is that with increasing confining pressure as the fault-zone material becomes denser, larger increments of elastic or inelastic strain energy are required to further compact the fault and increase the contact area. In the limit, as the contact area approaches the total fault area, the amount of strain energy required to further increase the contact area becomes infinite. Thus it is expected and observed that the pressure dependence decreases with increasing confining pressure, both for friction [e.g., *Raleigh and Paterson*, 1965] and for intact failure (e.g., fig. 13.2). However, there are exceptional instances where pressure dependence increases with normal stress or confining pressure. These cases are associated with fault weakness. The best-documented examples of this behavior are for wet clay [*Morrow et al.*, 1992] and wet chrysotile serpentine [*Moore and Lockner,* 2004] (fig. 13.33). Both are weak when dry and weaker when saturated. In general, sheet silicates are weakened by the presence of water; apparently, the strength reduction measures water affinity [*Morrow et al.*, 1992; *Moore and Lockner,* 2004]. Cleavage surfaces are highly

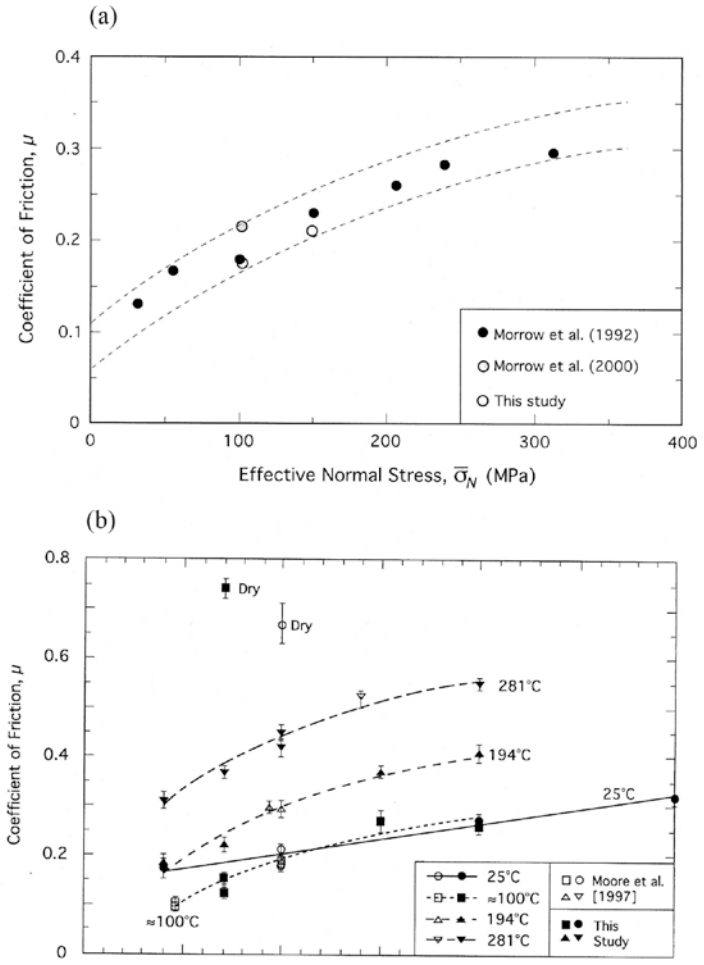

Figure 13.33 Examples of "reverse" pressure dependence where the coefficient of friction $\mu_f = \partial\tau/\partial\sigma_e$ increases with normal stress. Both examples are for drained, water saturated gouge layers. (a) Montmorillonite from *Morrow et al.* [1992, 2000] and *Moore and Lockner* [2004]. Figure is from *Moore et al.* [2004]. (b) Chrysotile serpentinite, data from *Moore et al* [1997], *Moore and Lockner* [2004], figure from *Moore and Lockner* [2004].

charged and water is attracted and bonded to surfaces in a structured film [*Israelachvili et al.,* 1988]. The bonding of structured water influences macroscopic shear strength. The increasing pressure dependence seen for montmorillonite and chrysotile is probably due to the reduction in thickness of the bound intergranular layer with increasing normal stress, as shown by *Rutter* [1983] in statically loaded kaolinite layers. The presence of a water layer with pressure-dependent thickness is a case that violates the equation (13.10b) and instead

the pressure dependence results from the sum of changes in contacting area and changes in shear strength of the water layer

$$\frac{d\tau}{d\sigma_e} = \frac{\partial\tau}{\partial A_f}\frac{dA_f}{d\sigma_e} + \frac{\partial\tau}{\partial\tau_f}\frac{d\tau_f}{d\sigma_e} \tag{13.24}$$

As water dramatically reduces the strength of all sheet silicates [*Morrow* et al., 2000; *Moore and Lockner*, 2004], it is likely that friction at water-saturated conditions of all these minerals increases to some degree with effective pressure.

Rate Dependence

One largely unexplored implication of equation (13.24) is that rate and displacement-dependent changes of strength are possible without dilatancy and changes in area of contact. Fluid layers might be expected to be viscous and therefore rate strengthening; however, structured fluids may have quite anomalous properties [e.g., *Thompson and Robbins*, 1990], and it is difficult to anticipate even the sign of the steady-state rate dependence without some experimental observation. As yet there are no comprehensive studies of the rate dependence of saturated weak faults.

Strength and Rate Dependence of Subduction Zone Minerals

Many measurements of rate dependence of individual mineral constituents found in subduction zones have been made. Localized slip between strong $\mu = 0.65–0.8$) quartzofeldspathic mineral and rock surfaces, for example quartz [*Dieterich and Conrad*, 1984], feldspar (V. J. Scruggs and T. E. Tullis, unpublished data 1997), and granite [*Dieterich*, 1978] are rate weakening and allow for earthquake nucleation.

Basic rocks and minerals as represented by gabbro [*Cox*, 1990; *Tsutsumi and Shimamoto*, 1997] are rate weakening and strong $\mu = 0.7–0.8$).

The data for localized slip between carbonate mineral and rock surfaces are not extensive and are somewhat ambiguous. *Weeks and Tullis* [1985] report relatively high strength ($\mu = 0.5$) rate strengthening for a dolomite. The same laboratory finds that calcite is similarly rate strengthening and somewhat stronger ($\mu = 0.73$) [*Tullis and Weeks*, 1987]. However, *Spetzler et al.* [1991] reports both stable and unstable slip for limestone surfaces. As carbonate is a common cement in accretionary and subduction environments, additional experiments are warranted.

Serpentine has more complicated friction than more approximately isotropic phases. Serpentine can be either weak or strong, rate strengthening or

rate weakening, depending on temperature, pressure, and sliding velocity [*Reinen et al*. 1994; *Moore et al*., 1997]. Chrysotile can be weak ($\mu = 0.2$) at low temperature and pressure except in very dry environments. The other serpentine varieties antigorite and lizardite are stronger ($\mu > 0.4$.) at all conditions, but relatively weak compared to quartzofeldspathic minerals. At low sliding rates, chrysotile serpentines are rate weakening only at high temperatures (>150ºC) and therefore could produce earthquake nucleation near the base of the seismogenic zone [*Moore et al*., 1997]. However, at rates slip rates of around 1×10^{-3} μm/s (31 mm/yr) all serpentines studied are rate neutral or rate strengthening and at corresponding plate motion rates would therefore be a barrier to earthquake nucleation [*Reinen et al*., 1994; *Moore et al*., 1997]. There is virtually no low slip rate data for lizardite and antigorite at crustal conditions however.

Montmorillonite clay may also have complicated strength and rate dependence [e.g., *Saffer et al*., 2001]. Under saturated conditions, montmorillonite can be weak ($\mu = 0.08–0.15$) at low confining pressure [*Logan and Rauenzahn*, 1987; *Morrow et al*., 1992; *Brown et al*. 2003], but under increasing effective stress becomes considerably stronger ($\mu = 0.35$). While *Logan and Rauenzahn* [1987] and *Saffer et al*. [2001] suggest that rate weakening may occur at very low sliding rates (~1×10^{-3} μm/s), at all saturated conditions tested to date, montmorillonite is rate strengthening [*Morrow et al*., 1992; *Brown et al*., 2003].

The sources of illite in laboratory samples are illite-rich shales; these are not pure illite (>90%). Saturated illite /illite-rich shale is somewhat stronger than montmorillonite ($\mu = 0.2–0.45$) [*Morrow et al*., 1992, *Brown et al*., 2003] but is weak relative to quartzofeldspathic rocks. At all saturated conditions tested to date, illite is rate strengthening at temperatures below 400ºC [*Moore et al*., 1989; *Morrow et al*., 1992; *Brown et al*., 2003].

Friction in Polyphase Fault Zones

That accretionary sediments, often involved in shallow faulting and underthrusting in subduction zones, have mineral components with widely varying frictional strength (e.g., quartz and smectite) requires that the friction of polyphase aggregates be considered. Continuum rheology of polyphase components is well studied [e.g., *Tullis et al*., 1991, and references therein], however, because friction is controlled by processes operating at contacts between grains, mixing relationships from standard rheological studies are not directly applicable. For friction that is controlled in part by intergranular water films, the polyphase boundary may have strength that is different from the single-phase boundaries of either component.

Basic aspects of polyphase friction can be considered using a single roughly planar surface between two arrays of grains as the locus of all deformation (fig. 13.34a). There are two phases present. The resistance to shearing is the sum of the resistance of each contact to shear. There are three types of contacts, two different single-phase boundaries and interphase boundaries. The macroscopic shear strength is

$$\tau = P_{11}\tau^{11} + P_{22}\tau^{22} + P_{12}\tau^{12} \tag{13.25a}$$

where τ^{11}, τ^{22}, and τ^{12} are the strengths of a single-phase boundary between phase 1, a single-phase boundary between phase 2, and an interphase boundary, respectively. The coefficients P_{11}, P_{22}, and P_{12} are the corresponding fractions of each boundary type present. For a fully localized shear boundary whose composition is the same of the entire gouge layer, the fractions are known as a function of composition; they are the probabilities

$$\begin{aligned} P_{11} &= \frac{\binom{K}{0}\binom{M-K}{2}}{\binom{M}{2}} \\ P_{22} &= \frac{\binom{K}{2}\binom{M-K}{0}}{\binom{M}{2}} \\ P_{12} &= \frac{\binom{K}{2}\binom{M-K}{0}}{\binom{M}{2}} \end{aligned} \tag{13.25b}$$

where M is the number of grains in the boundary, K is the number of grains of phase 1, and the probability notation used is defined by

$$\binom{i}{j} = \frac{i!}{(i-j)!\,j!} \tag{13.25c}$$

Figure 13.34b shows the coefficients P as a function of composition. At a composition of 50%, half of the grain boundaries are interphase boundaries. It is possible to have enhanced weakening owing to a weak interphase boundary, for example $\tau^{11} = 0.7$, $\tau^{22} = 0.2$, and $\tau^{12} = 0.2$ (fig. 13.34c). Similar behavior is seen in analog experiments where wet interphase boundaries induce dissolution effects not present at single-phase boundaries [*Bos and Spiers*, 2001]. Mixing also implies mixed rate dependence, which can be analyzed using a similar approach to that used for strength above. The very limited work on mixtures to date by *Logan and Rauenzahn* [1987], *Brown et al*. [2003], and *Saffer and Marone* [2003] suggest that interphase boundaries between quartz and clay have intermediate strength (fig. 13.34d). It is also possible that mixed clays have anomalous strengths, either stronger or weaker than linear combinations

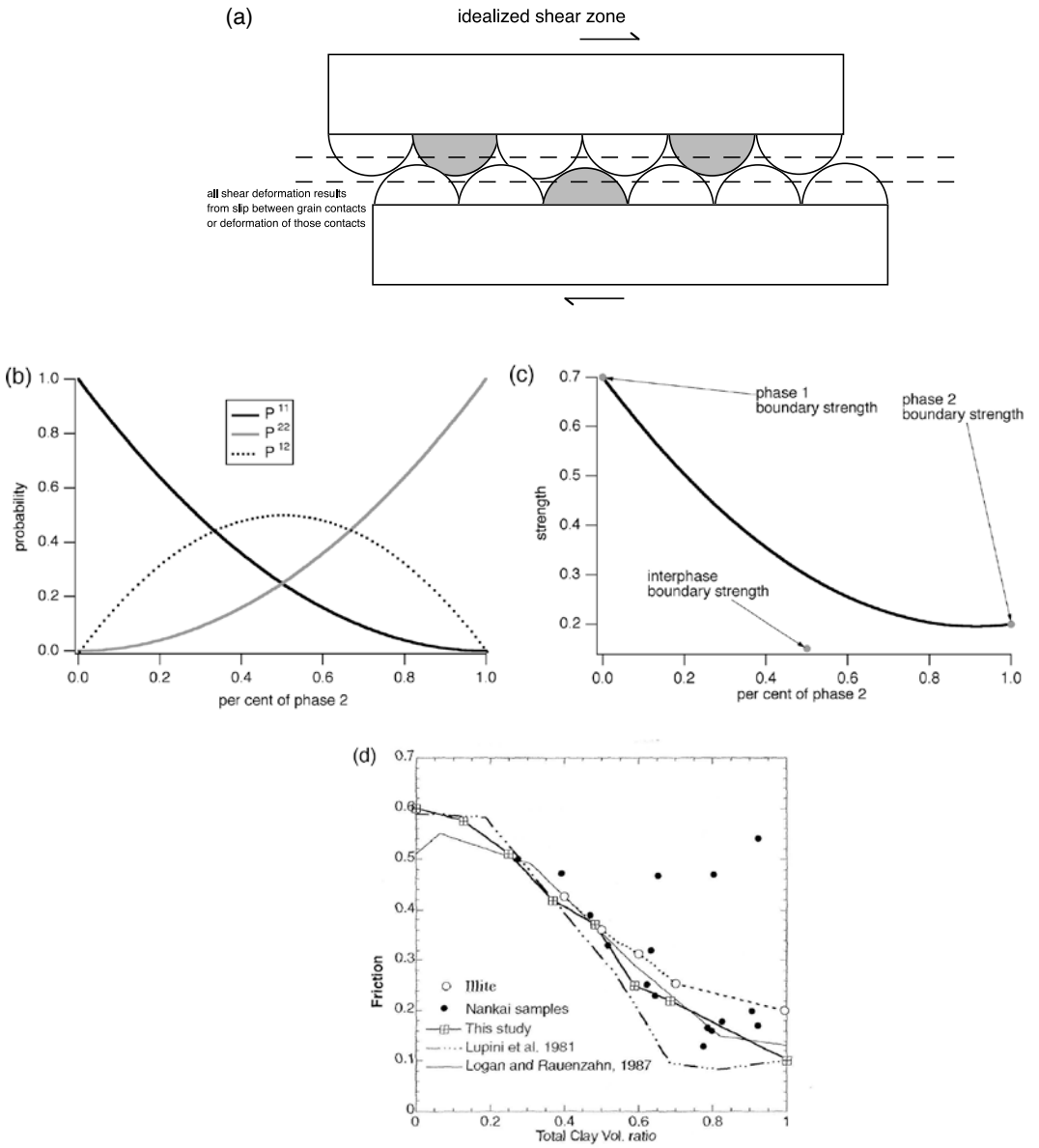

Figure 13.34 Simple model of strength of two-phase granular material. (a) The model is a fully localized slip on a surface composed of particles whose relative numbers reflect the overall composition. (b) The number of phase 1, phase 2, and interphase contacts as a function of percent phase 2. (c) Example strength with variation in percent phase 2. Here the phase 1 contact strength is $\mu = 0.7$ (quartz), the phase 2 contact strength is $\mu = 0.2$ (smectite), and the interphase boundary is anomalously weak $\mu = 0.15$. (d) Variation of mixed clay–quartz samples with clay content. Reprinted from Earth and Planetary Science Letters, 214, *Brown, Kopf, Underwood, and Weinberger*, Compositional and fluid pressure controls on the state of stress on the Nankai subduction thrust, 589–603, Copyright (2003), with permission from Elsevier.

of the constituents, and as strengths are related to water adhesion, water pH, and ionic properties may come into play.

Summary

Strength loss during failure of dry intact rock occurs when deformation is accompanied by dilatancy and an associated loss of contacting area across the incipient fault. Dilatancy is also the source of the pressure dependence of rock failure strength, the observation that as confining pressure is increased the failure strength increases. As confining pressure is increased, dilatancy is suppressed so more shear stress is required to dilate the rock to the point of failure. The primary differences between intrinsically strong and intrinsically weak rocks are that intrinsically weak rocks have low dilatancy and have small strength losses associated with fault formation. Intrinsic weakness results from the presence of weak, anisotropic minerals that slip on cleavage surfaces and a preferential orientation of the weak minerals within the stress field.

The basic observations stated above also apply to dry slip on preexisting faults: failure strength is pressure dependent, rapid slip and strength loss are accompanied by dilatancy and loss of contacting area across the fault, and intrinsic weakness is due to the presence and preferential alignment of weak minerals. Because strength loss during rapid slip is a result of dilatancy, it is expected that small strength losses are associated with the rapid slip of preexisting intrinsically weak faults. This expected correlation between failure strength and strength loss implies that for laboratory-based rate and state friction relationships there is proportionality between the coefficient of the rate weakening term (b) and the nominal strength (μ_0).

As applied to earthquake occurrence, the theory of slip instability requires that fault strength loss ($\Delta\tau$) with slip (δ) is larger than the elastic stiffness (k) of the surroundings, defining a critical stiffness (k_c), such that for instability $\Delta\tau/\delta > k_c$. As dry intrinsically weak rocks and faults have low strength loss, instability is less likely in weak materials. The presence of undrained pore fluid at pressure p affects sliding stability in two ways. First, the effective normal stress is lower, making the strength loss proportionally lower, which favors aseismic over seismic slip. Second, shear induces dilatancy, which reduces the local pore pressure making the fault strong. This dilatancy hardening prevents slip instability, again promoting aseismic over seismic slip. The principal conclusion of this review of laboratory observations of dry and saturated faulting is that in the absence of chemical effects of fluids on fault strength, both intrinsic weakness and apparent weakness resulting from high pore pressure tend to encourage aseismic over seismic slip.

However, the sliding stability of intrinsically weak rocks and minerals is not well studied. The effect of high pore pressure on sliding stability has only been considered for an intrinsically strong, highly dilatant, apparently weak fault. Since many weak phases found in subduction zones have low dilatancy, the effect of high pore pressure on sliding stability is presently unknown. In

addition, chemical effects on fault strength are not well studied to date. Many weak phases have strengths that are sensitive to the chemical environment, in particular clays and other sheet silicate minerals have strengths that are influenced by the presence of water. The role of such effects in seismogenesis is not known at present. Given the present state of knowledge, sliding stability and fault strength cannot be unequivocally related.

Acknowledgments

Some results presented here are from unpublished collaborations with Terry Tullis, David Lockner, T.-F. Wong, and Joan Gomberg. Long-standing discussion and correspondence with D. Lockner, T. Tullis, J. D. Weeks, T.-F. Wong, M. Nakatani, G. Hirth, D. Goldsby, J. Dieterich, C. Marone, L. Reinen, and M. Blanpied are gratefully acknowledged. A. Kronenberg provided unpublished data from studies of talc single crystals and shale. I was fortunate to be associated with D. Moore, L. Reinen, C. Morrow, and G. Hirth during periods when each were considering low temperature deformation of weak minerals. Masao Nakatani reviewed and made corrections to the analysis of contact-scale deformation leading to comparisons between the rate dependencies of friction, crack growth and dislocation glide. Thanks to Harold Tobin and Casey Moore for the opportunity to contribute to the SEIZE and MARGINS initiatives, and to T. Dixon, G. Hirth, S. Karner and C. Marone for comments on the manuscript.

This review was supported by the Southern California Earthquake Center. SCEC is funded by NSF Cooperative Agreement EAR–0106924 and USGS Cooperative Agreement 02HQAG0008. The SCEC contribution number for this paper is 1021.

References

Anderson, E. M. (1951), *The Dynamics of Faulting and Dyke Formation With Application to Britain*, 206 pp., Oliver and Boyd, Edinburgh, U.K.

Andrews, D. J. (1976), Rupture velocity of plane strain shear cracks, *J. Geophys. Res., 81*, 5679–5687.

Ashby, M. F., and C. G. Sammis (1990), The damage mechanics of brittle solids in compression, *Pure Appl. Geophys., 133*(3), 489–521.

Atkinson, B. K. (1984), Subcritical crack growth in geologic materials, *J. Geophys. Res., 89*, 4077–4114.

Atkinson, B. K., and P. G. Meredith (1987a), The theory of subcritical crack growth with applications to minerals and rocks, in *Fracture Mechanics of Rock*, *Geol. Ser.*, edited by B. K. Atkinson, pp. 111–166, Elsevier, New York.

Atkinson, B. K., and P. G. Meredith (1987b), Experimental fracture mechanics data for rocks and minerals, in *Fracture Mechanics of Rock*, *Geol. Ser.*, edited by B. K. Atkinson, pp. 477–525, Elsevier, New York.

Bailey, A. I., and J. S. Courtney-Pratt (1955), The area of real contact and the shear strength of monomolecular layers of a boundary lubricant, *Proc. R. Soc., Ser. A, 227*, 500–515.

Beeler, N. M., T. E. Tullis, and J. D. Weeks (1994), The roles of time and displacement in the evolution effect in rock friction, *Geophys. Res. Lett., 21* 1987–1990.

Beeler, N. M., and T. E. Tullis (1997), The roles of displacement in velocity dependent volumetric strain of fault zones, *J. Geophys. Res., 102*, 22,595–22,609.

Beeler, N. M., T. E. Tullis, M. L. Blanpied, and J. D. Weeks (1996), Frictional behavior of large displacement experimental faults, *J. Geophys. Res., 101*, 8697–8715.
Bernabe, Y. and W. F. Brace (1990), Deformation and fracture of berea sandstone, in *The Brittle-Ductile Transition in Rocks*, *Geophys. Monogr. Ser.,* vol. 56, edited by A. G. Duba et al., pp. 91–101, AGU, Washington, D. C.
Berthoud, P., T. Baumberger, C. G'Seil, and J.-M. Hiver (1999), Physical analysis of the state- and rate-dependent friction law: Static friction, *Phys. Rev. B., 59*, 14,313–14,327.
Biegel, R. L., C. G. Sammis, and J. H. Dieterich (1989), The frictional properties of a simulated gouge having a fractal particle distribution, *J. Struct. Geol., 11*, 827–846.
Bish, D. L., and R. F. Giese (1981), Interlayer boding in IIb chlorite, *Am. Mineral., 66*, 1216–1220.
Blanpied, M. L., D. A. Lockner, and J. D. Byerlee (1991), Fault stability inferred from granite sliding experiments at hydrothermal conditions, *Geophys. Res. Lett., 18*(4), 609–612.
Blanpied, M. L., C. J. Marone, D. A. Lockner, J. D. Byerlee, and D. P. King (1998), Quantitative measure of the variation in fault rheology due to fluid-rock interactions, *J. Geophys. Res., 103*, 9691–9712.
Boettcher, M. S., and T. H. Jordan (2004), Earthquake scaling relations for mid-ocean ridge transform faults, *J. Geophys. Res., 109*, B12302, doi:10.1029/2005JB003753.
Bos, B., and C. J. Spiers (2001), Experimental investigation into the microstructural and mechanical evolution of phyllosilicate-bearing fault rock under conditions favoring pressure solution, *J. Struct. Geol., 23*, 1187–1202.
Bowden, F. P., and D. Tabor (1950), *The Friction and Lubrication of Solids*, 374 pp., Oxford Univ. Press, New York.
Brace, W. F., and J. D. Byerlee (1966), Stick-slip as a mechanism for earthquakes, *Science, 153*, 990–992.
Brace, W. F. (1978), Volume changes during fracture and frictional sliding, *Pure Appl. Geophys., 116*, 603–614.
Brace, W. F., and D. L. Kohlstedt (1980), Limits on lithospheric stress imposed by laboratory experiments, *J. Geophys. Res., 85*, 6248–6252.
Brace, W. F., B. W. Paulding, and C. H. Scholz (1966), Dilatancy in the fracture of crystalline rock, *J. Geophys. Res., 71*, 3939–3953.
Brown, K. M., A. Kopf, M. B. Underwood, and J. L. Weinberger (2003), Compositional and fluid pressure controls on the state of stress on the Nankai subduction thrust, *Earth Planet. Sci. Lett., 214*, 589–603.
Brown, S. R., and C. H. Scholz (1985), The closure of random elastic surfaces in contact, *J. Geophys. Res., 90*, 5531–5545.
Byerlee, J. D. (1967). Frictional characteristics of granite under high confining pressure, *J. Geophys. Res., 72*, 3639–3648.
Byerlee, J. D. (1968), Brittle-ductile transition in rocks, *J. Geophys. Res., 73*, 4741–4750.
Byerlee, J. D., (1970), The mechanics of stick-slip, *Tectonophysics, 9*, 475–486.
Byerlee, J. D. (1978), Friction of rocks, *Pure Appl. Geophys., 116*, 615–626.
Byerlee, J. D., and R. Summers (1976), A note on the effect of fault gouge thickness on fault stability, *Int. J. Rock Mech. Min. Sci., 13*, 35–36.
Byrne, D. E., D. M. Davis, and L. R. Sykes (1988), Loci and maximum size of thrust earthquakes and the mechanics of the shallow region of subduction zones, *Tectonophysics, 7*, 833–857.
Charles, R. J., and W. B. Hillig (1962), The kinetics of glass failure by stress corrosion, in *Symposium sur la Resistance due Verre et les Moyens de l'ameliorer, Union Scientific Continentale du Verr, Charleroi, Belgium*, pp. 511–527, Union Sciences Continentale du Verre, Charleroi, Belgium.
Chester, F. M. (1994), Effects of temperature on friction: Constitutive equations and experiments with quartz gouge, *J. Geophys. Res., 99*, 7247–7262.
Costin, L. S. (1987), Deformation and failure, in *Fracture Mechanics of Rock*, edited by B. K. Atkinson, pp. 167–215, Elsevier, New York.
Cox, S. J. D. (1990), Velocity-dependent friction in a large direct shear experiment on gabbro, in *Deformation Mechanisms, Rheology and Tectonics*, *Spec. Publ. Geol. Soc., 54*, 63–70.

Das, S., and C. H. Scholz (1981), Theory of time-dependent rupture in the Earth, *J. Geophys. Res., 86*, 6039–6051.
Dieterich, J. H. (1972), Time-dependent friction in rocks, *J. Geophys. Res., 77*, 3690–3697.
Dieterich, J. H. (1978a), Mechanics of earthquake faulting, in *Summaries of Technical Reports, U.S. Geological Survey National Earthquake Hazards Reduction Program*, edited by J. Evernden, pp. 328–329, U.S. Geol. Surv., Boulder, Colo.
Dieterich, J. H. (1978b), Time-dependent friction and the mechanics of stick slip, *Pure Appl. Geophys., 116*, 790–806.
Dieterich, J. H. (1979), Modeling of rock friction: 1. Experimental results and constitutive equations, *J. Geophys. Res., 84*, 2161–2168.
Dieterich, J. H. (1981), Constitutive properties of faults with simulated gouge, in mechanical Behavior of Crustal Rocks, edited by N. L. Carter, M. Friedman, J. M. Logan, and D. W. Stearns, *Geophys. Monor. Ser., 24,* AGU, Washington, D. C. 103–120.
Dieterich, J. H. (1992). Earthquake nucleation on faults with rate- and state-dependent strength, in *Earthquake Source Physics and Earthquake Precursors*, edited by T. Mikumo et al., pp. 115–134, Elsevier, New York.
Dieterich, J. H., and G. A., Conrad (1984). Effect of humidity on time- and velocity-dependent friction in rocks, *J. Geophys. Res., 89*, 4196–4202.
Dieterich, J. H., and B. D. Kilgore (1994), Direct observation of frictional contacts: New insights for state-dependent properties, *Pure and Applied Geophys., 143*, 283–302.
Dieterich, J. H., and B. Kilgore (1996), Implications of fault constitutive properties for earthquake prediction, *Proc. Natl. Acad., Sci. U. S. A., 93*, 3787–3794.
Dieterich, J. H., and B. D. Kilgore (1994), Direct observation of frictional contacts: New insights for state-dependent properties, *Pure Appl. Geophys., 143*, 283–302.
Dieterich, J. H., and M. F. Linker (1992), Fault stability under conditions of variable normal stress, *Geophys. Res. Lett., 19*, 1691–1694.
Dokos, S. J. (1946), Sliding friction under extreme pressures, *J. Appl. Mech., 13A*, 148–156.
Donath, F. A. (1961), Experimental study of shear failure in anisotropic rocks, *Bull. Geol. Soc. Am., 72*, 985–900.
Du, Y., and A. Aydin (1991), Interaction of multiple cracks and formation of echelon crack arrays, *Int. J. Numer. Anal. Methods Geomech., 15*, 205–218.
Eckhardt, M. M, B. Evans, and S. Viswanathan (1996), Microstructural damage due to frictional sliding in calcite, *Eos, Trans. AGU, 77*, Fall Meet. Suppl., F696.
Engelder, J. T., and C. H. Scholz (1976), The role of asperity indentation and ploughing in rock friction, II, Influence of relative hardness and normal load, *Int. J. Rock Mech. Sci. Geomech. Abstr. 13*, 155–163.
Escartin, J., G. Hirth, and B. Evans (1997), Nondilatant brittle deformation of serpentinites; implications for Mohr-Coulomb theory and the strength of faults, *J. Geophys. Res., 102*, 2897–2913.
Evans, B. (1984), The effect of temperature and impurity content on indentation hardness of quartz, *J. Geophys. Res., 89*, 4213–4222.
Evans, B., and C. Goetze (1979), The temperature variation of hardness of olivine and its implication for polycrystalline yield stress, *J. Geophys. Res., 84*, 5505–5524.
Evans, B., J. T. Fredrich, and T.-F. Wong (1990), The brittle-ductile transition in rocks: Recent experimental and theoretical progress, in *The Brittle-Ductile Transition in Rocks, Geophys. Monogr. Ser.,* vol. 56, edited by A. G. Duba et al., pp. 1–21, AGU, Washington, D. C.
Frank, F. C. (1965), On dilatancy in relation to seismic sources, *Rev. Geophys., 3*, 485–503.
Friedman, M., J. Handin, and G. Alani (1972), Fracture surface energy of rocks, *Int. J. Rock Mech. Min. Sci., 9*, 757–766.
Frolich, C. (1989), The nature of deep-focus earthquakes, *Annu. Rev. Earth Planet. Sci., 17*, 227–254.
Frye, K. M., and C. Marone (2002), Effect of humidity on granular friction at room temperature, *J. Geophys. Res., 107*(B11), 2309, doi:10.1029/2001JB000654.
Furumoto, A. S. (1991), Source parameters of destructive tsunamis, *Sci. Tsunami Hazards, 9*, 95–113.

Giese, R. F. (1978), The electrostatic interlayer forces of layer structure minerals, *Clays Clay Miner., 26*, 51–57.
Giese, R. F. (1980), Hydroxyl orientations and interlayer bonding in amesite, *Clays Clay Miner., 28*, 81–86.
Goldsby, D. L., A. Rar, G. M. Pharr, and T. E. Tullis (2004), Nanoindentation creep of quartz, with implications for rate-and state-variable friction laws relevant to earthquake mechanics, *J. Mater. Res., 19*, 357–365.
Goetze, C., and B. Evans (1979), Stress and temperature in the bending lithosphere as constrained by experimental rock mechanics, *Geophys. J. R. Astron. Soc., 59*, 463–478.
Greenwood, J. A., and J. Williamson (1966), Contact of nominally flat surfaces, *Proc. R. Soc. London, Ser. A, 295*, 300–319.
Griffith, A. A., (1920), The phenomena of rupture and flow in solids, *Philos., Trans. R. Soc. London, Ser. A 221*, 163–198.
Griggs, D. (1936), Deformation of rocks under high confining pressure, *J. Geol., 44*, 541–577.
Gu, J., J. R. Rice, A. L. Ruina, and S. Tse (1984), Stability of frictional slip for a single degree of freedom elastic system with non-linear rate and state dependent friction, *J. Mech. Phys. Solids, 32*, 167–196.
Gu, Y., and T.-F. Wong (1991), Effects of loading velocity, stiffness and inertia on the dynamics of a single degree of freedom spring-slider system, *J. Geophys. Res., 96*, 21,677–21,691.
Hirata, T. (1987), Omori's power law aftershock sequences of microfracturing in rock fracture experiment, *J. Geophys. Res.*, 6215–6221.
Horii, H., and S. Nemat-Nasser (1986), Brittle failure in compression: splitting, faulting and brittle-ductile transition, *Philos. Trans. R. Soc. London, Ser. A, 319*, 337–374.
Hubbert, M. K., and W. W. Rubey (1959), Role of fluid pressure in mechanics of overthrust faulting, *Bull. Geol. Soc. Am., 70*, 115–166.
Ibanez, W. D., and A. K. Kronenberg (1993), Experimental deformation of shale: Mechanical properties and microstructural indicators of mechanisms, *Int. J. Rock Mech. Min. Sci., 30*, 723–734.
Ida, Y. (1972), Cohesive force across the tip of a longitudinal shear crack and Griffith's specific surface energy, *J. Geophys. Res., 77*, 3796–3805.
Ida, Y., (1973), The maximum acceleration of seismic ground motion, *Bull. Seismol. Soc. Am. , 63,* 959–968.
Israelachvili, J. N. (1992), Adhesion forces between surfaces in liquids and condensable vapours, *Surface Sci. Rep., 14*, 109–160.
Israelachvili, J. N., and G. E. Adams (1976), Direct measurement of long range forces between two mica surfaces in aqueous KNO_3 solutions, *Nature, 262*, 774–776.
Israelachvili, J. N., P. M. McGuiggan, and A. M. Homola (1988), Dynamic properties of molecularly thin liquid films, *Science, 240*, 189–191.
Jaoul, O., J. Tullis, and A. Kronenberg (1984), The effect of varying water contents on the creep behavior of Heavitree quartzite, *J. Geophys. Res., 89*, 4298–4312.
Johnson, T. (1981), Time dependent friction of granite: Implications for precursory slip on faults, *J. Geophys. Res., 86*, 6017–6028.
Kailer, A., K. G. Nickel, and Y. G. Gogotsi (1999), Raman microspectroscopy of nanocrystalline and amorphous phases in hardness indentations, *J. Raman Spectrosc., 30*, 939–946.
Karner, S. L., and C. J. Marone (1998), The effect of shear load on frictional healing in simulated fault gouge, *Geophys. Res. Lett., 25*, 4561–4564.
Kato, N., K. Yamamoto, H. Yamamoto, and T. Hirasawa (1992), Strain-rate effect on frictional strength and the slip nucleation process, *Tectonophysics, 211*, 269–282.
Kelleher, J., J. Savino, H. Rowlett, and W. McCann (1974), Why and where great thrust earthquakes occur along island arcs, *J. Geophys. Res., 79*, 4889–4899.
Kemeny, J. M., and N. G. W. Cook (1987), Crack models for the failure of rocks in compression, in *Constitutive Laws for Engineering Materials: Theory and Applications*, edited by C. S. Desai, pp. 878–887, Elsevier, New York.
Kirby, S. H. (1980), Tectonic stresses in the lithosphere: Constraints provided by the experimental deformation of rocks, *J. Geophys. Res., 85*, 6353–6363.

Knopoff, L. (1972), Model of aftershock occurrence, in *Flow and Fracture of Rocks*, *Geophys. Monogr. Ser.*, vol. 16, edited by H. C. Heard et al., pp. 259–263, AGU, Washington, D. C.
Kranz, R. L. (1980), The effects of confining pressure and stress difference on static fatigue of granite, *J. Geophys. Res., 85*., 1854–1866.
Kronenberg, A. K., S. H. Kirby, and J. C. Pinkston (1990), Basal slip and mechanical anisotropy of biotite, *J. Geophys., Res., 95*, 19,257–19,278.
Lawn, B. (1993), *Fracture of Brittle Solids*, 378 pp., Cambridge Univ. Press, New York.
Linker, M. F., and J. H. Dieterich (1992), Effects of variable normal stress on rock friction: Observations and constitutive equations, *J. Geophys. Res., 97*, 4923–4940.
Lockner, D. A. (1998), A generalized law for brittle deformation of Westerly granite, *J. Geophys. Res., 103*, 5107–5123.
Lockner, D. A., and J. D. Byerlee (1990), An example of slip instability resulting from displacement-varying strength, *Pure Appl. Geophys., 133*, 398–410.
Lockner, D. A., J. D. Byerlee, V. Kuksenko, A. Ponomarev, and A. Sidorin (1991), Quasi-static fault growth and shear fracture energy in granite, *Nature, 350*, 39–42.
Lockner, D. A., D. E. Moore, and Z. Reches (1992), Microcrack interaction leading to shear fracture, in *33rd U.S. Rock Mechanics Symposium*, edited by J. R. Tillerson and W. R. Wawersik, pp. 807–816, A. A. Balkema, Brookfield, VT.
Logan, J. M., and K. A. Rauenzahn (1987), Frictional dependence of gouge mixtures of quartz and montmorillonite on velocity, composition and fabric, *Tectonophysics, 144*, 87–108.
Mair, K., and C. Marone (1999), Friction of simulated fault gouge for a wide range of velocities and normal stresses, *J. Geophys. Res., 137*, 28,899–28,914.
Marcellini, A. (1995), Arrhenius behavior of aftershock sequences, *J. Geophys. Res., 100*, 6463–6468.
Marcellini, A. (1997), Physical model of aftershock temporal behavior, *Tectonophysics, 277*, 137–146.
Mares, V. M., and A. K. Kronenberg (1993), Experimental deformation of muscovite, *J. Struct. Geol., 15*, 1061–1075.
Marone, C. J. (1998), Laboratory-derived friction laws and their application to seismic faulting, *Annu. Rev. Earth Planet. Sci., 26*, 643–696.
Marone, C., and B. Kilgore (1993), Scaling of the critical slip distance for seismic faulting with shear strain in fault zones, *Nature, 362*, 618–621.
Marone, C., C. B. Raleigh, and C. H. Scholz (1990), Frictional behavior and constitutive modeling of simulated fault gouge, *J. Geophys. Res., 95*, 7007–7025.
Masuda, T., T. Hiraga, H. Ikei, H. Kanda, Y. Kugimiya, and M. Akizuki (2000), Plastic deformation of quartz at room temperature: A Vickers nano-indentation test, *Geophys. Res. Lett., 27*, 2773–2776.
Mogi, K. (1962), Study of elastic shocks caused by the fracture of heterogeneous materials and their relation to earthquake phenomenon, *Bull. Earthquake Res. Inst. Univ. Tokyo, 40*, 1438.
Mogi, K. (1974), On the pressure dependence of strength of rocks and the Coulomb fracture criterion, *Tectonophysics, 21*, 273–285.
Moore, D., and D. A. Lockner (2004), Crystallographic controls on the frictional behavior of dry and water-saturated sheet structure minerals, *J. Geophys. Res., 109*, B03401, doi:10.1029/2003JB002582.
Moore, D. E., and D. A. Lockner (2007), Friction of the smectite clay montmorillonite: A review and interpretation of data, this volume.
Moore, D. E., R. Summers, and J. D. Byerlee (1989), Sliding behavior and deformation textures of heated illite gouge, *J. Struct. Geol., 11*, 329–342.
Moore, D. E., D. A. Lockner, R. Summers, M. Shengli, and J. D. Byerlee (1996), Strength of chrysotile-serpentinite gouge under hydrothermal conditions: Can it explain a weak San Andreas fault?, *Geology, 24*(11), 1041–1044.
Moore, D. E., D. A. Lockner, S. Ma, R. Summers, and J. D. Byerlee (1997), Strengths of serpentinite gouges at elevated temperatures, *J. Geophys. Res., 102*, 14,787–14,801.
Moore, J. C., and R. von Huene (1980), Abnormal pore pressure and hole instability in forearc regions, preliminary report, p. 29, Ocean Margin Drill. Proj., Menlo Park, Calif.

Moore, J. C., and D. Saffer (2001), Updip limit of the seismogenic zone beneath the accretionary prism of southwest Japan: An effect of diagenetic to low-grade metamorphic processes and increasing effective stress, *Geology, 29*(2), 183–186.
Morrow, C., and J. Byerlee (1989), Experimental studies of compaction and dilatancy during frictional sliding on faults containing gouge, *J. Struct. Geol., 11*, 815–825.
Morrow, C. A., Radney, B, and J. D. Byerlee (1992), Frictional strength and the effective pressure law of montmorillonite and illite clays, in *Fault Mechanics and Transport Properties of Rocks*, pp. 69–88, Elsevier, New York.
Morrow, C. A., D. E. Moore, and D. A. Lockner (2000), The effect of mineral bond strength and adsorbed water on fault gouge frictional strength, *Geophys. Res. Lett, 27*, 815–818.
Nakatani, M. (2001), Conceptual and physical clarification of rate and state friction: Frictional sliding as a thermally activated rheology, *J. Geophys. Res., 106*, 13,347–13,380.
Nakatani, M., and H. Mochizuki (1996), Effects of shear stress applied to surfaces in stationary contact on rock friction, *Geophys. Res. Lett., 23*, 869–872.
Okubo, P. G., and J. H. Dieterich (1981), Fracture energy of stick-slip events in a large scale biaxial experiment, *Geophys. Res. Lett., 8*, 887–890.
Palmer, A. C., and J. R. Rice (1973), The growth of slip surfaces in the progressive failure of over-consolidated clay, *Proc. R. Soc. London, Ser. A, 332*, 527–548.
Peng, S., and A. M. Johnson (1972), Crack growth and faulting in cylindrical specimens of Chelmsford granite, *Int. J. Rock Mech. Min. Sci. Geomech. Abstr., 9*, 37–86.
Peterson, E. T., and T. Seno (1984), Factors affecting seismic moment release rates in subduction zones, *J. Geophys. Res, 89*, 10,233–10,248.
Power, W. L., T. E. Tullis, and J. D. Weeks (1988), Roughness and wear during brittle faulting, *J. Geophys. Res., 93*, 15,268–15,278.
Rabinowicz, E. (1958), The intrinsic variables affecting the stick-slip process, *Proc. Phys. Soc. London, 71*, 668–675.
Raleigh, C. B., and M. S. Paterson (1965), Experimental deformation of serpentinite and its tectonic implications, *J. Geophys. Res., 70*, 3965–3985.
Reches, Z., and D. A. Lockner (1994), Nucleation and growth of faults in brittle rocks, *J. Geophys. Res., 99*, 18,159–18,173.
Reuschle, T. (1990), Slow crack growth and aftershock sequences, *Geophys. Res. Lett., 17*, 1525–1528.
Rice, J. R. (1975), On the stability of dilatant hardening for saturated rock masses, *J. Geophys. Res., 80*, 1531–1536.
Rice, J. R. (1980), The mechanics of earthquake rupture, in *Physics of the Earth's Interior*, edited by A. M. Dziewonski and E. Boschi, pp. 555–649, Elsevier, New York.
Rice, J. R. (1983), Constitutive relations for fault slip and earthquake instabilities, *Pure Appl. Geophys., 121*, 443–475.
Rice, J. R. (1993), Spatio-temporal complexity of slip on a fault, *J. Geophys. Res., 98*, 9885–9907.
Rice, J. R., and A. L. Ruina (1983), Stability of steady frictional slipping, *J. Appl. Mech., 50*, 343–349.
Rice, J. R., N. Lapusta, and K. Ranjith (2001), Rate and state dependent friction an the stability of sliding between elastically deformable solids, *J. Mech. Phys. Sol., 49*, 1865–1898.
Reinen, L. A., J. D. Weeks, and T. E. Tullis (1994), The frictional behavior of lizardite and antigorite serpentinites: Experiments, constitutive models, and implications for natural faults, *Pure Appl. Geophys., 143*, 317–358.
Robertson, E. C. (1983), Relationship of fault displacement to gouge and breccia thickness, *Trans. Am. Inst. Min. Metall. Pet. Eng., 35*, 1426–1432.
Rudnicki, J. W., and C.-H. Chen (1988), Stabilization of rapid frictional slip on a weakening fault by dilatant hardening, *J. Geophys. Res., 93*, 4745–4757.
Ruina, A. L. (1983), Slip instability and state variable friction laws, *J. Geophys. Res., 88*, 10,359–10,370.
Rutter, E. H. (1974), The influence of temperature, strain rate and interstitial water in the experimental deformation of calcite rocks, *Tectonophysics, 22*, 311–334.
Rutter, E. H. (1983), Pressure solution in nature, theory, and experiment, *J. Geol. Soc. London, I40*, 725–740.

Saffer, D. M., and B. A. Bekins (2002), Hydrologic controls on the morphology and mechanics of accretionary wedges, *Geology, 30*(3), 271–274.
Saffer, D. M., and C. Marone (2003), Comparison of smectite- and illite-rich gouge frictional properties: Application to the updip limit of the seismogenic zone along subduction zone megathrusts, *Earth Planet. Sci. Let., 215*, 219–235.
Saffer, D. M., K. M. Frye, C. Marone, and K. Mair (2001), Laboratory results indicating complex and potentially unstable frictional behavior of smectite clay, *Geophys. Res. Lett., 28*, 2297–2300.
Sammis, C. G., and M. F. Ashby (1986), The failure of brittle porous solids under compressive stress states, *Acta Metall., 34*, 511–526.
Savage, J. C., J. D. Byerlee, and D. A. Lockner (1996), Is internal friction, friction?, *Geophys. Res. Lett., 23*, 487–490.
Scholz, C. (1968a), The frequency magnitude relation of microfracturing in rock and its relation to earthquakes, *Bull. Seismol. Soc. Am., 58*, 399–415.
Scholz, C. (1968b), Microfractures, aftershocks and seismicity, *Bull. Seismol. Soc. Am., 58*, 117–130.
Scholz, C. H. (1968c), Mechanism of creep in brittle rock, *J. Geophys. Res., 73*, 3295–3302.
Scholz, C. H. (1972), Static fatigue in quartz, *J. Geophys. Res., 77*, 2104–2114.
Scholz, C. H. (1988), The critical slip distance for seismic faulting, *Nature, 336*, 761–763.
Scholz, C. H. (1990), *The Mechanics of Earthquakes and Faulting*, 439 pp., Cambridge Univ. Press, New York.
Scholz, C. H., and J. T. Engelder (1976), The role of asperity indentation and ploughing in rock friction, I, Asperity creep and stick-slip, *Int. J. Rock Mech. Sci. Geomech. Abstr., 13*, 149–154.
Scruggs, V. J. (1997), Frictional constitutive properties and related microstructures of albite, muscovite, biotite and talc, Ph.D. dissertation, Brown Univ., Providence, R. I.
Scruggs, V. J., and T. E. Tullis (1998), Correlation between velocity dependence of friction and strain localization in large displacement experiments on feldspar, muscovite and biotite gouge, *Tectonophysics, 295*, 15–40.
Segall, P., and J. R. Rice (1995), Dilatancy, compaction, and slip instability of a fluid infiltrated fault, *J. Geophys. Res., 100*, 22,155–22,173.
Sharp, S. J., M. F. Ashby, and N. A. Fleck (1993), Material response under static and sliding indentation loads, *Acta Metall. Mater., 41*, 685–692.
Shea, W. T., and A. K. Kronenberg (1992), Rheology and deformation mechanisms of an isotropic mica schist, *J. Geophys. Res., 97*, 15,201–15,237.
Shea, W. T., and A. K. Kronenberg (1993), Strength and anisotropy of foliated rocks with varied mica content, *J. Struct. Geol., 15*, 1097–1121.
Sibson, R. H. (2002), Geology of the crustal earthquake source, in *International Handbook of Earthquake and Engineering Seismology*, edited by W. H. K. Lee, H. Kanamori, and P. C. Jennings, Elsevier, New York, 455–473.
Spetzler, H., G. Sobolev, A. Koltsov, A. Zang, and I. C. Getting (1991), Some properties of unstable slip on rough surfaces, *Pure Appl. Geophys. 137*, 95–112.
Stesky, R. M. (1978), Mechanisms of high temperature frictional sliding in Westerly granite, *Can. J. Earth Sci., 15*, 361–375.
Stuart, W. D. (1988), Forecast model for great earthquakes at the Nankai trough subduction zone, *Pure Appl. Geophys. 126*, 619–641.
Tapponnier, P., and W.F. Brace (1976), Development of stress-induced microcracks in Westerly granite, *Int. J. Rock Mech. Min. Sci. Geomech. Abstr., 13*, 103–112.
Terzaghi, K. V. (1923), Die berechnung der durchlassigkeitsziffer des tones asu dem verlauf der hydrodynamischen spannumgserscheinungen, *Sber. Akad. Wiss. Wien, 132*, 105.
Thomas, P. A., and M. O. Robbins (1990), Origin of stick-slip motion in boundary lubrication, *Science, 250*, 792–794.
Tse, S. T., and J. R. Rice (1986), Crustal earthquake instability in relation to the depth variation for frictional slip properties, *J. Geophys. Res., 91*, 9452–9472.
Tsutsumi, A., and T. Shimamoto (1997), High-velocity frictional properties of gabbro, *Geophys. Res. Lett., 24*, 699–702.

Tullis, T. E., and J. D. Weeks (1986), Constitutive behavior and stability of frictional sliding of granite, *Pure Appl. Geophys., 124*, 384–414.
Tullis, T. E., and J. D. Weeks (1987), Micromechanics of frictional resistance of calcite, *Eos Trans. AGU, 68*, 405.
Tullis, T. E., F. G. Horowitz, and J. A. Tullis (1991), Flow laws of polyphase aggregates from end-member flow laws, *J. Geophys. Res., 96*, 8081–8096.
Tullis, T. E., Cooper, C., Sanford, D., and A. Lochhead (1994), The influence of fluid chemistry on nanoindentation of quartz: relevance for the friction evolution effect, *Eos Trans. AGU, 75, Fall Meeting Abs. Supp.*, 443.
Viswanathan, S., and D. Kohlstedt (1996), Evolution of friction coefficient during sliding of a single asperity on semi-brittle mineral surfaces, *Eos Trans. AGU, 77*(46), Fall Meet. Suppl., F696.
Viswanathan, S., D. Kohlstedt, G. Eckhardt, and B. Evans (1995), Partitioning of strain between brittle and ductile deformation in microscratches on calcite, *Eos Trans. AGU, 76*(46), Fall Meet. Suppl., F583.
Walsh, J. B. (1971), Stiffness in faulting and friction experiments, *J. Geophys. Res., 76*, 8597–8598.
Walsh, J. B., and M. A. Grosenbaugh (1979), A new model for analyzing the effect of fractures on compressibility, *J. Geophys. Res., 84*, 3532–3536.
Wang, K., and J. He (1999), Mechanics of low-stress forearcs: Nankai and Cascadia, *J. Geophys. Res., 104*, 15,191–15,205.
Wang, W., and C. H. Scholz (1994), Micromechanics of the velocity and normal stress dependence of rock friction, *Pure Appl. Geophys., 143*, 303–316.
Weeks, J. D., and T. E. Tullis (1985), Frictional sliding of dolomite: A variation in constitutive behavior, *J. Geophys. Res., 90*, 7821–7826.
Weeks, J. D., and T. E. Tullis (1992), High-resolution measurement of displacement in rock friction experiments, *Eos Trans. AGU, 73*, 565.
Weeks, J. D., N. M. Beeler, and T. E. Tullis (1991), Glass is like a rock, *Eos Trans. AGU, 72*, 457–458.
Westbrook, G. K., and M. J. Smith (1983), Long decollements and mud volcanoes: Evidence from the Barbados Ridge Complex for the role of high pore-fluid pressure in the development of an accretionary complex, *Geology, 11*(5), 279–283.
Westbrook, J. H. (1958), Temperature dependence of strength and brittleness of some quartz structures, *J. Am Ceram. Soc., 41*, 433–440.
Westbrook, J. H., and P. J. Jorgensen (1965), Indentation creep of solids, *Trans. Am. Inst. Min. Metall. Pet. Eng., 233*, 425–428.
Westbrook, J. H., and P. J. Jorgensen (1968), Effects of water desorption on indentation microhardness anisotropy in minerals, *Am. Mineral., 53*, 1899–1909.
Wiederhorn, S. M., and L. H. Bolz (1970), Stress corrosion and static fatigue of glass, *J. Am. Ceram. Soc., 53*, 543–548.
Wong, T.-F. (1982), Shear fracture energy of Westerly granite from post-failure behavior, *J. Geophys. Res., 87*, 990–1000.
Wong, T.-F. (1986), On the normal stress dependence of the shear fracture energy, in *Earthquake Source Mechanics, Geophys. Monogr. Ser.,* vol. 37, edited by S. Das et al., pp. 1–11, AGU, Washington, D. C.
Wong, T.-F. (1990), Mechanical compaction and the brittle-ductile transition in porous sandstones, in *Deformation Mechanisms, Rheology and Tectonics*, *Spec. Publ. Geol. Soc., 54*, 111–122.
Wong, T.-F., and Y. Zhao (1990), Effects of load point velocity on frictional instability behavior, *Tectonophysics, 175*, 177–195.
Yamashita, Y., and L. Knopoff (1987), Models of aftershock occurrence, *Geophys. J. R. Astron. Soc., 91*, 13–26.
Yund, R. A., M. L. Blanpied, T. E. Tullis, and J. D. Weeks (1990), Amorphous material in high strain experimental fault gouges, *J. Geophys. Res., 95*, 15,589–15,602.